Non-axisymmetric equilibrium reconstruction and suppression of density limit disruptions in a current-carrying stellarator

by

Xinxing Ma

A dissertation submitted to the Graduate Faculty of
Auburn University
in partial fulfillment of the
requirements for the Degree of
Doctor of Philosophy

Auburn, Alabama
May 5, 2018

Keywords: Stellarator, CTH, Equilibrium Reconstruction, Density Limit

Approved by

David A. Maurer, Chair, Professor of Physics
Stephen F. Knowlton, Co-Chair, Professor Emeritus of Physics
David A. Ennis, Assistant Professor of Physics
Gregory J. Hartwell, Associate Research Professor of Physics
Ryan Comes, Assistant Professor of Physics
Lloyd Riggs, Professor of Electrical and Computer Engineering

Abstract

Reconstruction of non-axisymmetric, three-dimensional (3D) plasma equilibria is important for understanding 3D confinement and stability in stellarators as well as in nominally axisymmetric plasmas in tokamaks and reversed-field pinches (RFP). Tests of non-axisymmetric free-boundary equilibrium reconstruction are performed on the Compact Toroidal Hybrid (CTH) experiment, a small torsatron/tokamak hybrid device. The flexible CTH magnetic configuration allows varying the amount of 3-D shaping by modifying the rotational transform of the magnetic field. 3D equilibrium reconstruction on this device is used to determine the effect of the internal current on the 3D shaping of the MHD equilibrium. The results are used to interpret the stability, and disruptive characteristics of hybrid stellarator/tokamak plasmas.

These studies were performed using the 3D equilibrium reconstruction code V3FIT with experimental measurements from external magnetics and soft X-ray (SXR) cameras. It was verified that external magnetic diagnostics have limited sensitivity to accurately reconstruct the internal experimental current distribution. Instead the current distribution was reconstructed by two methods using soft X-ray measurements. The location of the sawtooth inversion radius can be identified by soft X-ray analysis to infer the radial location of the $q = 1$ surface, which is used to fit parameters of plasma current profile with greater precision than with magnetic signals alone. Secondly, SXR emissivity multi-channel measurements are used to reconstruct the shape and position of flux surfaces, and infer the current distribution within the plasma. The reconstruction results are consistent with those using external magnetic data and the constraint of the location of $q = 1$ surfaces determined from inversion surface radii extracted from SXR emission data.

Improved reconstructions of current and q profiles provide insight into understanding the physics of density limit disruptions observed in current-carrying discharges in CTH. The phenomenology of hybrid discharge terminations is similar to tokamak disruptions. As a result of the ability to adjust the external vacuum rotational transform in CTH, we have found the density limit at a given current increases linearly with the addition of vacuum transform. Consequently, plasmas with densities up to two times the Greenwald limit[1] are attained at the maximum vacuum transform of 0.22. Equilibrium reconstructions show that addition of 3D fields effectively moves resonance surfaces towards the edge of the plasma where the current profile gradient is lower, providing a stabilizing effect to the growth of resistive rearing modes.

Acknowledgments

First of all, I would like to express my deepest gratitude to the chair and co-chair of my committee members, Prof. David Maurer and Prof. Stephen Knowlton. Thank them for continues patience and support, guiding me through over seven years of study and research in CTH. They have been very helpful not just in project discussions, publication and thesis writings, but also in preparations for conference presentations and job interviews. My research will not be as smooth and fruitful without help from each fellow fusion researcher and graduate student. I would like to thank Prof. Greg Hartwell for teaching me almost everything about CTH. I thank Prof. David Ennis for discussions on my research and all suggestions on my publications and thesis. Special thanks to Prof. James Hanson for his support on my work with V3FIT. Supports from all CTHers, Mihir Pandya, Peter Traverso, Jeffery Herfindal, Matt ArchMiller, have been amazing. Thank you guys for running the machine, discussing physics problems.

Thank you Mum and Dad for conditionless love and support. Shiqi, my forever love, I would have not gone so far without you. Thank you for being patient, understanding and the great effort you have made to take care our precious Erica.

Table of Contents

List of Figures

List of Tables

Chapter 1

Introduction

As worldwide consumption of energy and resources steadily increases, it is becoming more probable that traditional, non-renewable energy resources such as coal, oil and natural gas will be significantly depleted in the coming century. What is more, these relatively cheap energy solutions come at a coast of environmental damage via the generation of harmful pollutants, including greenhouse gases. The last decades have correspondingly seen a serious pursuit of renewable, cleaner sources of energy. Renewable energy technologies such as wind, solar photovoltaic and hydroelectric, are considered to be relatively clean sources of energy in that they produce no harmful by-products. However they have their own weakness. Solar and wind power are intermittent sources without fully predictable output and are restricted by climate and other environmental effects. Thus they are considered by many to be still relatively immature and expensive compared to fossil fuels. While hydropower is a mature technology with relatively low costs, in some industrial countries, the available sites for hydropower have been nearly fully exploited, and thus do not offer much possibility of significant expansion. Besides, dams may have huge influence on local environments and some effects can show up after years.

For either non-renewable fossil fuels or renewable solar, wind and hydropower, their origin is the fusion reaction in the sun, in which two light nuclei such as hydrogen or its isotopes, collide with each other, producing a heavier nuclei accompanied by the release of energy. The thermonuclear fusion reaction has revealed its power with the mighty H-bomb in a uncontrolled, destructive way. Accomplishing the fusion reaction in a controlled environment and collecting released energy during the process will be a more positive outcome, producing abundant and clean energy. While there are many possible fusion reactions, the particular process of interest for controlled fusion is the deuterium-tritium reaction:

$$D + T \rightarrow He^4(3.5\,\mathrm{MeV}) + n(14.1\,\mathrm{MeV})\,, \tag{1.1}$$

where high energy neutrons are produced. This process has the highest fusion cross-section at low incident energies[2].

However, great benefits come with enormous challenges. For a sufficient fraction of charged nuclei to overcome their mutual Coulomb repulsion to allow them to fuse the collection of charged particles, plasma, must have a sizable average kinetic energy, in the range of $10-20\,\mathrm{keV}$. This requires the temperature of the burning plasma to reach $100-200$ million $^\circ C$[3]. Because no matter In this extreme condition, any material on the Earth can easily be destroyed by the hot plasma. Thus advanced confinement techniques are required. Another challenge comes from how to capture the released thermal energy, transfer it into electrical energy, and make sure the overall outcome is greater than the input power, i.e. to exceed the break-even condition

Current research focused on two promising solutions for electric energy productions: Inertial Confinement Fusion (ICF) and magnetic confinement fusion. Inertial confinement, which is outside the scope of this thesis, attempts to obtain fusion by heating and compressing a fuel target, typically in the form of pellet that would contain a mixture of deuterium and tritium, using converging high-energy beams of laser light, electrons or ions. In the magnetic confinement approach, strong magnetic fields are used to confine the hot dense plasma for a sufficiently long period of time while the plasma is heated such that random collisions between deuterium and tritium nuclei will produce fusion. Major magnetic confinement concepts that have been explored include axisymmetric (toroidal symmetry) configurations, such as tokamak, reversed field pinch, spheromak and field reversed configuration, and inherently non-axisymmetric configuration, stellarator.

One of the major challenges of magnetic confinement is not only to sustain continuous high temperature plasma but also to ensure the hydrodynamic stability of the confined plasma for reactions. The operation of these fusion devices is usually limited by instabilities and disruptive phenomenon associated with plasma current, pressure gradient and density. Among them, the density limit describes the maximum density that can be achieved in a magnetic confined plasma[4]. In various magnetic confinement experiments, it is found that there are clear limitations on the density that can be achieved even with advanced heating or fueling techniques. Attempts to raise the density beyond the limit result in a disruption of the discharge. Since the fusion reaction rate scales with n^2, the density limit plays an important role in achieving practical fusion power. Therefore studies of the physics and mechanism behind density limit along with its mitigation and avoidance are of great importance to the success of future fusion plant.

1.1 Magnetically confined plasma

A charged particle within a magnetic Field $\boldsymbol{B}$ is subject to the Lorentz force:

$$\boldsymbol{F} = q\boldsymbol{v} \times \boldsymbol{B}\,, \tag{1.2}$$

where q is the charge of the particle and $\boldsymbol{v}$ is the velocity of the particle. For a particle moving perpendicularly to a magnetic field line, the Lorentz force produces a force pulling the particle towards the magnetic filed line. Thus the particle orbits around the magnetic field line with a characteristic frequency called the gyro frequency,

$$\omega = \frac{|q|B}{m}\,, \tag{1.3}$$

at a characteristic radius known as the Larmor radius,

$$r_L = \frac{mv_\perp}{|q|B}\,. \tag{1.4}$$

Here m is the mass of the charged particle, and $v_\perp$ refers to the velocity component that is perpendicular to the magnetic field, $\boldsymbol{B}$. In conjunction with the parallel component of the motion, the trajectory of a charged particle in the plasma follows the helical orbit of the field

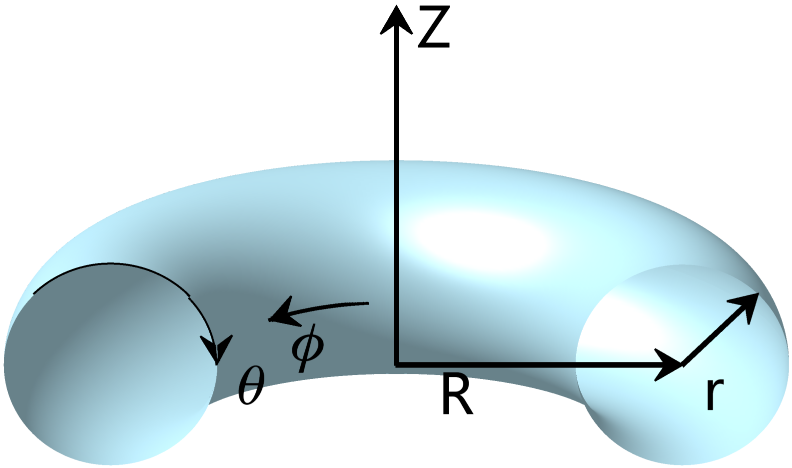

Figure 1.1: Toroidal geometry is used in plasma confinement. R is the major radius of the torus, r is the minor radius, θ is the poloidal angle and ϕ is the toroidal angle. Z-axis is vertical, and normal to the horizontal plane of the torus.

line. In the absence of collisions, this orbital motion traps the particle on the magnetic field lines.

Ideally, a field line confines a charged particle if it can go from $x = +\infty$ to $-\infty$. To produce an enclosed finite volume of plasma, the magnetic field lines are curved back onto themselves. A magnetic confinement device is designed to produce magnetic fields to minimize contact of the hot plasma with the enclosing vessel wall. One natural geometry of magnetic confinement devices is a torus as shown in Fig. 1.1. Here the increments in toroidal or azimuthal angle, ϕ, and poloidal angle, θ, are indicated by arrows. R and r are the major radius and minor radius of the torus respectively. The Z-direction is along the axis normal to the plane of the torus. If there was only a toroidal field in the ϕ-direction within the torus, the plasma would be convected outward by an $\boldsymbol{E} \times \boldsymbol{B}$ drift, leading to the loss of confinement. This $\boldsymbol{E}$ field arises from the gradient of a $\boldsymbol{B}$ field and centrifugal drifts. To counteract this drift, a poloidal magnetic field is added to create a helical magnetic field.

In a tokamak, the toroidal magnetic field is provided by the external currents flowing in planar electromagnetic coils spaced along the ϕ-direction, while the poloidal magnetic field is mainly provided by a toroidal current within the plasma. Typically this current is driven by a voltage induced by an external circuit called the ohmic heating transformer. Thus the magnetic configuration in a tokamak exhibits toroidal symmetry. In contrast, in current-free stellarators, both toroidal and poloidal magnetic fields necessary for toroidal plasma confinement are supplied by currents in external magnetic coils, resulting a non-axisymmetric magnetic configuration. A comparison of the last closed flux surfaces of an axisymmetric tokamak and a non-axisymmetric stellarator is shown in Fig. 1.2[1].

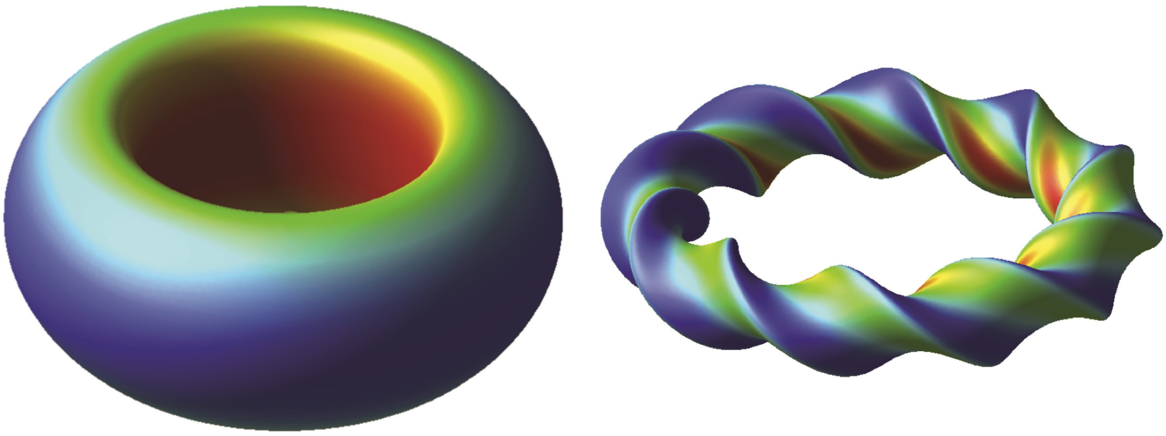

Figure 1.2: The last closed flux surfaces of (a) an axisymmetric tokamak with continuous rotational symmetry in the toroidal direction, and (b) a ten field period stellarator with discrete symmetry. Colors indicates the strength of magnetic fields.[1]

The helicity of the curved magnetic field line is characterized by the rotational transform. Considering the trajectory of a field line, the rotational transform can be defined as the average change in poloidal angle of the field line location, $\langle \Delta\theta \rangle$, normalized to the toroidal circuit of 2π. The average nominally is applied over an infinite number of toroidal transits[5]:

$$\iota = \lim_{N\to\infty} \frac{1}{N} \sum_{1}^{N} \frac{\Delta\theta}{2\pi} \tag{1.5}$$

Here 2π is the change in toroidal angle, $\Delta\phi = 2\pi$ for a single toroidal transit of the field line. If a field line makes n poloidal transits during m toroidal transits, the rotational transform of this specific field line is given by:

$$\iota = \frac{n}{m}\,. \tag{1.6}$$

The helical fields of the different rotational transforms form a set of nested flux surfaces. If n and m in Eq. 1.6 are integers, these magnetic field lines would close on themselves after a finite number of toroidal and poloidal circuits of the field line. The flux surface formed by this group of magnetic field lines is known as rational flux surface. Otherwise, magnetic field lines never close upon themselves after infinite number of toroidal transits and form so-called ergodic flux surfaces. In a tokamak, the parameter q is used to characterize the helicity of field lines. This parameter is the safety factor, and is the reciprocal of the rotational transform: $q = \frac{1}{\iota}$.

A fluid model, the magnetohydrodynamic (MHD) model, is used to describe the dynamics and macroscopic equilibrium and stability of the plasma within these magnetic fields. In the ideal MHD approach, the plasma is represented by a single fluid with infinite conductivity and zero ion gyro radius. Details of the ideal MHD theory is given by Freidberg[5]. In a static ideal MHD equilibrium, the confined plasma obeys the force balance equation:

$$\nabla p = \boldsymbol{J} \times \boldsymbol{B}\,, \tag{1.7}$$

where $\boldsymbol{J}$ is the plasma current density and p is the plasma pressure. Taking the dot product of Eq. 1.7 with field $\boldsymbol{B}$ gives:

$$\boldsymbol{B} \cdot \nabla p = 0\,. \tag{1.8}$$

Therefore the magnetic field must be tangential to the contours of constant pressure, thus magnetic flux surfaces are also surfaces of constant pressures. The plasma pressure is typically maximum at the magnetic axis, where magnetic flux surface approaches single field line in the center of the poloidal cross-section, and decreases at outward surfaces.

An example of nested flux surfaces for a plasma equilibrium in the Compact Toroidal Hybrid (CTH) is shown in Fig. 1.3. In contrast with traditional current-free stellarators, CTH is a tokamak/stellarator hybrid with the ability to drive plasma current within pre-established pure stellarator plasma. CTH can vary the amount of rotational transform from a near axisymmetric tokamak-like equilibrium to a fully 3D non-axisymmetric stellarator equilibrium.

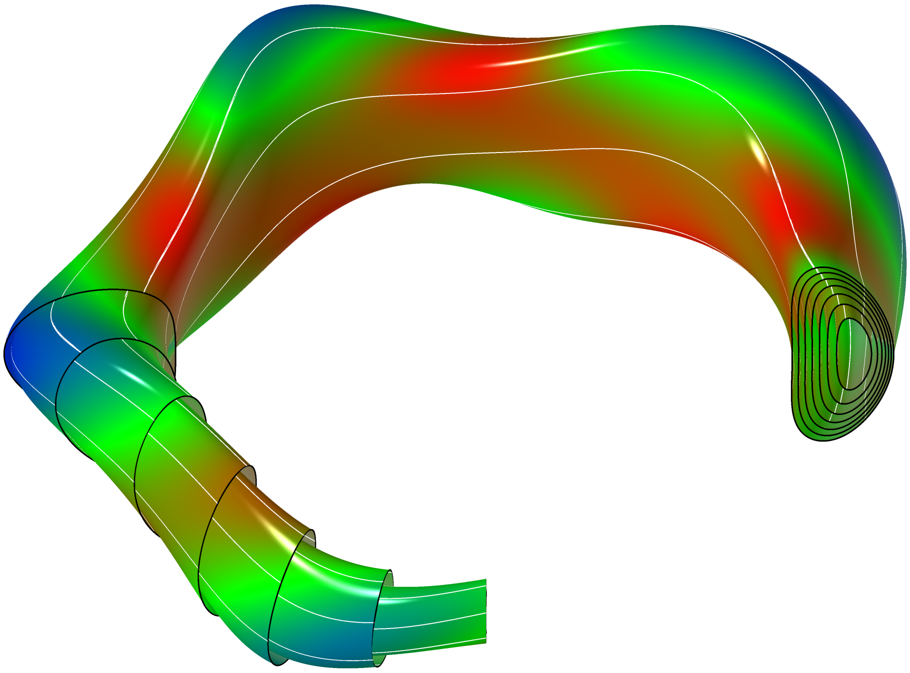

Figure 1.3: Layers of closed nested magnetic flux surfaces in CTH. The coloring represents the strength of the magnetic field. A few magnetic field lines are plotted in white on flux surfaces. [Figure provided by M. Cianciosa]

1.2 Goal of this thesis

Fusion science is now moving into the era of controlled burning plasma experiments. As the largest thermonuclear fusion project, International Thermonuclear Experimental Reactor (ITER) is under construction in France and will attempt to achieve a fusion power gain of up to 10 for over five minutes[6]. As a result, ITER confronts the practical challenges of tokamak physics and technology at a scale greater than in any previous experiment. Some of the critical challenges that hinder the tokamak concept are plasma disruptions, operational complexity, and control of the self-organized burning plasma state. Designed as a tokamak/stellarator hybrid, CTH has the flexibility to vary externally applied rotational transform, i.e. the amount of three-dimensional (3D) magnetic field imposed. It targets the challenge of reducing the disruptivity of toroidal plasmas by passive, 3D shaping of the equilibrium magnetic flux surfaces. Equally important is to develop a predictive physics basis for disruption modification using 3D shaping fields. Indeed, experiments on current-carrying stellarators have shown evidences of disruption avoidance and improved positional stability[7–9].

In principle, the stellarator configuration can avoid the problem of major disruptions by operating in MHD stable regimes. It can also operate with long pulses without significant auxiliary current drive. Thus stellarator configuration is inherently a steady-state concept capable of ignition operation, and the stellarator approach is considered to be a realistic means of overcome a number of practical challenges to fusion. What is more, the stellarator provides an example of the benefit that strong 3D shaping field can lead to improved toroidal magnetic confinement. High performance stellarator such as LHD is exploring confinement regimes in current-free helical discharges[10], in which the average non-axisymmetric magnetic filed component B_{3D} is comparable to the main axisymmetric toroidal filed B_0, $B_{3D}/B_0 \sim 0.3$. LHD has achieved an averaged beta value of 5%[11], comparable to that required for stellarator power plant. There is also evidence that quasi-symmetric field configurations in stellarators improves the confinement and plasma flow while exploiting the steady-state advantages of the stellarator[12,13]. On the other hand, modest levels of 3D field structure ($B_{3D}/B_0 \sim 10^{-4} - 10^{-3}$) have been applied to tokamaks to effect control of resistive wall modes (RWM)[14,15] and edge localized modes (ELM)[16,17]. Relative theoretical work suggests that some form of 3D magnetic field structure is expected in the design of future steady state reactors[1,18,19].

A natural question arises, what are the potential benefits of a larger level of non-axisymmetric shaping field in nominally axisymmetric tokamaks, or how can the 3D vacuum equilibrium of helical configurations broadly improve control and maintenance of tokamak discharges. This could lead to the control and avoidance of disruptions as well as the sustainment of the discharges by means of supplemental rotational transform supplied by external helical or modular coils with $B_{3D}/B_0 \sim 10^{-2} - 10^{-1}$. To answer this equation, a hybrid magnetic configuration such as CTH is proposed , where a toroidal plasma current can be driven on the flux surface of a pure stellarator equilibrium. The goal of this approach is specifically to reduce plasma disruptions and their consequences by superimposing closed stellarator flux surfaces on current-driven toroidal discharges.

The major objectives of this work on CTH focus on understanding the effects of strong 3D shaping on the equilibrium and stability of hybrid discharges[20]. Specifically they are:

- Exploring the magnitude and geometry of non-axisymmetric 3D shaping field that is effective in instability, disruption mitigation and avoidance in current-carrying discharges.
- Understanding the physics of major disruptions in hybrid discharges as well as the mechanism of their mitigation and avoidance with imposed external vacuum rotational transform.
- Validating and improving equilibrium modeling and reconstruction to providing linkage of experimental observations to computational prediction for large devices.
- Understanding the impact of resonant field errors or magnetic islands in hybrid discharges.

1.3 Thesis overview

This thesis provides equilibrium reconstructions of hybrid discharges in CTH with 3D equilibrium reconstruction code V3FIT[21], and using it as a tool to understand the effect of strong 3D shaping on MHD instability and disruption, specially the density limit disruption. Equilibrium reconstruction is a process in which the diagnostic signals computed from a model plasma equilibrium are compared with corresponding data from experimental measurements to find an accurate model of the actual experimental equilibrium configuration. Reconstruction of non-axisymmetric, three-dimensional plasma equilibrium is important for understanding intrinsic 3D confinement and stability in stellarators. CTH‘s unique hybrid nature makes itself a good test-bed to benchmark and validate the V3FIT code. Continuous and considerable efforts have been put into the improvements and benchmarking of V3FIT, which not only impact the scientific merit of experimental explorations on CTH, but also motivate improvements in the code itself. Accordingly equilibrium reconstructions with both external magnetic measurements and internal soft x-ray emissivity measurements have routinely been performed for various CTH discharges. This capability enables a more quantitatively evaluation of the conditions for MHD instability that lead to disruptions. With addition of internal soft-x ray emissivity measurements, V3FIT gives better reconstruction of the core of the plasma compared to the one using external magnetic diagnostics alone. We have found that density limit disruptions in a current-carrying stellarator exhibit similar phenomena as in tokamaks. And the final scenario of the density limit is consistent with classic observation in tokamaks, involving cooling of edge plasma, current profile shrinkage, growing MHD instabilities (usually $m/n = 1/2$ tearing mode) followed by loss of MHD equilibrium, and final disruptions[22]. What makes CTH standout is that the disruptive behavior of current-carrying discharges in CTH can be reproducibly modified by the presence of modest levels of externally generated rotational transform. CTH plasma can routinely operate beyond the empirical Greenwald density limit[23] with addition of 3D magnetic shaping field. As the vacuum rotational transform is raised, normalized density before disruption increases by a factor of nearly 4, although we have not found a threshold value of vacuum transform that eliminates disruptions. Equilibrium reconstructions of the these discharges suggest that modified disruption behavior is due to changed interaction between current profile and safety factor q profile with imposed 3D shaping fields.

The outline of this thesis is as follows: Chapter 2 describes the CTH experiment, especially its flexible magnetic configuration, along with the diagnostics available in equilibrium reconstruction on CTH. Chapter 3 gives a brief introduction of the computational tools for 3D equilibrium reconstruction performed on CTH, the VMEC and V3FIT codes. Chapter 4 discusses the design, installation and optimization of various magnetic diagnostics on CTH, and how they are incorporated in V3FIT to reconstruct CTH plasmas. Chapter 5 highlights both the indirect and direct application of soft-x ray (SXR) measurements in V3FIT to improve the reconstruction of current profile on CTH. Chapter 6 contains a complete discussion of the scaling laws, experimental observations, involved physics and proposed mechanism of density limit disruptions on toroidal confinement experiments, similarity and uniqueness of density limit disruptions on CTH, and demonstrates the suppression of density limit disruptions with increasing amounts of stellarator transform provided by the external coil currents. Chapter 7 summarizes and discusses the major results along with possible future work to extend current understanding.

Chapter 2

Experimental platform for study of 3D equilibrium reconstructions

2.1 Introduction

The experimental toroidal magnetic equilibria studied in this work were obtained on the CTH hybrid stellarator. A photo of the CTH device is shown in Fig. 2.1. Compared to most stellarators, it produces a low aspect ratio plasma with $R/a_{\text{plasma}} > 3.5$. Here, R is the major plasma radius and a_{plasma} is the toroidally averaged minor radius. Like all stellarators, the magnetic configuration of CTH lacks toroidal symmetry (or axisymmetry), but exhibits field-period symmetry in the toroidal direction, in which the magnetic configuration is repeated on integral number of times in the full toroidal circuit. The magnetic coil system is designed to create field-periodic magnetic flux surfaces, in which the set of points defining the magnetic flux surfaces have the following property[24]:

$$[R(\Phi,\theta,\phi), Z(\Phi,\theta,\phi)] \iff \left[R\left(\Phi,\theta,\frac{2\pi n}{N}+\phi\right), Z\left(\Phi,\theta,\frac{2\pi n}{N}+\phi\right)\right] \tag{2.1}$$

Here the functions R and Z refer to the set of points on a given flux surface labeled by Φ. The radial-like coordinate Φ is typically the toroidal magnetic flux enclosed in a specific flux surface; $\Phi = \iint \boldsymbol{B} \cdot \hat{\phi} dA$. θ and ϕ are the poloidal and toroidal angles respectively. The number of field periods of CTH is $N = 5$. The coil configuration is also designed to enforce stellarator symmetry, so that the magnetic flux surfaces also exhibit the following property of vertical symmetry:

$$[R(\Phi,\theta,\phi), Z(\Phi,\theta,\phi)] \iff [R(\Phi,\theta,-\phi), -Z(\Phi,\theta,\phi)] \tag{2.2}$$

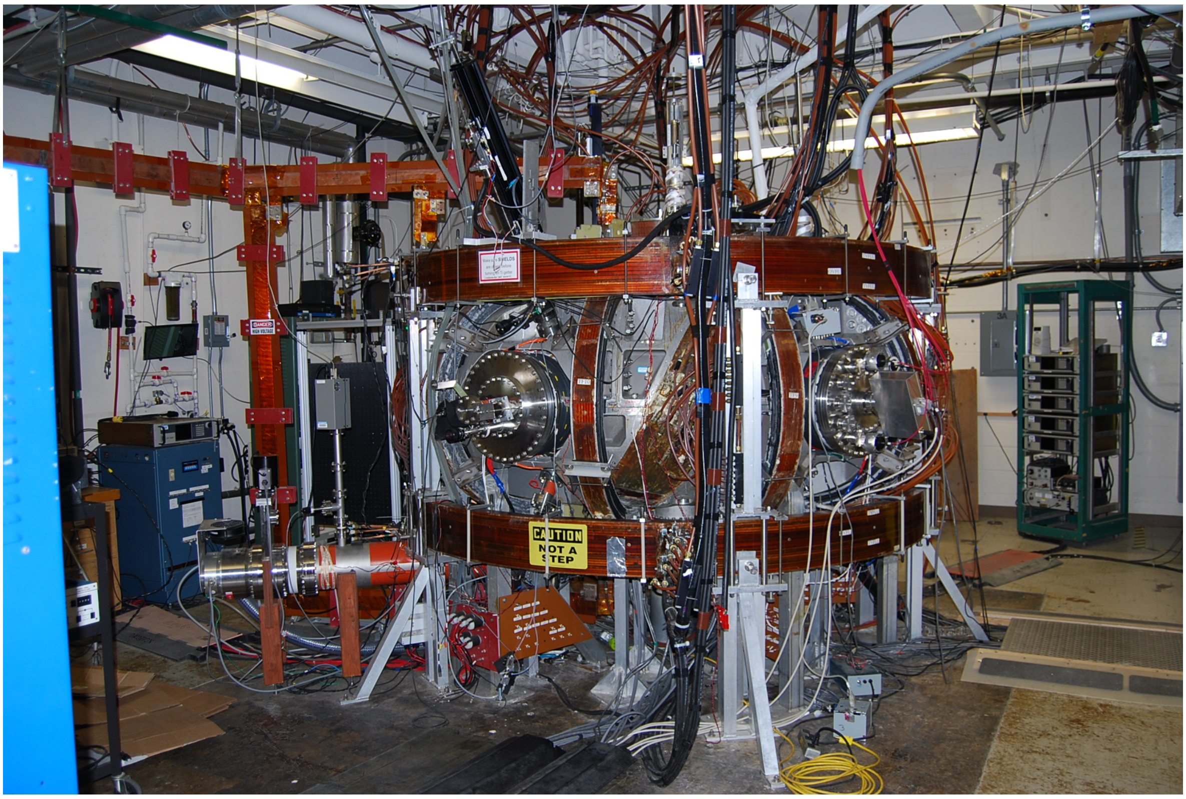

Figure 2.1: CTH machine area

The maximum toroidal magnetic field produced by the CTH coil set is $B_0 = 0.6\,\mathrm{T}$.

CTH may operate as a pure stellarator, or as an unusual hybrid of a current-carrying tokamak and a stellarator. When CTH operates as a pure stellarator, the magnetic rotational transform, which is required to generate closed, nested flux surfaces for confinement, is provided by external magnetic field coils alone. In its unique hybrid role, a central ohmic solenoid can drive a toroidal current, I_p, within a pre-established ECRH (electron cyclotron resonance heating) stellarator plasma. By varying the currents in the external magnetic coils and the total plasma current, CTH is capable of investigating the effects of strong 3D shaping on MHD instabilities and disruptions that are driven by unstable plasma currents. Table. 2.1 shows several major parameters of the CTH design and plasmas.

A discussion of CTH magnetic coil configuration is presented in sec. 2.2. Numerous diagnostics available on CTH are described in sec. 2.3.

R	$0.75\,\mathrm{m}$	P_{ECRH}	$\leqslant 30\,\mathrm{kW}$
a_{vessel}	$0.289\,\mathrm{m}$	n_{e}	$\leqslant 4 \times 10^{19} m^{-3}$
a_{plasma}	$\leqslant 0.2\mathrm{m}$	$T_{\mathrm{e}}(\mathrm{est.})$	$\leqslant 200\,\mathrm{eV}$
B_0	$\leqslant 0.6\,\mathrm{T}$	β	$\leqslant 0.5\%$
I_{p}	$\leqslant 80\,\mathrm{kA}$	Edge ι_{vac}	$0.02 - 0.32$

Table 2.1: Major parameters of CTH design and operation

2.2 CTH magnetic configuration

The main magnet coils of CTH are shown in Fig. 2.2. They consist of six, independently-controlled, magnetic coil sets, which allow the vacuum magnetic rotational transform, magnetic shear, and vertical elongation to be varied. Also shown is the vacuum vessel in gray.

Although the plasmas in CTH are non-axisymmetric, the vacuum vessel was chosen to be circular in both poloidal and toroidal cross section It has a major radius of $R_0 = 0.75\,\mathrm{m}$ and a minor radius of $a_{\mathrm{vessel}} = 0.29\,\mathrm{m}$. Unlike strongly-shaped vessels of stellarator configurations defined by a set of highly-optimized coils[25–27], the CTH vessel allows a large variety of plasma shapes and positions to be accommodated. The choice of a circular vessel was also based on economy. The wall of the Inconel 625 alloy vessel has an average thickness of $2.5\,\mathrm{mm}$ and toroidal electric resistance of approximately $1\,\mathrm{m}\Omega$. As a result, the inductive toroidal loop voltage of current-driven plasmas will also induce current within the vacuum vessel itself. The placement of all ports are designed to maintain the five-field periodicity and reduce the magnitude of symmetry-breaking errors from finite vacuum vessel currents. These finite vacuum vessel currents are eddy currents induced by changing magnetic fluxes form the coil and plasma currents. Additional eddy currents are driven in other conducting structures including the helical coil frame, which consists of ten identical interlocking but electrically-isolated cast aluminum frame pieces. More details about the description of eddy currents on CTH and proper modeling in equilibrium reconstruction will be discussed in Sec. 4.3.2.

A single $\ell = 2$, $m = 5$ helical field coil (HF), consisting of 96 turns, is wound onto an aluminum frame that encloses the vacuum vessel. The coil makes two toroidal circuits for every five poloidal circuits as it is wound around the vacuum vessel. The helical path followed by the center of the HF coil pack is defined by a HF coil winding law[28,29] in pseudo-toroidal

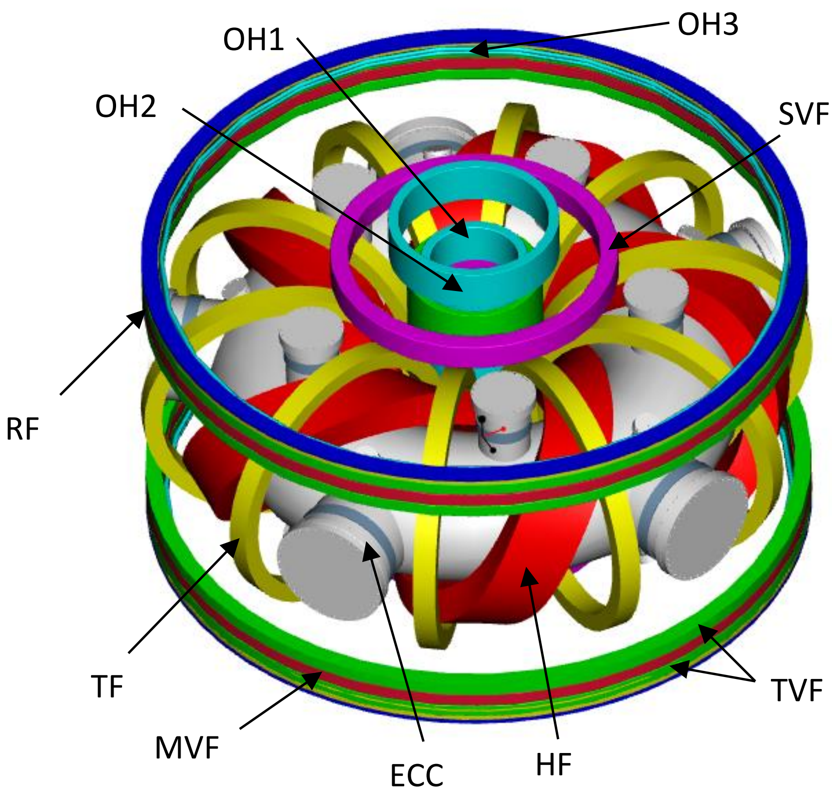

Figure 2.2: Magnet coils of the Compact Toroidal Hybrid: Helical field coil (HF) and main vertical field coils (OMVF), connected in series, are shown in red. Additional poloidal field coils for trimming the vertical field (TVF) and radial field (RF) are shown in green and blue respectively. Auxiliary toroidal field (TF) coils are shown in yellow. The shaping vertical field coil (SVF) set for elongation and shear is shown in purple. The ohmic transformer solenoid and dedicated poloidal for ohmic flux expansion (OH) are indicated in green-blue.

coordinates (r, θ, ϕ). The winding law was selected by optimization with the IFT code[30] to maximize the volume of the region within the CTH vacuum vessel. Since the current in the HF coil is unidirectional, the magnetic configuration of CTH is referred to as a torsatron within the class of stellarators.

The HF coil provides toroidal and poloidal components of the equilibrium helical field. In most torsatrons and CTH in particular, an additional poloidal/vertical field is required to produce a closed vacuum equilibrium within the volume of the vacuum vessel. The poloidal field coil set on CTH consists of four subsets:

1. The main vertical field (MVF) coils, electrically connected in series with the HF coil (and therefore with the same current as the HF coil), to provide approximately 50% fo the vertical field required for equilibrium.

2. A pair of trim vertical field (TVF) coils, powered independently to further control the radial position of the plasma

3. A shaping vertical field (SVF) coil set, providing a quadrupole field, to adjust the vertical elongation as well as the magnetic shear of the plasma equilibrium.

4. A radial field (RF) coil set for shifting the vertical position of the plasma, or maintain vertical stability during ohmic operation.

The vacuum rotational transform, ι_{vac}, can be raised or lowered with the use of ten auxiliary toroidal field (TF) coils by adding to or subtracting from the toroidal field component produced by HF coil. Various vacuum transform radial profiles for different ratios, $I_{\mathbf{TF}}/I_{\mathbf{HF}}$, are plotted in Fig. 2.3. With the independent control presently available, the edge vacuum rotational transform, $\iota_{\text{vac}}(a)$, can be varied from 0.02 to 0.35.

To operate as a hybrid tokamak/stellarator, a toroidal current is driven using the ohmic heating transformer within the pre-established ECRH plasma. In a typical experiment in CTH, a vacuum configuration presumably with predictable nested closed magnetic flux surfaces is first obtained using external coil currents. A plasma is then produced in this magnetic configuration using ECRH. The plasma working gas is typically hydrogen or deuterium. Next, a large toroidal

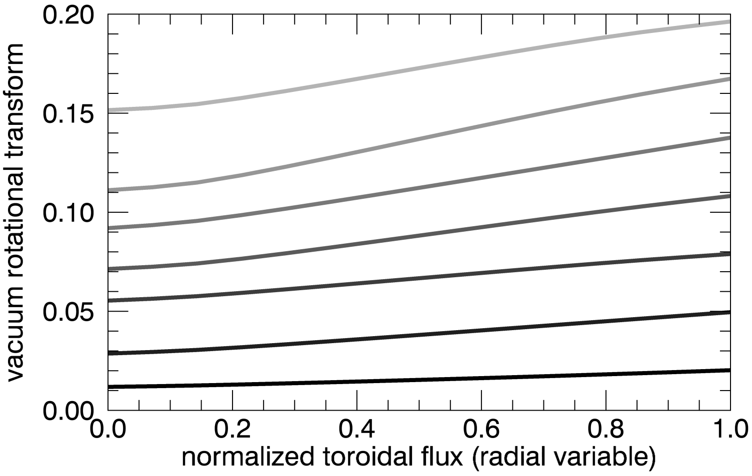

Figure 2.3: Vacuum rotational transform vs. radial-like coordinate Φ for several values of $I_{\mathbf{TF}}/I_{\mathbf{HF}}$. Positive values of $I_{\mathbf{TF}}/I_{\mathbf{HF}}$ correspond to the toroidal components of the TF and HF being parallel, negative to anti-parallel. The normalized toroidal flux is 1 at the last closed flux surface and 0 at the magnetic axis.

loop voltage is induced by the OH coil, leading to a driven toroidal plasma current. The addition of plasma current substantially changes the transform profiles, as shown in Fig. 2.4. In this case, the resulting rotational transform has contributions from both the vacuum field and the poloidal field produced by the driven plasma current. Accordingly, the total rotational transform is the sum of the vacuum rotational transform and the transform due to the plasma current: $\iota_{\mathrm{tot}} = \iota_{\mathrm{vac}} + \iota_{\mathrm{p}}$. In CTH, the driven plasma current can provide up to $\sim 96\%$ of the total rotational transform in some cases.

The magnetic equilibria of CTH plasmas are predicted to be highly non-axisymmetric either with or without ohmic plasma current. The shapes of the last closed flux surfaces are computed with VMEC, and illustrated in Fig. 2.5. One half of a zero-current, ECRH-only plasma is depicted on the left side of the plot, along with poloidal cross-sections of flux surfaces at four different toroidal angles. The right side of the figure shows flux surfaces and plasma shape computed at a plasma current of $I_{\mathrm{p}} = 53.6\,\mathrm{kA}$. While the poloidal cross-section of CTH discharges becomes less elliptical with the addition of driven plasma current, the underlying toroidal $N = 5$ stellarator periodicity is enhanced. Thus even in hybrid discharges, the need for fully 3D computational tools for reconstruction remains clear.

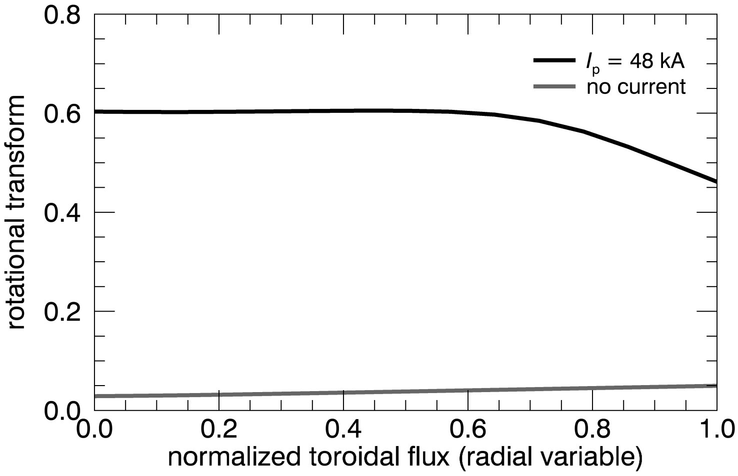

Figure 2.4: Toroidal plasma current substantially modifies the shape of the rotational transform profile. Bottom trace shows the monotonically increasing vacuum transform of ECRH only plasma, with vacuum rotational transform ~ 0.05. The top trace presents the changed total transform with $50\,\mathrm{kA}$ of plasma current and total rotational transform ~ 0.45, showing a monotonically decreasing profile.

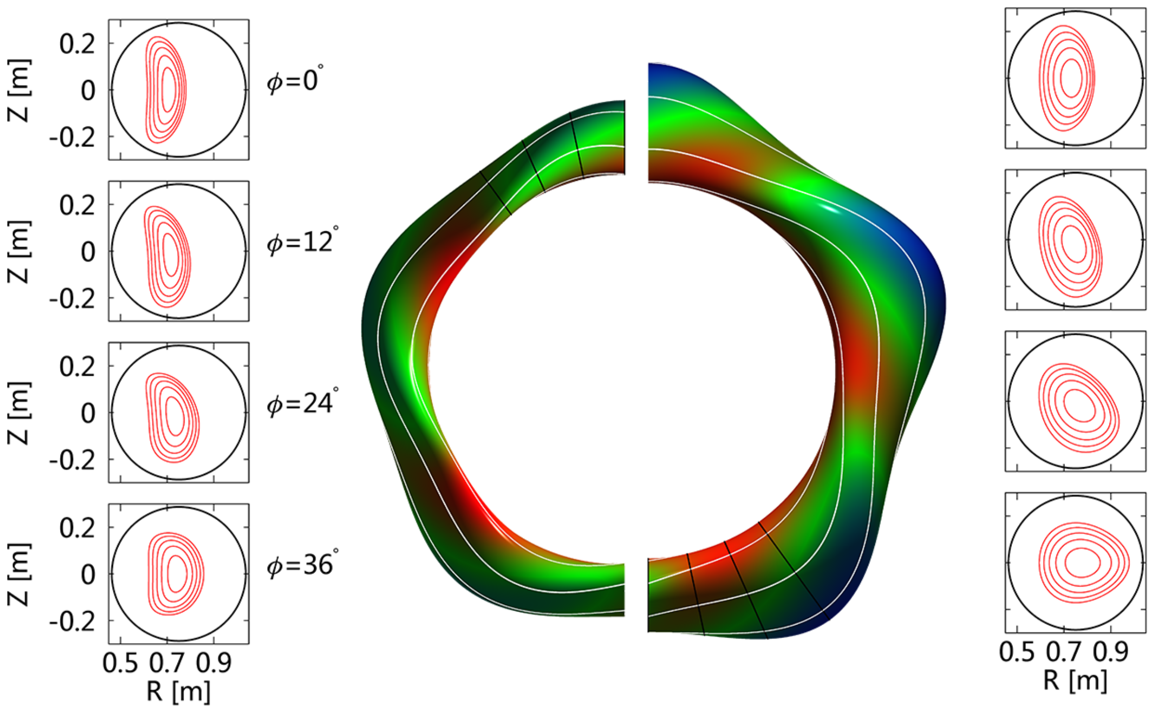

Figure 2.5: Poloidal cross-sections of magnetic flux surfaces and representations of the last closed flux surfaces of CTH plasmas without plasma current ($I_p = 0$)(left) and with $I_p = 53.6kA$. The color shading refers to magnetic field strength (blue lowest; red highest), and several field lines are indicated by white lines.

2.3 CTH diagnostics

Plasma diagnosis is a process that deduces properties of the state of plasma from experimental observations of physical processes and corresponding effects. Its principles are well discussed in numerous references[31–33], which set the foundation to understand experimental diagnostic data and to design and build new diagnostics. In this work, the plasma parameters of plasma shape, position, density, temperature, magnetic fluctuations as well soft-x ray (SXR) emission, are important in performing redible equilibrium reconstructions. A top view of CTH device and positions of various diagnostics available on CTH are shown in Fig. 2.6.

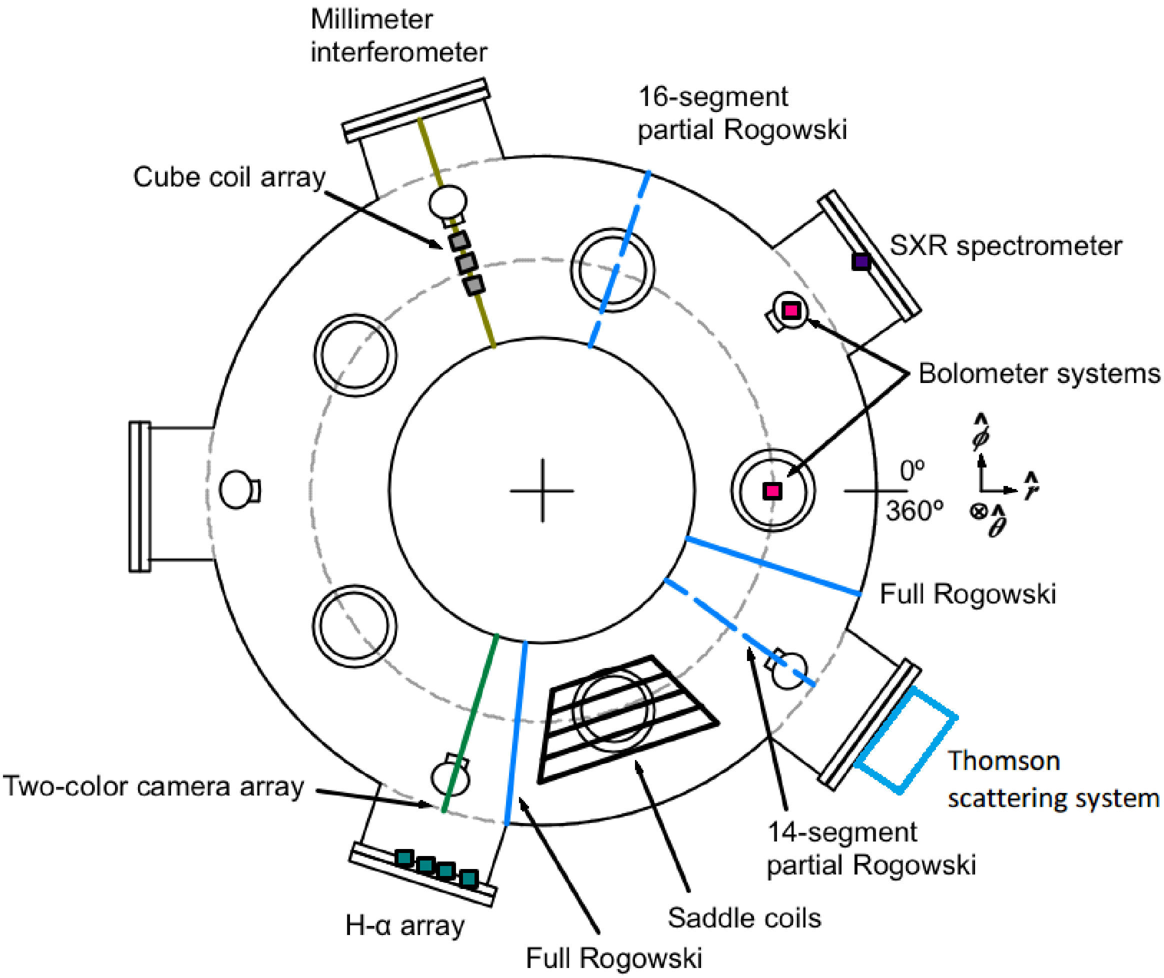

Figure 2.6: Top view of CTH device with a map showing various diagnostics available on CTH.

Magnetic diagnostics on CTH include full and segmented Rogowski coils, saddle shape flux loops, poloidal, toroidal and radial magnetic pick up coils and diamagnetic loops. On CTH, magnetic diagnostics are routinely used to determine plasma current, loop voltage, plasma shape and position[34], current distribution as well as magnetic fluctuations[35]. They are used for equilibrium reconstructions together with other internal diagnostics such as SXR cameras[36].

CTH is also equipped with an extensive collection of emissivity diagnostics consisting of SXR cameras and bolometer cameras. Three 20-channel two-color SXR cameras are developed and installed at the toroidal location of $\phi = 252°$ for electron temperature measurements[37] and soft-x ray fluctuation analysis[38]. Two additional bolometer-SXR systems are located at $\phi = 0°$ and $36°$. The emissivity measurements from all SXR cameras are implemented in the V3FIT code as internal diagnostics primarily for fitting the radial distribution of the plasma current.

The line-integrated electron density is measured with a three-channel $1\,\mathrm{mm}$ microwave interferometer system installed at $\phi = 108°$[39]. One of the three chords passes through the horizontal mid-plane, while the other two located above and below the mid-plane.

Chapter 3

Computational procedures for reconstructions in CTH

3.1 Introduction

Equilibrium reconstruction is an inverse process in which the diagnostic signals computed from a model plasma equilibrium are compared with corresponding data from experimental measurements to find an accurate model of the actual experimental equilibrium configuration. Reconstruction of non-axisymmetric, three-dimensional (3D) plasma equilibria is important for understanding intrinsic 3D confinement and stability in stellarators as well as in nominally axisymmetric plasmas in tokamaks and reversed field pinches (RFP). Reconstruction of two-dimensional (2D) equilibria based upon solving the Grad-Shafranov equation is well understood with reconstruction tools such as EFIT[40] and MSTFIT[41], and is routinely performed for tokamak[42–45] and RFP[41] discharges. The application of fully 3D MHD equilibrium reconstruction of fusion plasmas is less well developed, but is now being applied to a variety of magnetic configurations, including tokamaks and RFPs, as well as stellarators, for which it was originally intended[46]. For example, 3D equilibrium reconstruction has been applied to HSX stellarator discharges to interpret Pfirsch-Schluter and bootstrap currents[47], quasi-single helicity states in RFP plasmas[48], and error field effects on tokamak devices[49]. High β stellarator discharges in the W7-X experiment are likely to benefit from 3D reconstructive capability[50]. Controlling the equilibrium and stability properties of current carrying finite-beta stellarators as embodied in the NCSX design[51] may have required some elements of real-time 3D reconstruction.

The highly 3D shaping of CTH plasmas make it a useful platform to benchmark 3D equilibrium reconstructions. Unlike most present stellarator plasmas, discharges in CTH are modified by ohmically driven plasma current and thus are strongly perturbed from their vacuum configurations. 3D equilibrium reconstruction on this device attempts to determine the effect of internal current on the 3D shaping on the MHD equilibrium, and ultimately the stability and disruptive characteristics of these hybrid stellarator/tokamak-like plasmas. Of particular importance is the knowledge of the plasma current profile which in turn determines the rotational transform profile. With knowledge of the transform profile, the locations of resonant magnetic surfaces at which the rotational transform is a ratio of two integers may be determined. There is no diagnostic in CTH that can directly measures the poloidal magnetic field distribution inside the plasma. A fully 3D equilibrium reconstruction code, V3FIT[21], is used to reconstruct the stellarator equilibrium state with various sets of external and internal diagnostics that are available. The details of V3FIT code required to understand the CTH reconstruction work are presented in this chapter.

3.2 VMEC equilibrium

Models are usually used to simplify and organize knowledge about a system. Typically, a model represents the family of permissible profile solutions of the system using a limited set of parameters. The solution family is thus spanned by a parametric vector space. With given parameters, the model can predict values of experimental observations for the system. This process is called the forward problem. Whether the result is a 2D or 3D calculation, the equilibrium model must be a solution of a plasma-magnetic field MHD equilibrium. Since the non-axisymmetric configuration is considered here, we require a 3D equilibrium solver. In this work, the Variation Moments Equilibrium Code (VMEC)[52,53] is used to provide a 3D equilibrium solution.

Instead of solving the Grad-Shafranov equation as in axisymmetric equilibrium codes, one computes the fully 3D equilibrium with VMEC by solving the MHD force balance equation using variational principle to minimize the total energy.

$$\boldsymbol{J} \times \boldsymbol{B} = \nabla p \tag{3.1}$$

The existence of closed flux surfaces is assumed, and as a result symmetry breaking magnetic islands and chaotic regions are not modeled. The flux surfaces are represented by Fourier modes in poloidal and toroidal coordinates. This greatly reduces the computational complexity and time of the problem, making robust and real-time equilibrium solutions possible. The convergence of the VMEC code to an equilibrium solution requires several input parameters to be set. These are the plasma pressure profile and the current or rotational transform profile. These profiles are parametrized as flux surface variable profiles. The flux surface variable is the normalized toroidal flux, s, with $s = 0$ at the magnetic axis and $s = 1$ at the last closed flux surface. Obviously the experimental profiles in flux coordinates are unknown and their parameterizations must be reconstructed.

VMEC can be operated in fixed or free boundary modes. In the fixed boundary mode, the equilibrium calculation requires knowledge of the last closed flux surface geometry. The shape of the last closed flux surface must be specified. While in free boundary mode the external coil currents and the total toroidal magnetic flux through the last closed flux surface are required. In CTH, the additional plasma current significantly changes the geometry of flux surfaces of the equilibrium such that the geometry of the last closed flux surface is unknown. As a result, VMEC is used in free boundary mode and the boundary of the plasma is limited by limiters.

In the VMEC code, profile models of the current and pressure are implemented as either parametrized functions of normalized magnetic flux or as discrete interpolated segments in flux space such as splines or line segments. The equilibrium reconstructions presented in this thesis make use of two profile parameterizations, both are functions of the normalized toroidal flux. First is the two-power profile modeling, which uses three parameters, α, β and γ in its functional form,

$$f(s) = \alpha(1 - s^{\beta})^{\gamma} \,. \tag{3.2}$$

Generally, the α parameter controls the peakedness or breadth of the profile, and β has influence on the shape of the tail of the profile. [Figures here] But the two-power parameterization cannot model a hollow profile. Instead splines and line segment profiles are introduced with the flexibility to model a greater range of profiles. The splines and line segment profiles are parameterized by defining nodes with value at multiple s positions.

$$\begin{aligned} f(s) &= [f_0, f_1, ..., f_n] \\ s &= [s_0, s_1, ..., s_n] \end{aligned} \tag{3.3}$$

Usually the s and/or f values for one or multiple nodes are reconstructed in a equilibrium reconstruction.

3.3 V3FIT

While in the inverse problem, values of experimental observations for the system can be predicted with given parameters in the VMEC model, the inverse problem is solved with fitting code like V3FIT, in which experimentally observed data is used to infer the parameter of the model.

For a given equilibrium model characterized by the parameter vector, $\boldsymbol{p}$, the simulated diagnostic signals, $S^M(M(\boldsymbol{p}))$, are calculated and compared with the experimental observations, S^O. The mismatch between the modeled signals and experimental data is quantified by a χ^2 defined as:

$$\chi^2(\boldsymbol{p}) = \boldsymbol{e}(\boldsymbol{p}) \times \boldsymbol{e}(\boldsymbol{p}) = \sum_i W_i \left(\frac{S_i^O - S_i^M(M(\boldsymbol{p}))}{\sigma_i} \right)^2 . \tag{3.4}$$

Here, each element $e_i(\boldsymbol{p})$ consists of a signal uncertainty σ_i and weight W_i, in addition to the modeled signals and experimental data. Each element is differentiated with respect to the parameters to compute the Jacobian,

$$\boldsymbol{J} = \frac{\partial e_i(\boldsymbol{p})}{\partial p_j} . \tag{3.5}$$

The computed Jacobian is employed within V3FIT to determine an optimized path to a minimum value of χ^2.

The parameters of VMEC and auxiliary models determine the equilibrium solution and ultimately determine the computed model signals. Effectively, any parameter that affects the equilibrium may be reconstructed to a known upper and lower range. In the V3FIT code parameter ranges may be specified as either unconstrained, a particular value, or in terms of another parameter. The last type could be used for cases where a profile specified by splines is reconstructed. Sometimes, specifying a parameter range is necessary such as when someone wants to prevent the reconstructed s position of a node from crossing over the previous or subsequent node. Specified parameter ranges can also used as a constraint to avoid reconstructions that result in unphysical models.

3.3.1 Signals in V3FIT

Four classes of general signals are included in V3FIT, including diagnostic signals, geometric signals, prior constraints, and combinations of signals. All of these signals are implemented using an object-oriented programming technique that allows for quick implementation of new signals with minimal code impact.

The diagnostic signals include any signal determined from experimental observations. In axisymmetric configurations, all diagnostics may be effectively treated as being in the same toroidal plane. However, in non-axisymmetric 3D equilibrium reconstructions, the 3D position and orientation of the diagnostics becomes important, thus V3FIT takes into account the fully 3D geometry of a diagnostic. In the V3FIT code, measurements can be specified as point, line integrated, or volume integrated, depending on the nature of the diagnostics. Currently, V3FIT implements typical diagnostics found on magnetic confined experiments, including various types of magnetic diagnostics, soft x-ray cameras, interferometer systems and Thomson scattering. The implementation of the first two diagnostics will be discussed in detail in this thesis.

Geometric signals are used to model plasma-wall interactions with limiters and first walls, and are used to define the boundary of the plasma. Circularly and bar shaped limiters model the installed limiters at their measured toroidal and poloidal locations.

A prior is a pseudo-signal that fix known values of certain parameters in the reconstruction, assuming Gaussian distributions. By setting a prior, the χ^2 minimization can be biased to known quantity. The key usage of prior signals in this study is the implementation of prior signals is to use the location of the $q = 1$ surface extracted from analysis of soft x-ray emission of sawtoothing plasmas in equilibrium reconstructions.

Lastly, combination signals combine any of the various χ^2 contributions of other signals into a single signal subject to a specified operation. For reconstructions performed in CTH, each of the geometric limiter signals is combined into a single combination signal taking the maximum value of each signal. This insures that only the first limiter that is encountered is used to limit the boundary of the plasma.

Chapter 4

Equilibrium reconstruction with external magnetic diagnostics alone

4.1 Introduction

Magnetic diagnostics external to the plasma can provide measurements of the plasma current and plasma shape. They are routinely used to determine the shape and position of magnetized plasma[54,55], to measure the magnitude and distribution of currents within the plasmas[31], and to identify various MHD instabilities[56]. These measurements are essential for performing reconstructions in tokamaks[40,42,57], and reversed field pinches (RFP)[41]. The use of magnetic diagnostics in magnetically confined fusion experiments is reviewed by E. Strait[58].

The results in this chapter are obtained from measurements using full and segmented Rogowski coils, flux loops, and poloidal and radial B-dot pick up coils, all of which are used to measure poloidal and radial magnetic flux at multiple toroidal and poloidal locations. Measurements performed with these external magnetic diagnostics have been implemented in conjunction with the V3FIT code to determine a model for the magnetic equilibrium of the CTH plasma.

This chapter is organized as follows. The design and installation of the external magnetic diagnostics that are used for equilibrium reconstruction are described in Sec. 4.2. The method to incorporate magnetic diagnostic measurements in the V3FIT code is discussed in Sec. 4.3, including optimization of the model positions and orientations of the various probes (Sec. 4.3.1) and eddy current compensation (Sec. 4.3.2). Examples of 3D equilibrium reconstruction using magnetic diagnostics are then given in Sec. 4.4. Finally, limitations of equilibrium reconstructions using only external magnetic diagnostics are discussed in Sec. 4.5.

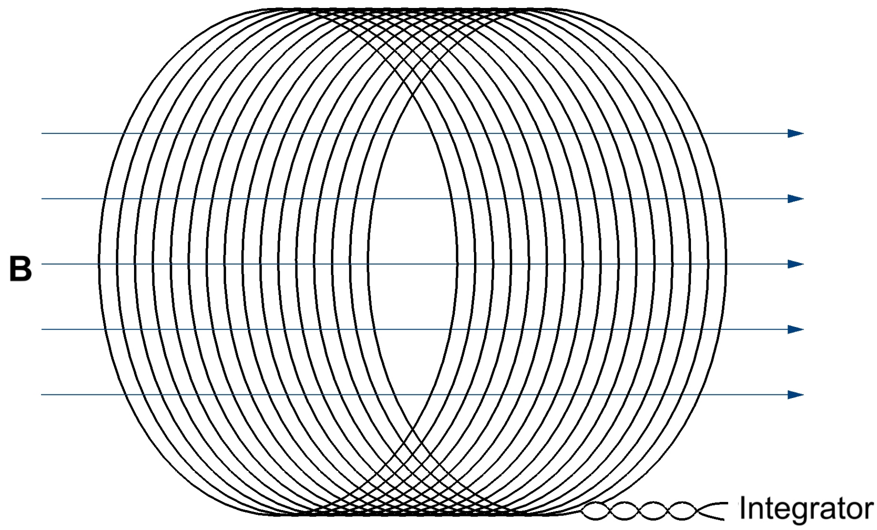

Figure 4.1: Magnetic coil with multiple turns

4.2 Magnetic diagnostics on CTH

Local and average magnetic flux is typically measured with passive wire loops or coils. The inductive voltage, V, produced by a loop with surface S and contour C in a magnetic field $\boldsymbol{B}$ is

$$\mathrm{V} = -\int_S \dot{\boldsymbol{B}} \cdot d\boldsymbol{S} = -\frac{d}{dt}\int_S \boldsymbol{B} \cdot d\boldsymbol{S} = -\frac{d\Phi}{dt}\,, \tag{4.1}$$

which gives the time derivative of the total induced magnetic flux, Φ, through the area $\boldsymbol{S}$ of the loop. To determine Φ, the signal from the loop is electronically integrated:

$$V_{\mathrm{meas}} = \int_{t_0}^{t} V dt = -\int_S \boldsymbol{B} \cdot d\boldsymbol{S} = -\Phi\,. \tag{4.2}$$

To increase the level of the signal and accuracy of the measurement, one typically winds a diagnostic coil with multiple turns as in Fig. 4.1 to increase the induced voltage for a given local field. The magnetic flux through a solenoidal coil with cross section area ,A, number of turns per unit length of n and length l, is:

$$\Phi = n\int_l\int_A dA\boldsymbol{B} \cdot d\boldsymbol{l} = nA\int_l \boldsymbol{B} \cdot d\boldsymbol{l} = V_{\mathrm{meas}}\,. \tag{4.3}$$

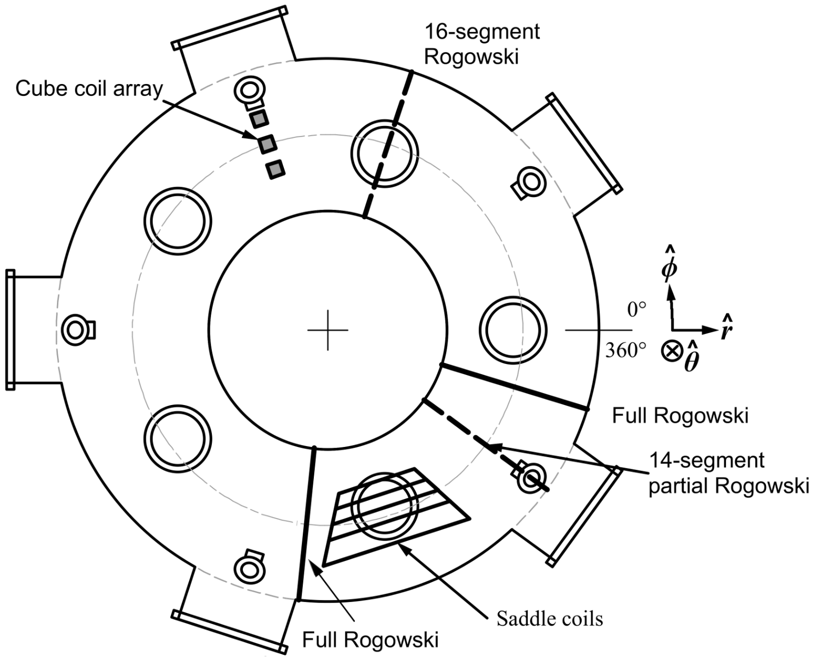

Figure 4.2: Top view of CTH vessel showing locations of the magnetic diagnostics used for reconstruction. The saddle coils have a matching set on the bottom of the vessel.

Here $\int_l \boldsymbol{B} \cdot d\boldsymbol{l}$ is the line integral of magnetic field $\boldsymbol{B}$ averaged over the cross-section of the coil. For coils with smaller dimensions than the scale length of variation of the magnetic field, the measured voltage may provide a direct measure of the local magnetic field.

$$V_{\text{meas}} = NAB\,. \tag{4.4}$$

Here $N = nl$ is total turns of wire. Based on Eq. 4.4, we can use small $\dot{B}$ coils to measure local magnetic fields.

The location of the magnetic diagnostics that are used for equilibrium reconstruction is shown in Fig. 4.2. They include full and segmented Rogowski coils, saddle coils or flux loops and magnetic $\dot{\boldsymbol{B}}$ pickup coils. A total of over 50 magnetic diagnostics are routinely used to provide data for reconstructing CTH plasmas. Details of the construction, calibration and position measurement of these magnetic diagnostics are given in the following sections.

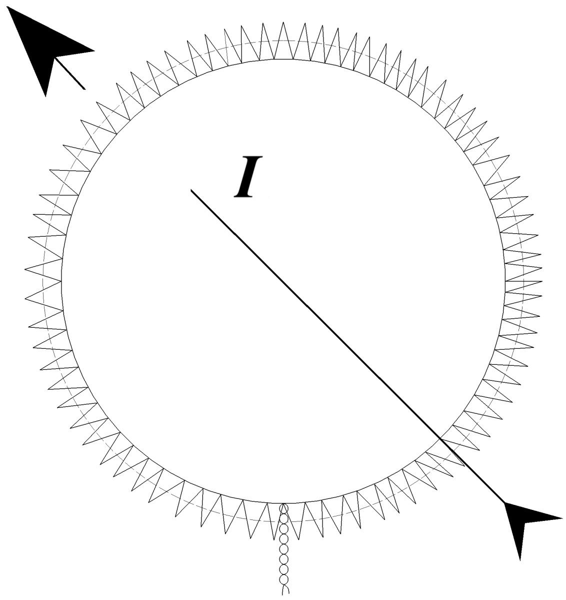

Figure 4.3: Full Rogowski coil encloses the current to be measured. The coils are wound over a return lead and the leads are twisted to minimize measurement of flux.

4.2.1 Rogowski coils

A Rogowski coil consists of a solenoid coil or set of solenoid coils connected in series that closes on itself or not. An illustration of a full Rogowski coil is shown in Fig. 4.3. It is used to measure the total current I that flows through the area created by the closed solenoidal loop.

$$\frac{\Phi}{nA} = \oint_l \boldsymbol{B} \cdot d\boldsymbol{l} = \mu_0 I \tag{4.5}$$

On CTH and other current-carrying plasma experiments, full Rogowski coils are used to measure the total toroidal plasma current.

Information of the spatial variation of the current or distribution may be obtained using separate partial solenoid coils, which measure the distribution of the poloidal magnetic flux. A segmented Rogowski coil is constructed as a set of partial coils connected in series. An example of 14-segment Rogowski coil is shown in Fig. 4.4.

All Rogowski coils on CTH are fabricated by winding polyimide-coated (Kapton) 30 gauge copper magnet wires onto a solid $6.35\,\mathrm{mm}$ diameter Teflon® core. To minimize pick up of the toroidal flux in uncompensated leads, the solenoidal coils are wound in two layers.

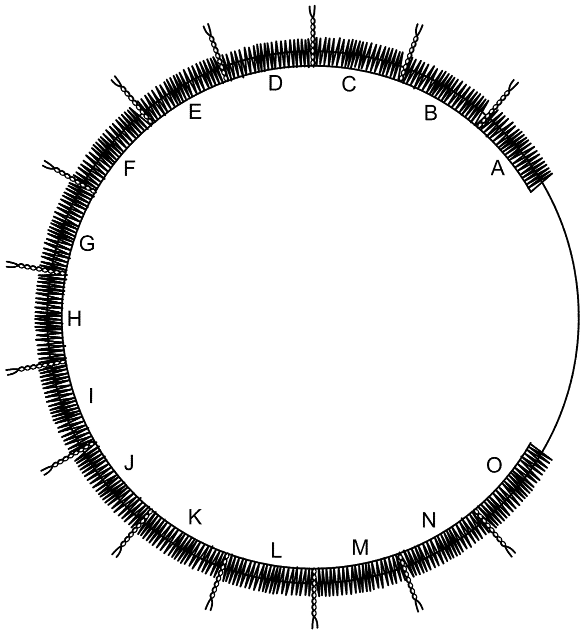

Figure 4.4: 14-segment Rogowski coil is vertically symmetric with each segment spanning a fixed 20° poloidal angle. All leads are twisted to avoid unwanted pick-ups.

The return wire is wound back as the second layer of coil on top of the first so that the effective closed toroidal flux loop is eliminated. The pair of leads from each coil are twisted to reduce the additional flux pickup.

All internal coils are mounted on the interior wall of the vacuum vessel. Fig. 4.5 shows one full and one segmented Rogowski coils inside the vacuum vessel. Rogowski coils are covered by thin Teflon® sheet for electrical isolation. Strips made of 316 stainless steel with thickness of $0.08\,\mathrm{mm}$ are used to install coils in the desired poloidal cross-section. Each of the full Rogowski coils was calibrated prior to installation by measuring the output voltage while enclosing an AC current, measured using a $0.1\,\Omega$ resistor with a resistance tolerance of 0.1%.

A full Rogowski coil inside the vacuum vessel installed at a toroidal angle of $\phi = 264^\circ$ is used to measure the total plasma current, and a separate full Rogowski coil exterior to the vacuum vessel at $\phi = 342^\circ$ is used to determine the vacuum vessel current as being the difference between it and the interior coil. Signals from segmented, or partial poloidal Rogowski coils allow for some reconstructions of the plasma current profile. A 16-segment Rogowski coil is located at $\phi = 96^\circ$, and a 14-segment coil is at $\phi = 324^\circ$.

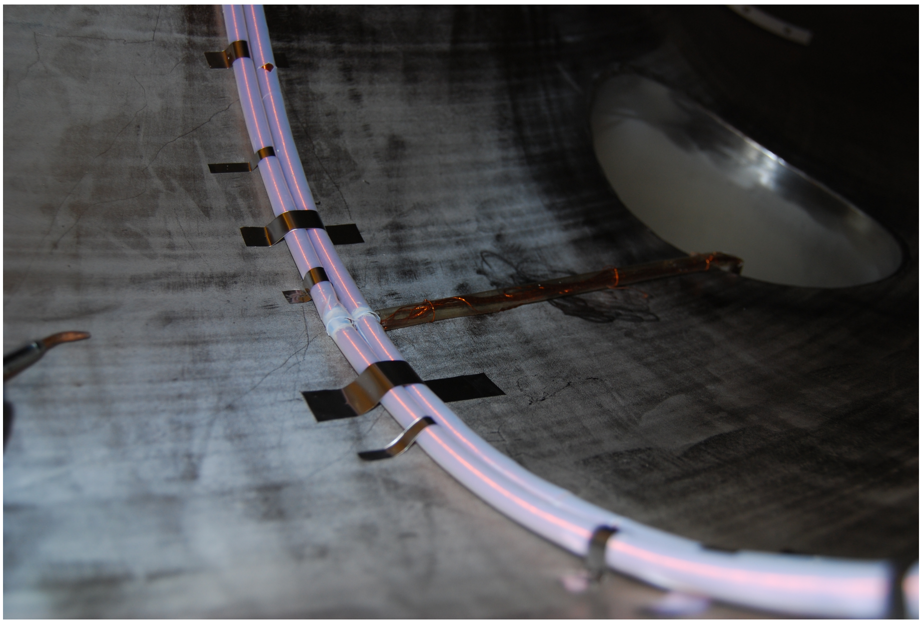

Figure 4.5: One full and one segmented Rogowski coils mounted on the interior vacuum vessel wall. Rogowski coils are covered by thin Teflon® sheet for electrical isolation. Stainless steel strips are used to fix coils in desired position.

After installation, the position and orientation of the coils are measured with a coordinate measuring machine (CMM). Considering the 3D shape of Rogowski coils, simple point measurements along the loop are not accurate enough to describe the actual position of the coil loop. Instead, each segmented coil is geometrically represented by the coordinates of the center of 8 evenly divided cross-sections, as shown in Fig. 4.6. The coordinates of 5 points on the outer layer of each cross-section are measured using the CMM. The average of their coordinates is taken to model the position of the center of the cross-section. After position measurements, all coils and cables are covered by stainless steel sheet to provide electrostatic shielding, as well as protection from erosion and metal deposition during plasma discharges, glow discharge cleaning, and titanium gettering.

4.2.2 Saddle coils

Radial magnetic fluxes are measured with a set of saddle coils (flux loops). They are installed at $\phi = 288°$, with one section installed at $90°$ above the mid-plane and a matching set installed at $90°$ below the midplane.

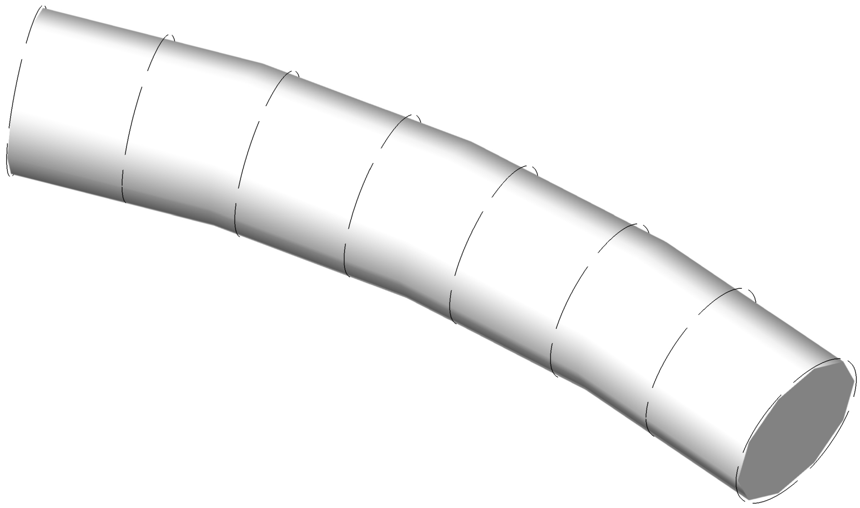

Figure 4.6: Sketch of partial Rogowski coil. CMM measurements are made at 8 evenly divided cross-sections.

The location of these saddle coils are optimized through the calculation of the so-called signal effectiveness. As discussed in Appendix C, the signal effectiveness of a diagnostic is calculated by determining the sensitivity of the diagnostic's quantitative response to a reconstruction model parameter. The intent is to ascertain, prior to construction, which diagnostics will be most effective in reconstructing a particular parameter. Here, we use the capability of V3FIT to calculate the signal effectiveness of simulated saddle coils to the current profile width parameter α. The current profile is parameterized as

$$I'(s) = I_0(1 - s^{\alpha})^6 \,. \tag{4.6}$$

A smaller value α represents a more peaked profile while a profile with larger α is broader.

For this calculation, a full field period with poloidal extent from $0°$ to $180°$ and toroidal extend from $0°$ to $72°$ is populated with 120 flux loops on a 12×10 grid. For a given VMEC equilibrium, the signal effectivenesses of each of the 120 simulated loops is calculated with respect to parameter α. The calculation is repeated using 20 different model plasmas with different plasma currents, densities and external coil currents. A contour plot of the average signal effectiveness is shown in Fig.4.7. The color represents the strength of the signal effectiveness.

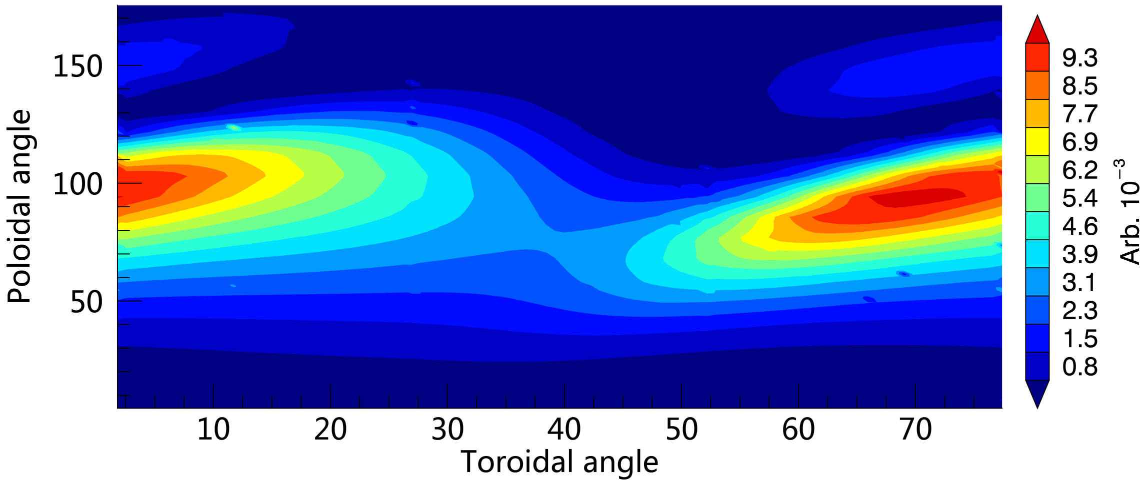

Figure 4.7: Contours of predicted signal effectiveness of small saddle coils as a function of their position within a field period. The red color denotes the highest effectiveness, and blue the lowest. The values at the toroidal location $0°$ and $72°$ match because CTH system has a five-fold field periodicity.

These simulations indicate that a small set of saddle flux loops mounted on the inboard side of the vacuum vessel near $\phi = 0°$ (close to the top or bottom vertical port) would be most effective in reconstructing the current profile parameter α. The actual saddle coils were placed in these areas, as shown in Fig. 4.2.

Fig. 4.8 shows one frame of the saddle coils before installation on the inner wall of the vacuum vessel. The frame of the saddle coil is made of stainless steel tubes and bars. The latter are bent to fit to the curved wall of the vacuum vessel. Each frame consists of four flux loops, each of which contains three turns of Teflon® coated cooper wire with a diameter of $0.5\,\mathrm{mmm}$, wound within the stainless steel tubes. The leads of each loop are tightly twisted to reduce flux pick-up. The two frames are fastened to the marked position of the interior vacuum vessel wall with strips of shim stock. After installation, the coordinates of multiple points along each flux loop are measured with the CMM.

4.2.3 Magnetic pickup coils

Local measurements of poloidal and toroidal magnetic field, B_θ and B_ϕ, are made with a set of 6 small coils wound onto cubical Teflon® forms. Kapton-coated 30 AWG copper wire is wound on the form, in two perpendicular directions to measure time derivative of the radial and

Figure 4.8: One frame of the saddle coils on the bench. Each frame consists of 4 loops.

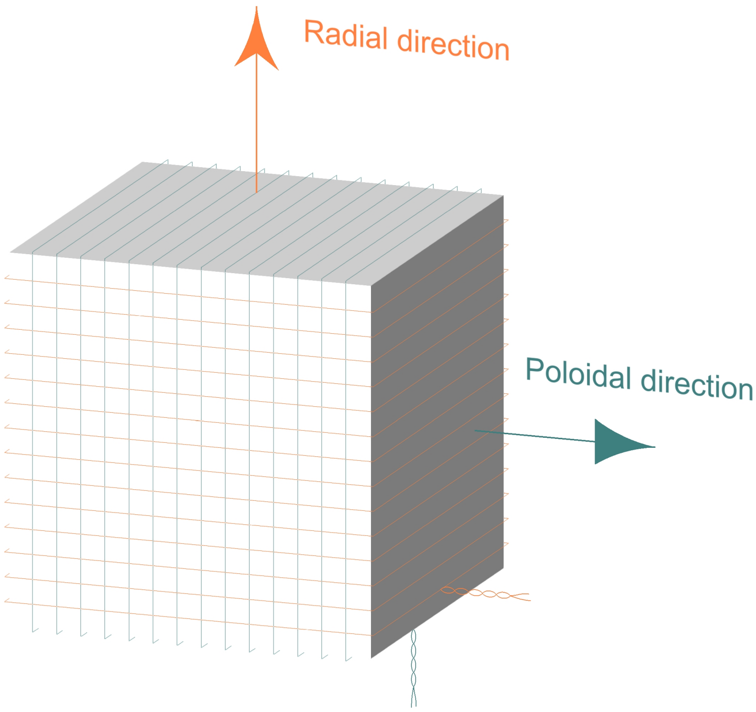

Figure 4.9: Cube coils are wound on cubic Teflon® forms, $13.5\,\mathrm{mm}$ on a side. Polyimide-coated (Kapton) 30 AWG copper magnet wire is wound on the form, in two perpendicular directions to measure $\dot{B}_\theta$ and $\dot{B}_\phi$

poloidal components of the magnetic field, $\dot{B}_\theta$ and $\dot{B}_\phi$. They are distributed along a poloidal cross-section at $\phi = 108°$. One set of 3 cube coils is installed at $\theta = 60°$, $90°$ and $120°$. Another matching set is installed at vertically symmetric positions about the mid-plane. In addition to their use in reconstruction, these coils are also used to measure the vertical drift of ohmic plasmas[34]. These coils are wound on cubic Teflon® forms with $13.5\,\mathrm{mm}$ edges as show in Fig. 4.9. As with the Rogowski coils developed for this thesis, these coils are wound with double layers to minimize stray pickup.

From Eq. 4.1, we get the voltage response of the coil to be:

$$\begin{aligned} V &= -\frac{d\Phi}{dt} \\ &= -NA\frac{dB}{dt}\,. \end{aligned} \tag{4.7}$$

Here we assume that the magnetic field does not change much over the volume of the coil. The product NA measures the response of the coil to the varying magnetic field. The NA value of

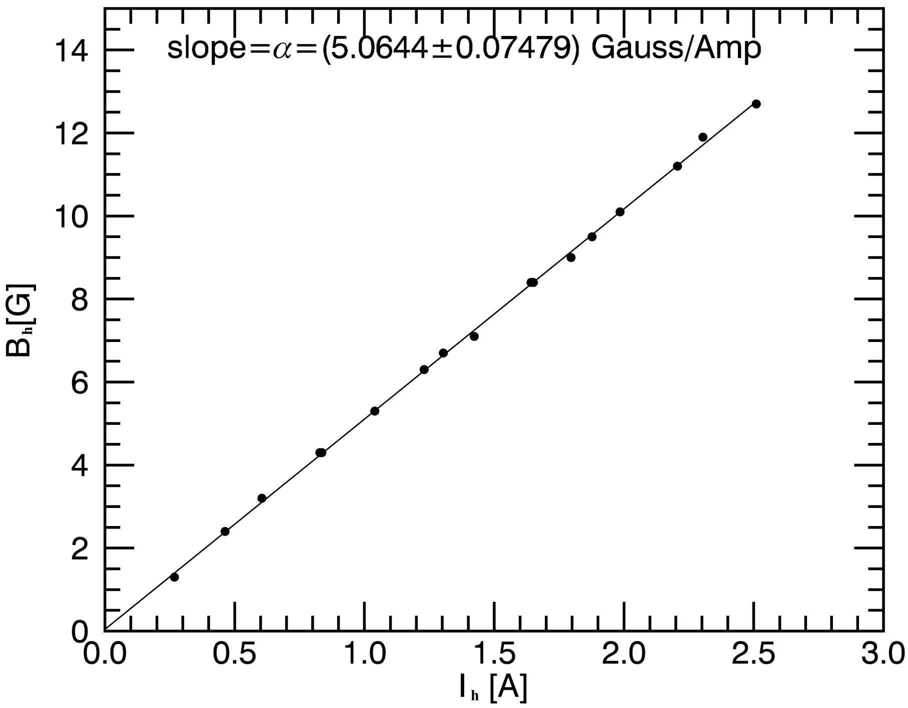

Figure 4.10: Calibration of the Helmholtz coil is done with a Hall probe and varying DC currents. The vale of parameter α is given by the slope of the fitted line.

each coil is calibrated using the uniform magnetic field generated by a Helmholtz coil. To do this, the Helmholtz coil is first calibrated with different DC currents and a Hall probe with a nominal accuracy of $0.2\,\mathrm{G}$ to determine the parameter α in Eq. 4.8.

$$B_{\mathrm{h}} = \alpha I_{\mathrm{h}} \tag{4.8}$$

Here, I_{h} is the DC current that goes through the Helmholtz coil. The Hall probe measures the corresponding magnetic field, B_{h}, in the center of the Helmholtz coil. The calibration data and fitted value of α are shown in Fig. 4.10.

To calibrate the $\dot{B}$ coil, it is suspended in the center of the Helmholtz coil. The orientation of the coil is adjusted so that its axis lies collinear with the axis of the Helmholtz coil and the its cross-section is perpendicular to the magnetic field in the center of the Helmholtz coil. The Helmholtz coil is powered by a function generator with sinusoidal voltage output. The current through the Helmholtz coil is determined by measuring the voltage drop, V_r, across an high accuracy resistor R $(0.1\Omega, 0.1\%)$ in series with the Helmholtz coil The response of the $\dot{B}$ coil,

V_c, is measured across the leads of the coil. For a given sinusoidal magnetic field ,B, with frequency ,f, $B = B_0 \sin(2\pi f t + \delta)$, and the response V_c is:

$$\begin{aligned} V_c &= -NA\frac{dB}{dt} \\ &= -2\pi f NAB_0 \cos(2\pi f t + \delta)\,. \end{aligned} \tag{4.9}$$

Here we measure the peak value of V_r and V_c using an oscilloscope. Using the relation, $B_0 = \alpha I_0 = \alpha\frac{V_r}{R}$, Eq. 4.9 turns to:

$$V_c = 2\pi f NA\alpha\frac{V_r}{R}\,. \tag{4.10}$$

Then we can solve for NA as :

$$\begin{aligned} NA &= \frac{R}{2\pi\alpha} \times \frac{\frac{V_c}{V_r}}{f} \\ &= \frac{R}{2\pi\alpha} \times \beta\,. \end{aligned} \tag{4.11}$$

Experimentally, the frequency f of the power supply was scanned from $200\,\mathrm{Hz}$ to $2000\,\mathrm{Hz}$. The slope, $\beta = \frac{\frac{V_c}{V_r}}{f}$, is obtained with a linear fit of the calibration data. An example of the calibration result of one of the pick-up coils is shown in Fig. 4.11. Then with Eq. 4.11 and the calibrated α value, NA is calculated. In this case, $NA = 81.46 \pm 0.91\,\mathrm{cm}^2$.

After the calibration, the six cube coils were installed in position with one face against the inner wall of the vacuum vessel. They were carefully aligned to make sure that for each cube coil the poloidal coil only measures the poloidal flux and the radial coil only measures the radial flux. After installation, the position and orientation of all coils was measured with a CMM. Specifically, the coordinates of the 8 vertices of each cube form were measured, from which we can calculate the center of the cube as well as the radial and poloidal vectors.

All twisted pair conductors from magnetic diagnostics are fed through the nearest vacuum vessel ports with a bayonet type multiple-pin connector, which brings the measured signals to the analog integrator boards. The integration circuit design was provided by John Sarff of the University of Wisconsin in Madison and Sterling Scientific. Then integrated signals are amplified with specified gains and directed to the data acquisition system.

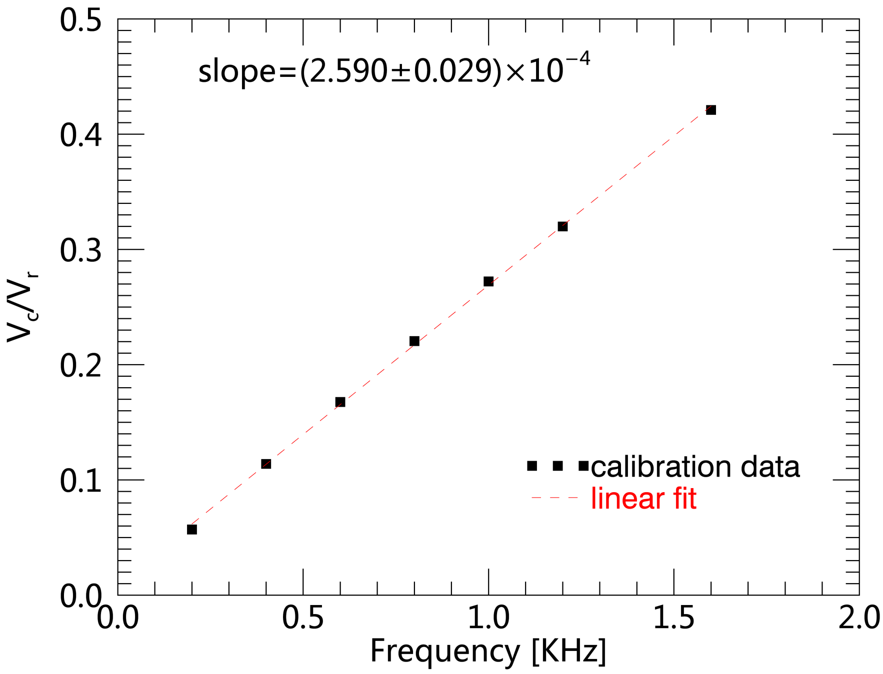

Figure 4.11: The ratio of the voltage output from the pick-up coil, V_c, and the voltage drop across the current resistor, V_r, is plotted against the frequency, f, of the magnetic field. A linear fit of the calibration data gives the value of slope with uncertainty.

4.3 Implementation of magnetic diagnostics in V3FIT

Experimentally, the signal from a particular magnetic diagnostic results from a combination of the magnetic flux due to the plasma current, and that from the external magnetic coil currents and eddy currents in the vacuum vessel and other conducting structures. Extracting the actual plasma contribution, S^{plasma}, from the net signal, S^{total}, is important for V3FIT to optimize the simulated plasma equilibrium.

$$S^{\text{plasma}} = S^{\text{total}} - S^{\text{ext}} - S^{\text{eddy}} \tag{4.12}$$

Here S^{ext} represents the signal due to external coil currents, and S^{eddy} is the signal contribution from eddy currents. As a result, great efforts have been taken to account for magnetic flux from external currents and eddy currents. Sec. 4.3.1 describes how the geometry of the magnetic diagnostics was optimized in order to correctly subtract signal contributions due to external coil currents. The details of eddy current modeling and signal compensation are discussed in Sec. 4.3.2.

4.3.1 Optimization of geometry of magnetic diagnostics in V3FIT

The magnetic signal measured by a magnetic diagnostic due to the external coil currents depends on the amplitude of the currents in the external coils and the response functions of the diagnostic to the external coils (i.e. the mutual inductance between the diagnostic coil and the external coils).

$$S^{\mathrm{ext}} = \sum_i M_i^{\mathrm{ext}} I_i^{\mathrm{ext}} \tag{4.13}$$

Here M_i^{ext} is the mutual inductance, between the diagnostic coil and the ith external coil current, I_i^{ext}. The external coil currents are measured using shunts which have a specified accuracy of 0.5%. M^{ext} completely depends on the relative geometry between the diagnostic and the external coil. Thus accurate position and orientation of the diagnostic is required to calculate correct responses due to external currents.

With the exception of several full Rogowski coils, all magnetic diagnostics used for reconstructions are installed inside the vacuum vessel. As described in the details above, the positions and orientations of the diagnostics were measured with the CMM during their installation to a nominal accuracy of $0.25\,\mathrm{mm}$. However, due to the finite size and three-dimensional shape of the diagnostics, the CMM measurements often appear to be insufficient to model the position and orientation of a diagnostic with the requisite accuracy. Accordingly, the mutual inductances of the magnetic diagnostics to the external coils are further refined by experimental calibration.

This is accomplished by discharging each of the external coils separately (with all other coils open-circuited) and measuring the responses of the diagnostics when the coil current is ramped to a steady value. Once the exciting current has reached its constant programmed value, all eddy current can be expected to have died away. The mutual inductance of the ith diagnostic to the jth external current is calculated as:

$$M_{ij} = \frac{S_{ij}}{I_j} \tag{4.14}$$

Experimentally, the external current and corresponding diagnostic signal are averaged over a time window of $100\,\mathrm{ms}$. For each external coil, mutual inductances are calculated using a set of testing currents with different amplitudes. The difference between measured mutual inductances are within 0.5%. The average is used as the final calibration data.

Fig. 4.12 shows an example of the calibrations when only the HF coil is powered to a desired current around $4.5\,\mathrm{KA}$. Also plotted in the graph is the response signal from one segment of the 14-segment Rogowski coil. The HF coil current rises to a steady value near $t = 1.6\,\mathrm{s}$.

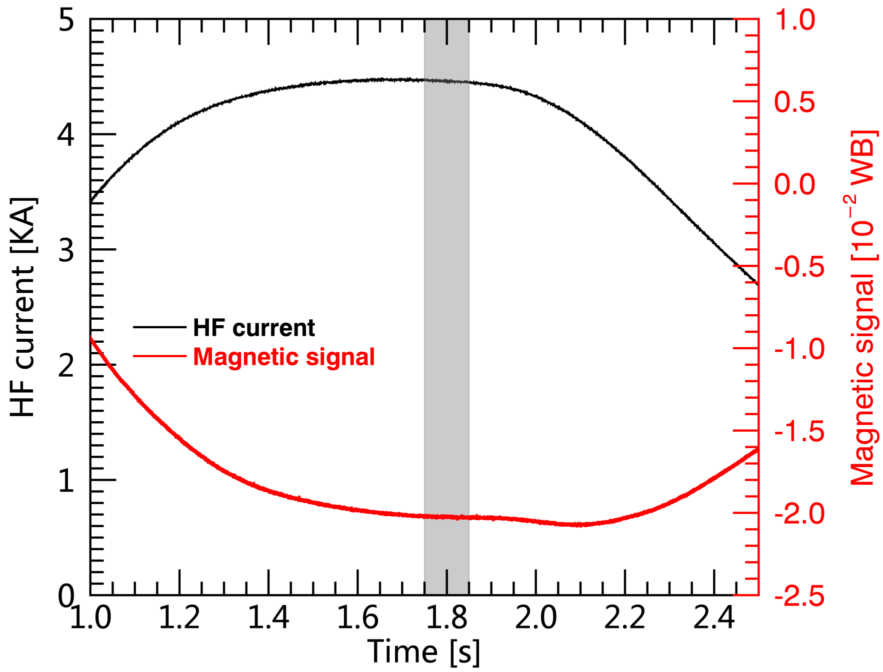

Figure 4.12: The HF current (black) and corresponding response from one channel of the 14-segment Rogowski coil (red). The average mutual inductance between this diagnostic and the HF coil is calculated during the $100\,\mathrm{ms}$ time window (gray stripe).

An averaging window from $t = 1.75\,\mathrm{s}$ to $t = 1.85\,\mathrm{s}$ is chosen to calculate the mutual inductance between this diagnostic and the HF coil. The same process is performed for all diagnostic channels and external current (HF, TF, TVF, SVF, OH and RF) coils.

For the purpose of reconstruction, the location of the diagnostics are then optimized by minimizing the mismatch between the mutual inductances from experimental calibration and the ones from the simulated geometry model in V3FIT. The quantified difference is defined as:

$$\delta^2 = \sum_{i,j} \left(\frac{M_{ij}^{\text{Model}} - M_{ij}^{\text{Exp}}}{\Delta M_{ij}^{\text{Exp}}} \right)^2 , \tag{4.15}$$

where M_{ij}^{Exp} represents the experimental calibrated mutual inductance of the i^{th} magnetic diagnostic to the j^{th} external current source, and M_{ij}^{Model} is the modeled mutual inductance calculated using the positional measurements from a CMM. The model locations may be adjusted by as much as $1\,\text{mm}$ from the measurements given by the CMM in order to minimize the δ^2 in Eq. 4.15. This model is assumed to give the most reliable description of the installed magnetic diagnostics.

Fig. 4.13 shows an example of optimized results of the mutual inductances of a segment of the 14-segment Rogowski coil to the HF coil current. It is clear that most of the blue squares

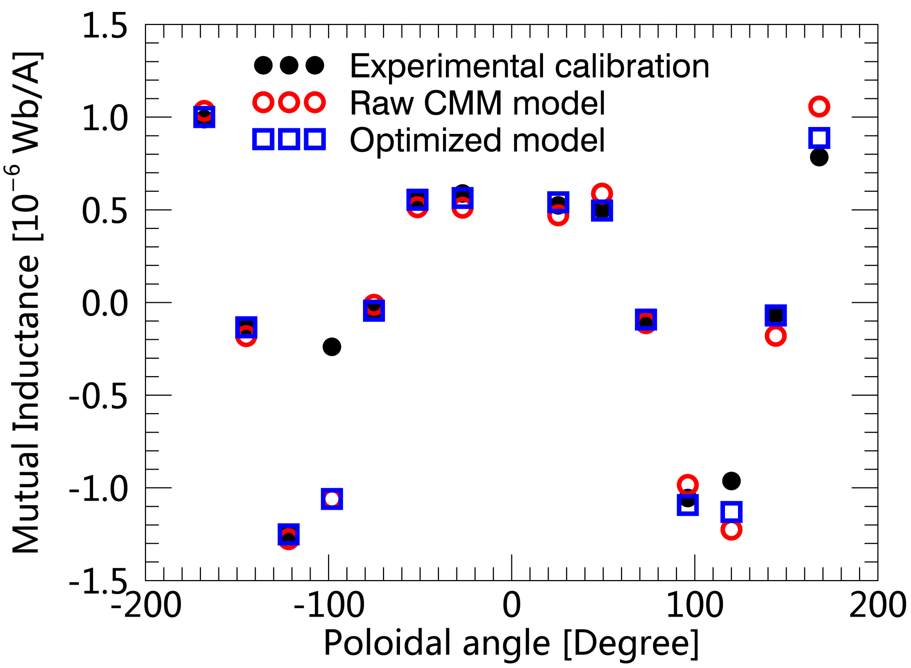

Figure 4.13: Comparison of mutual inductances of one segment of the 14-segment Rogowski coil to the HF coil. The mutual inductances from experimental calibration are shown with black dots. Calculated mutual inductances from initial CMM measured positions are shown in red circles. The optimized results are plotted in blue squares.

are closer to the black dots, which indicates that the mutual inductances from optimized model are a better representation of the experimental calibrated values. However, even after the optimization, the mutual inductance from one segment of the Rogowski coil close to $\theta = -100^\circ$ is still far from the experimental calibration. This diagnostic might already be damaged, and is neglected in the equilibrium reconstruction.

4.3.2 Eddy current compensation

In addition to the desired diagnostic signals from external coil currents and plasma current, eddy currents within conducting structures surrounding the plasma may also lead to magnetic signals that must be compensated for. Two types of eddy currents on CTH are investigated: eddy currents in the electrically continuous vacuum vessel, and in the aluminum helical coil frame. The distribution of these currents depends on the source of magnetic flux that drives them. Also, the magnitudes of these eddy currents are time-dependent with differing decay rates.

Although each of the magnet coils drives eddy currents in the vacuum vessel and coil frame, the OH current is the only external coil current that varies significantly during the time when the plasma is generated. The equilibrium currents of the HF, TF, and VF coils are essentially constant during the plasma discharges. The current driven in the vacuum vessel during the OH discharge has been modeled by James Bialek of Columbia University using his VALEN code[59]. The vacuum vessel current distribution is modeled as a toroidal grid as shown in Fig. 4.14. This grid model computes the currents driven within the toroidal shell, and around and within the various ports.

The results of the VALEN code serve as a basis for a simpler filament model of the vacuum vessel currents to be used in the V3FIT code. In this model the induced current distribution is modeled as a set of 24 circular toroidal filaments that lie within the vacuum vessel, poloidally separated by 15° as shown in Fig. 4.15. The vacuum vessel wall thickness is known to be a function of poloidal angle and varies as much as $1.2\,\mathrm{mm}$ because of the method of fabricating the vacuum vessel. This thickness variation is used to vary the relative electrical resistances of the filaments. The ratios of the currents in the individual filaments are modeled from a

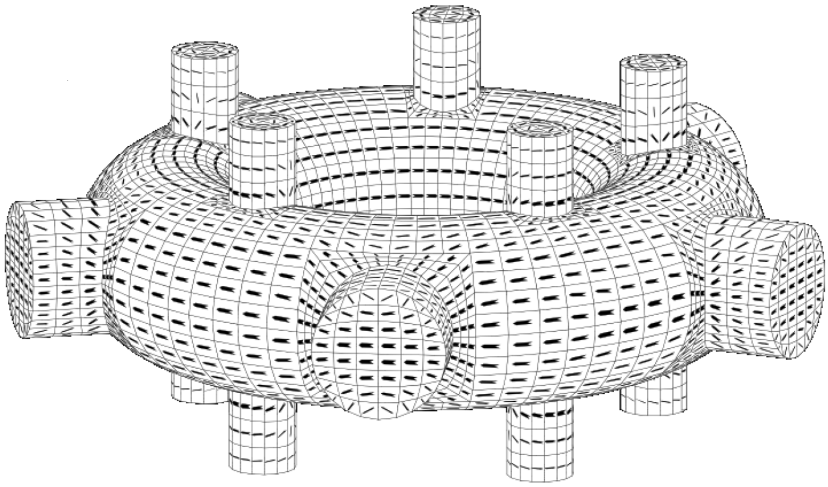

Figure 4.14: Mesh model of eddy current distribution using VALEN code

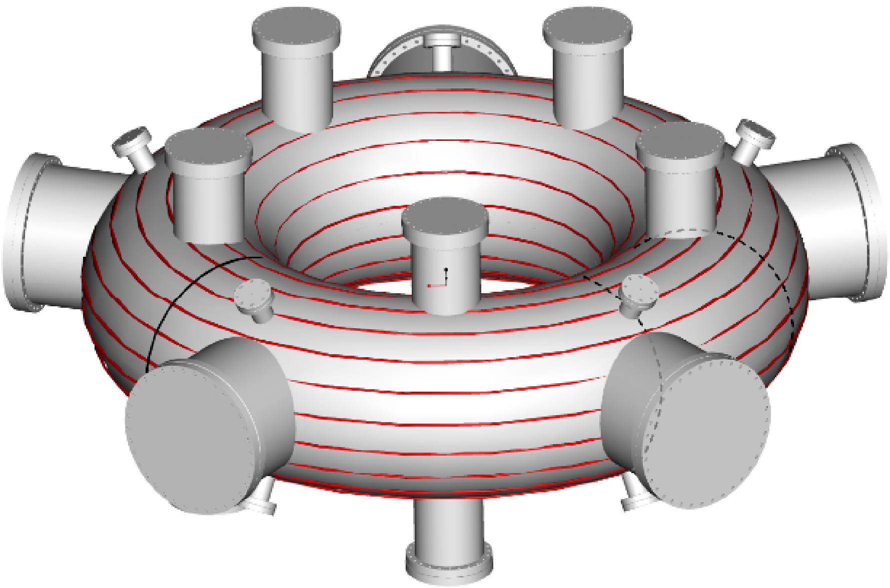

Figure 4.15: The eddy current driven in the vacuum vessel are modeled as a set of 24 toroidal filaments that lie on the vacuum vessel, equally spaced in poloidal angle, shown in red circles.

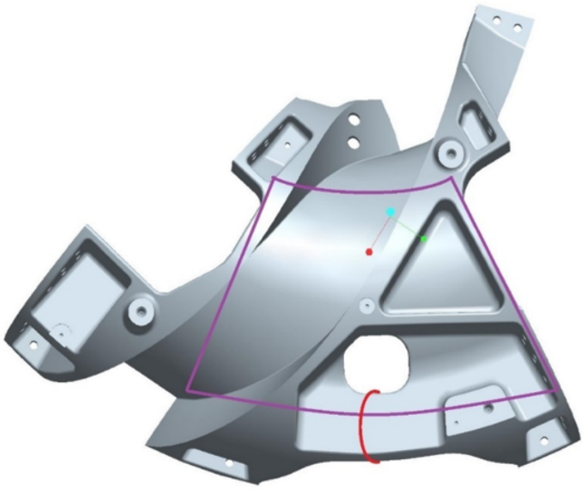

Figure 4.16: A rendering of a helical coil frame section showing the location of the saddle coil (purple) used to model the eddy current in the frame and the Rogowski coil (red) used to measure the eddy current in one portion of the frame.

calculation based on the resistivity of the Iconel625® vacuum vessel. The sum of the currents is set to the total measured vacuum vessel current.

Additional eddy currents are driven in the helical coil frame, which consists of ten identical interlocking but electrically-isolated cast aluminum frame pieces as shown in Fig. 4.16. The rigid frame system provides accurate positioning of the helical coil during the fabrication of the CTH device and adequate support during operation. Due to the complex shape of helical coil frame, modeling of the eddy currents within these frames is challenging[60]. As an approximation, the eddy current flowing though each helical coil frame is geometrically modeled as a saddle coil, as illustrated in Fig. 4.16. A physical opening in each coil frame allows a major portion of the eddy current in each frame piece to be measured by Rogowski coils threaded through these openings.

The relative contributions of the eddy currents to the magnetic diagnostic signals are assessed with magnet current pulses used in CTH discharges, both with and without induced plasma current. The signal from one segment of the 14-segment Rogowski coil is shown in Fig. 4.17. The response of the diagnostic coil to vacuum fields alone are shown in Fig. 4.17(a). It should be noted that the fluxes from the main field coils (HF, TF, TVF) have been set to zero

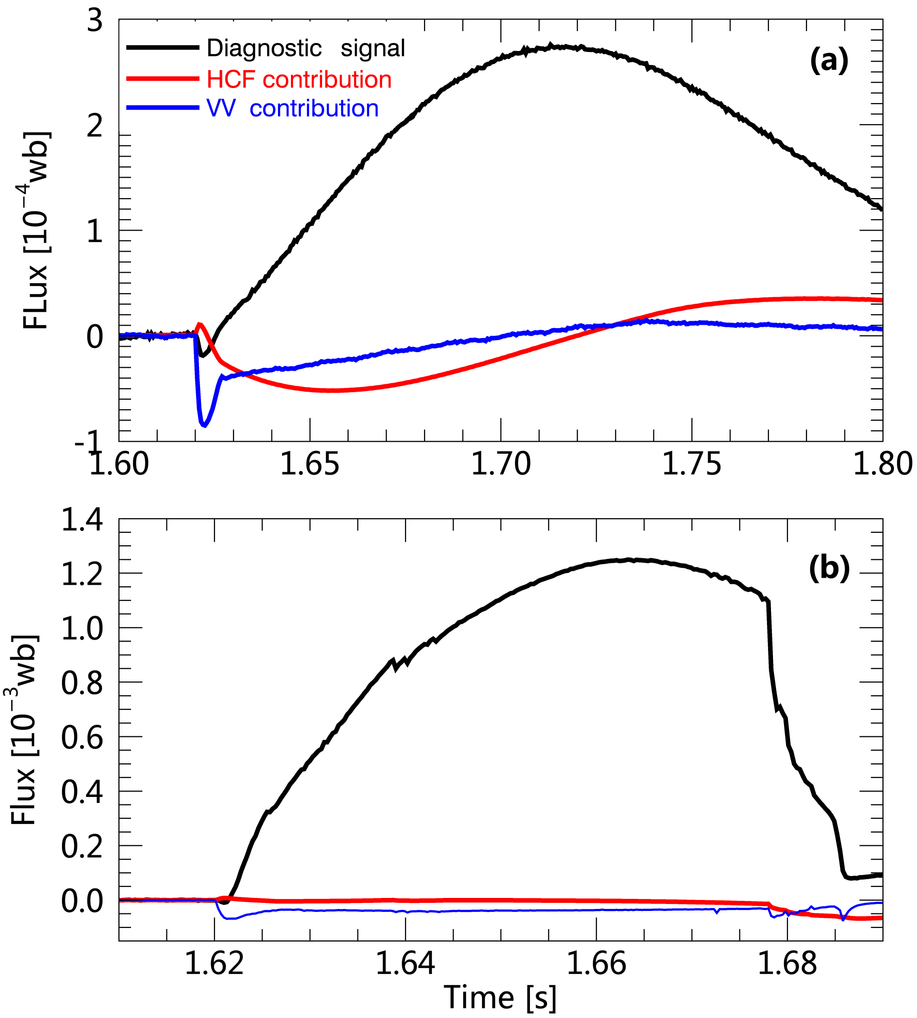

Figure 4.17: (a) Time evolution of the computed ohmically-induced eddy current contribution of the helical coil frame (red) and vacuum vessel (blue) currents, and measured magnetic signal from one of the 14-segment Rogowski coil channels (black) with vacuum fields only. (b) Corresponding time evolution when plasma current is present. Note the change in time and amplitude scales between panels (a) and (b).

just prior to the ohmic current pulse that starts at $t = 1.62\,\mathrm{s}$, so the diagnostic response displayed in the figure mainly reflects the flux from the ohmic transformer, the eddy currents, and small time-dependent changes in the equilibrium vertical field. The calculated contributions to this signal from the eddy currents in the vacuum vessel and helical coil frames, computed from the measured currents and their modeled mutual inductances to the diagnostic, are also plotted. The relative contributions from the vacuum vessel and helical coil frame to the net diagnostic signal of the vacuum-only signal (after excluding the signals from the main magnet coils) are on the order of 10%. The same diagnostic response is shown in Fig. 4.17(b) for a discharge with plasma current $I_\mathrm{p} = 62.3\,\mathrm{kA}$. In this case, the computed eddy current contributions reduce to as low as 1% of the total signal during the plasma current peak. While accounted for in V3FIT modeling, the signals resulting from eddy currents nonetheless represent only relatively minor corrections to the diagnostic signals.

Besides external current contributions and eddy current compensation, drifts and offsets induced by the analog integrator and amplifier are also subtracted from the raw measurements S^raw:

$$S^\mathrm{total} = S^\mathrm{raw} - \left(S^\mathrm{offset} + R^\mathrm{drift} t\right). \tag{4.16}$$

Here the offset, S^offset, and drift rate, R^drift, are obtained by computing a linear fit of the integrated signal prior to the time when the external magnetic coils are triggered.

After all these corrections to the raw signals, the final resulting plasma responses S^plasma are accounted for in V3FIT to reconstruct the plasma equilibrium.

Fig. 4.18 shows comparisons between simulated signals from reconstructed equilibrium and experimental measurements from the 16-segment Rogowski coils and saddle coils. The observed and model signals match well.

4.4 Reconstructions with external magnetics

To achieve convergence, the free-boundary VMEC equilibrium solver must be provided with a boundary condition of the total toroidal flux enclosed in the plasma. The equilibrium solver also requires the plasma pressure profile, and either the current density profile or the rotational

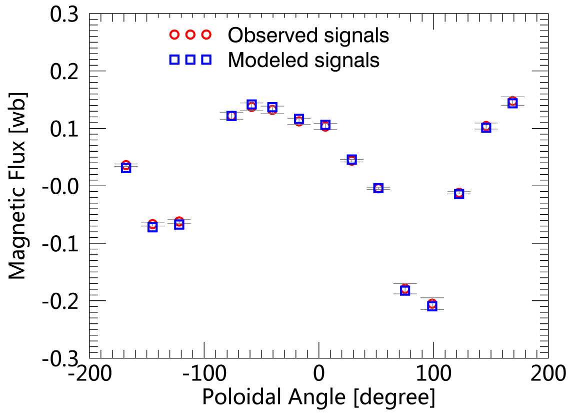

(a) 16-segment Rogowski coils

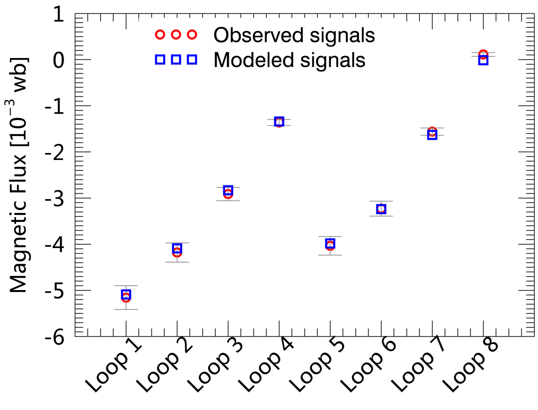

(b) Saddle coils

Figure 4.18: Comparison of experimental measurements and simulated signals from reconstructed plasma equilibrium for 16-segment Rogowski coils and saddle coils.

transform profile as functions of the normalized toroidal flux. The known external currents and modeled eddy current distributions complete the required specific data. The three-dimensional locations of the actual limiters in CTH are modeled in V3FIT to act as a signal to fit the maximum toroidal flux within the plasma under the assumption that the last closed flux surface cannot extend past any limiter surface. The reconstruction process returns the toroidal magnetic flux enclosed by the plasma, the edge safety factor $q(a)$, and the plasma current profile, subject to the parametrization allowed by the model.

4.4.1 Profile parameterization

A two-power model is employed for the current density and pressure profiles in the reconstructions presented here. It has the general form:

$$A(s) = A_0(1 - s^{\alpha})^{\beta}\,, \tag{4.17}$$

where A_0 is a scaled amplitude; α and β determine the shape of the profile; s is the normalized toroidal flux used in VMEC, a radial-like coordinate with $s = 0$ at the magnetic axis and $s = 1$ representing the last closed flux surface. In this thesis, the current profile is reconstructed while the pressure profile is held fixed because it is not yet measured in CTH.

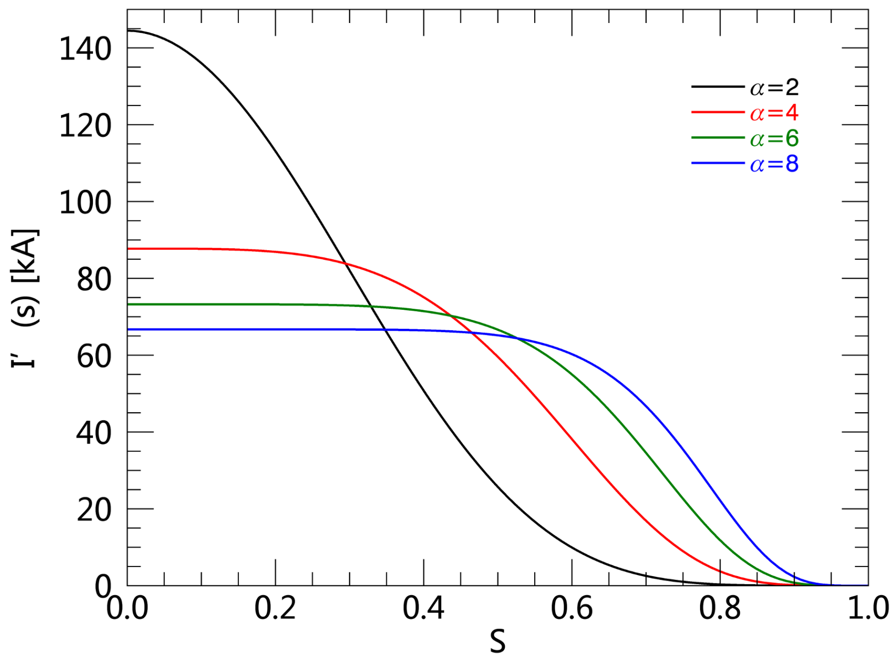

Figure 4.19: Current density profiles determined by the parameter α. Smaller values of α correspond to narrower profiles.

The current profile parametrization is based on a single fitting parameter α, as shown in Eq. 4.18.

$$I'(s) = I_0(1 - s^{\alpha})^6 \tag{4.18}$$

Reconstructions performed to fit both α and β yielded uncertainties two or three times larger than the reconstructed values. Thus, a median value of $\beta = 6$ was chosen for the current profile parameterization. Examples of current density profiles are illustrated in Fig. 4.19 for several values of α and show that the current profile becomes more peaked as the value of α decreases.

The well-known quantity of internal inductance ,l_i, that characterizes the width of the current profile in tokamaks is not as useful for hybrid stellarator devices since much of the confining poloidal field in the latter is provided by the current in the external coils. Indeed, because hybrid stellarators typically exhibit a larger vertical field index relative to tokamaks[61], the sensitivity of the requisite equilibrium vertical field to the poloidal β and internal inductance is lower than in a tokamak.

While the plasma pressure profile is not yet measured with precision in CTH, its overall effect on the equilibrium is low compared to that of the plasma current in these low β plasmas. The plasma density is measured with a three-chord interferometer[39], and measurements of central electron temperature are obtained with soft X-ray bremsstrahlung spectroscopy, with $T_{\mathrm{e0}} < 150\,\mathrm{eV}$. Chordal measurements of the soft X-ray emission using filters of different thickness also provide estimates of the electron temperature profile[37]. These measurements indicate profiles that are not strongly peaked. A Thomson scattering diagnostic now under construction[62] is expected to provide more accurate temperature measurements in the near future, and will serve to calibrate the soft X-ray profile measurements, thus giving a better measurement of the pressure profile. Until then, the fixed pressure profiles used in reconstructions are taken to have a broad radial profile parameterized as:

$$P(s) = P_0(1 - s^{10})^2\,, \tag{4.19}$$

with the central pressure P_0 estimated from the central density and temperature. Because the pressure of CTH ohmic plasmas is low, with typical values of the poloidal beta, $\beta_\theta < 0.1\%$, the effect of the uncertainty in the plasma pressure on the reconstructed equilibrium is limited, although certainly not inconsequential.

4.4.2 Equilibrium reconstruction of CTH plasma with magnetic diagnostics only

The following example of equilibrium reconstruction considers a case for which the external coil currents were configured to produce a low vacuum transform, $\iota_{\mathrm{vac}}(a) \sim 0.04$, with the electron density held constant at $n_{\mathrm{e}} \sim 0.4 \times 10^{19}\mathrm{m}^{-3}$. The left side of Fig. 4.20 shows time evolution of the plasma current, loop voltage, and $\dot{B}_\theta$ signal from one of the poloidal magnetic field probes. The plasma current shows a series of hesitations or plateaus prior to $t = 1.65\,\mathrm{s}$ which are characteristic of many current driven plasma discharges in CTH as in tokamak discharges. At the times of these current hesitations, positive loop voltage spikes and increasing magnetic fluctuating signals are observed, which are usually indications of current redistribution (peaking) and enhanced MHD activities. The amplitude of the magnetic signal begins to

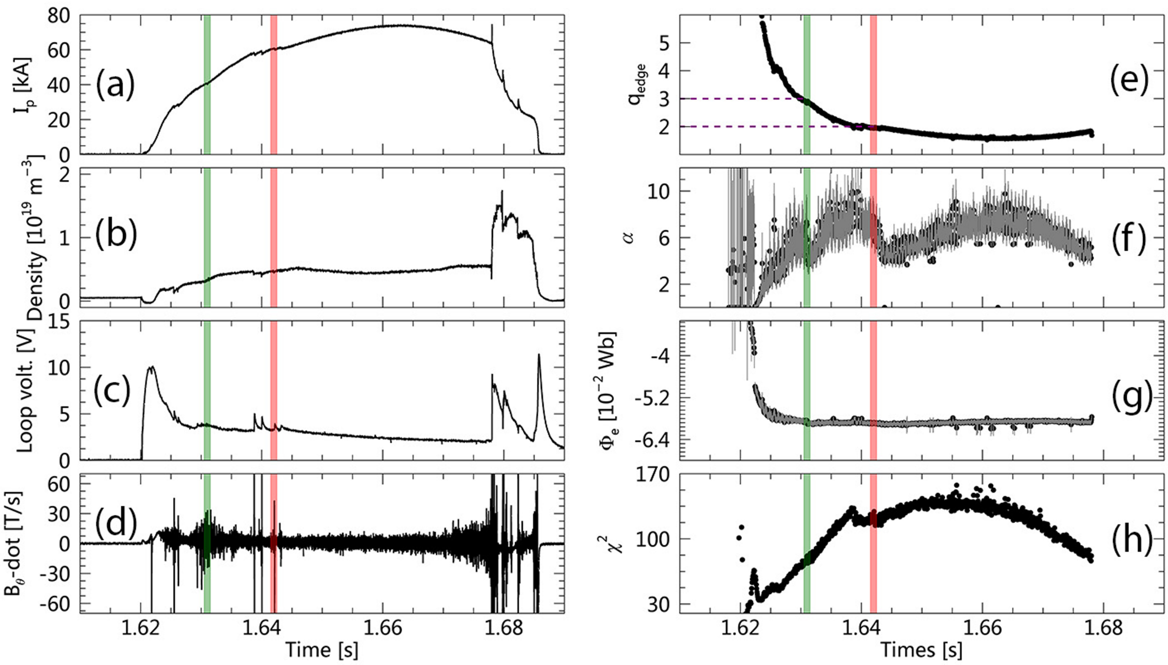

Figure 4.20: Left: (a) plasma current, (b) line-average density, (c) loop voltage, and (d) B_θ-dot signal from one of 32 poloidal magnetic pickup coils. Right: reconstructed parameters (e) edge safety factor $q_{\rm edge}$, (f) current density profile parameter α, (g) total enclosed toroidal flux $\Phi_{\rm e}$, (h) fitting error (χ^2). Colored regions highlight time intervals when current hesitations and increasing B_θ-dot signals are present.

grow around $t = 1.665\,$s until the plasma disrupts at $t = 1.678\,$s, marked by a drop in plasma current and a loop voltage spike.

A series of reconstructions were performed for the same discharge using the total enclosed toroidal flux, $\Phi_{\rm e}$, and the current density parameter α as reconstruction parameters. The results of these reconstructions are shown in the right side of Fig. 4.20 along with the evolution of edge safety factor value, $q_{\rm edge}$, and the χ^2 values from each reconstruction. Each hesitation seen during the plasma current ramp in Fig. 4.20(e) corresponds to the edge safety factor crossing a rational value, e.g. $q_{\rm edge} = 2, 3, 4$, as are highlighted by the blue, green, and red bars, which are indications of the presence of internal MHD modes[3].

Multiple sets of toroidal and poloidal magnetic pick up coil arrays are installed on CTH to measure MHD fluctuations[35]. The dominant mode structures resulting from a bi-orthogonal decomposition (BD)[63] technique of the measured magnetic signals at the times shown by green and red bars in Fig. 4.20 are shown in Fig. 4.21. These structures indicate the presence of

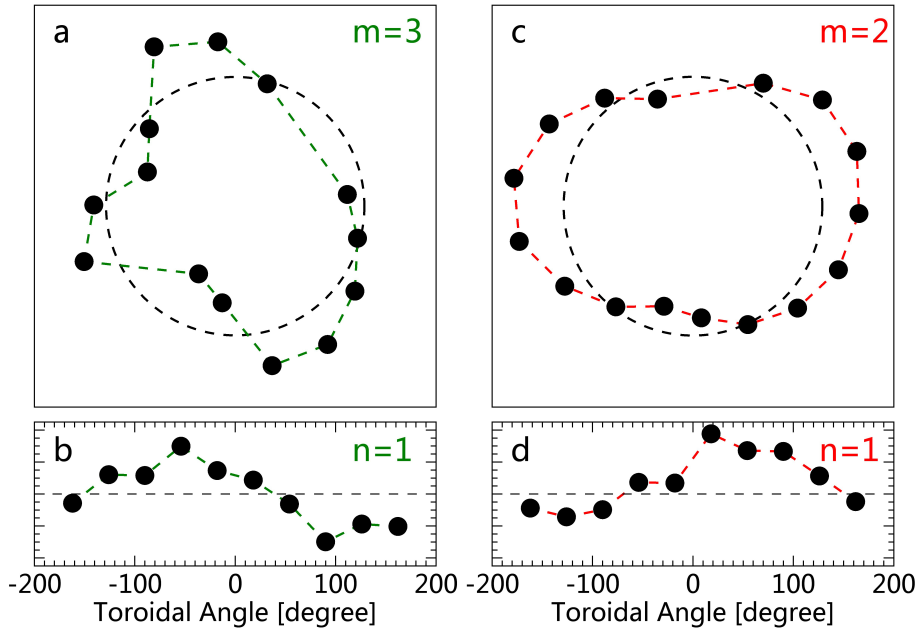

Figure 4.21: MHD fluctuation calculated by Bi-orthogonal decomposition (BD) of magnetic signals from poloidal and toroidal magnetic pick up coils. (a) and (b) shows resulting $3:1$ mode. (c) and (D) shows a $2:1$ mode.

$m/n = 3/1$ and $m/n = 2/1$ modes in agreement with the growing MHD activity measured from magnetic pick-up coils at these times.

The reconstructed parameter, α, specifies the peakedness of the current density profile. Its temporal trend shows it to suddenly decrease (corresponding to a radial narrowing of the current profile) as the edge safety factor crosses through integer values during the current rise prior to $t = 1.65\,\mathrm{s}$. Similar narrowing behavior observed during the current rise in tokamaks associated with resonant MHD activity may be more variable with regard to the value of q_{edge} due to the evolution of the internal current profile[64], while the non-disruptive current narrowing on CTH during the current rise may be more related to the plasma edge effectively being defined by a static magnetic island when $\iota\!\!\!$-(a) takes on low order rational values, leading to rapid transport at the edge.

The second reconstructed parameter, Φ_{e}, is the toroidal flux enclosed by the last closed flux surface. It is constrained in part by the locations of the physical limiters inside the CTH vacuum vessel. The trace in Fig. 4.20(h) is the standard reconstruction error, χ^2,. The reconstruction

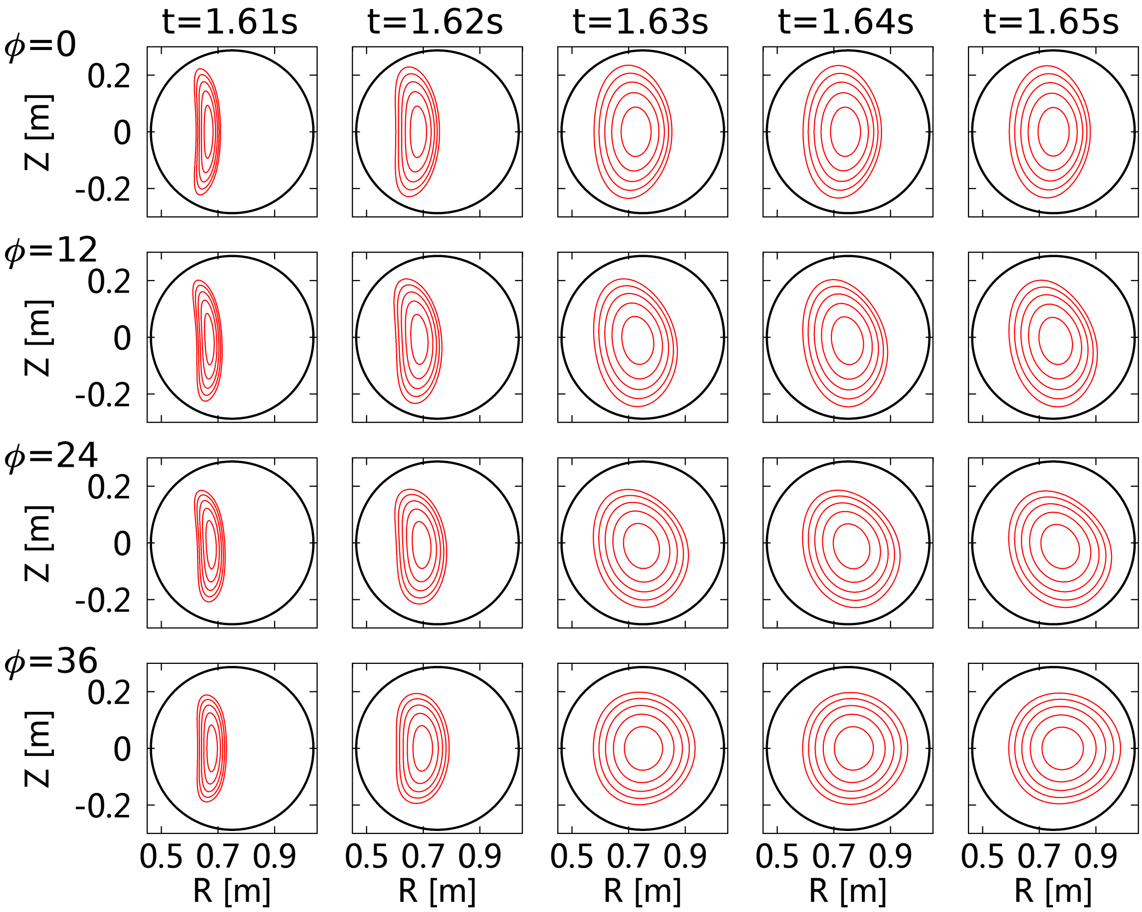

Figure 4.22: The poloidal cross-sections of flux surfaces at the toroidal angles,$\phi = 0°$, $12°$,$24°$ and $36°$, when $t = 1.61s$,$t = 1.62s$,$t = 1.63s$,$t = 1.4s$ and $t = 1.65s$.

error follows the trend of plasma current. Most likely this is because there are significant residual signals due to the eddy currents driven by the plasma current that are not well compensated. That speaks to the need for more accurate modeling of eddy currents especially from the helical coil frame.

These equilibrium reconstructions also provide shaping evolution of our hybrid plasmas. The poloidal cross-sections of flux surfaces at four different toroidal angles for different time slices are shown in Fig. 4.22. When the plasma current increases, the shape of the plasma at $\phi = 36°$ or the half period of CTH changes to a greater extent compared to the plasma at $\phi = 0°$ or the full period of CTH. The geometry of the plasma at the full period appears to be more rigid under the influence of the plasma current. To quantify the change of the geometry of the plasma, the time evolution of the major radius and the ellipticity of the plasma at both

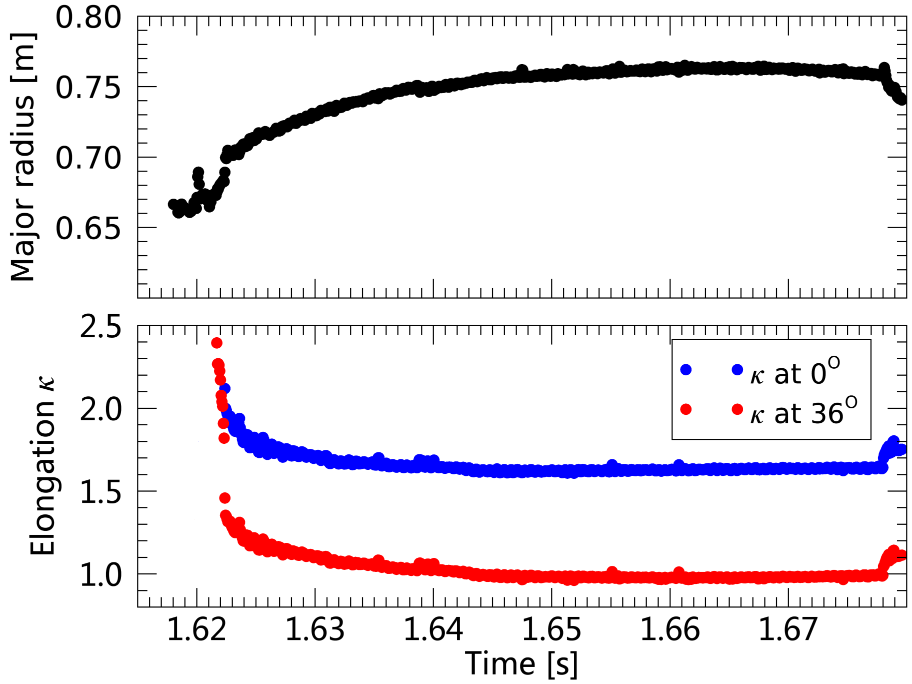

Figure 4.23: Time evolution of the major radius and the ellipticity of the plasma at $\phi = 0°$ and $36°$.

$\phi = 0°$ and $\phi = 36°$ are plotted in Fig. 4.23. With addition of plasma current, the plasma moves outward due to the change of toroidal force balance. The plasma also becomes more circular, or more like a tokamak. The change of the ellipticity of the plasma at $\phi = 36°$ is more dramatic compared to the plasma at $\phi = 0°$. This is due to the nature of helical coil winding. At the half period of CTH, the helical coils are wound above and under the plasma and produce helical fields to deform the plasma to be more circular. While the winding direction of the helical coils is at the horizontal mid-plane at the full period of CTH, where the helical fields cause less deformation of the plasma.

Operation with different external current configurations, allows CTH to vary the vacuum rotational transform $\iota_{\rm vac}$, which is an indication of amount of 3D field applied. An ensemble of plasma shots with low density ($\sim 0.6 \times 10^{19}\mathrm{m}^{-3}$) and varying $\iota_{\rm vac}(0.02 \rightarrow 0.14)$ are reconstructed at the time when the plasma current reaches maximum value. The scatter plot of the toroidal averaged elongation, κ, are show in Fig. 4.24 Plasmas are more elongated with increasing $\iota_{\rm vac}$, i.e. increasing amount of 3D stellarator field.

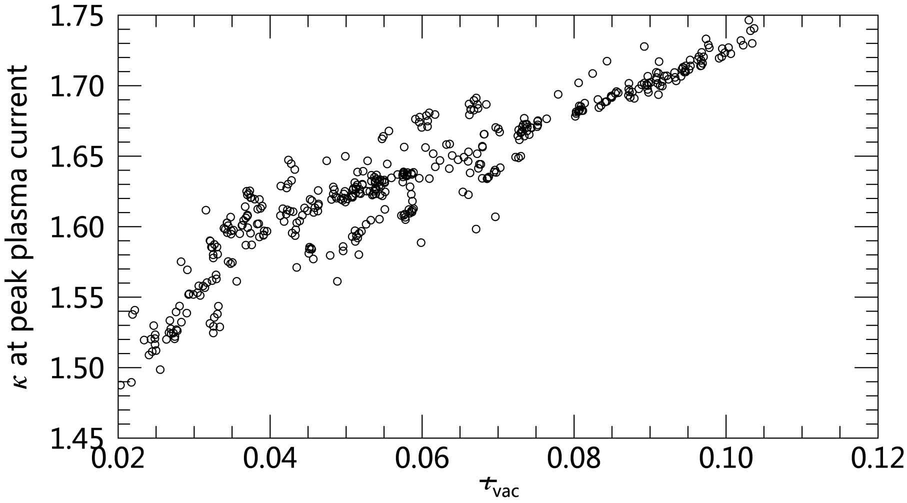

Figure 4.24: Scatter plot of κ vs. vacuum transform

4.5 Discussion

Equilibrium reconstructions with external magnetics have been useful to provide good estimates of edge or last closed flux surface properties of the plasma, including plasma position, shape, and edge rotational transform. However, it is well known that external magnetic diagnostics in axisymmetric plasmas have limited sensitivity to variation of internal current distribution, and yield only global current and pressure profile parameters such as poloidal plasma beta ,β_p, and internal plasma inductance, l_i[57,65–67]. Even in stellarator plasmas with typical geometries characterized by high elongation and non-axisymmetric 3D shaping, the variation of the magnetic field outside the plasma is predicted to yield little on the details of the internal current profile[68]. This fact will become clear when we perform equilibrium reconstruction of sawtoothing plasmas observed in CTH.

In tokamaks, sawtooth activity appears as a relaxation of the temperature in the center of plasma and is associated with the final state of a growing $m = 1$, $n = 1$ MHD fluctuation. Characteristic sawtooth relaxation can also been observed with sufficiently dense plasma in CTH and exhibit behavior similar to that of axisymmetric tokamaks. Under the assumption that the radius of the inversion of the sawtooth signals corresponds to the magnetic surface at which $q = 1$ as in tokamaks, the presence of a $q = 1$ surface near the core is expected for sawtoothing plasma in CTH also.

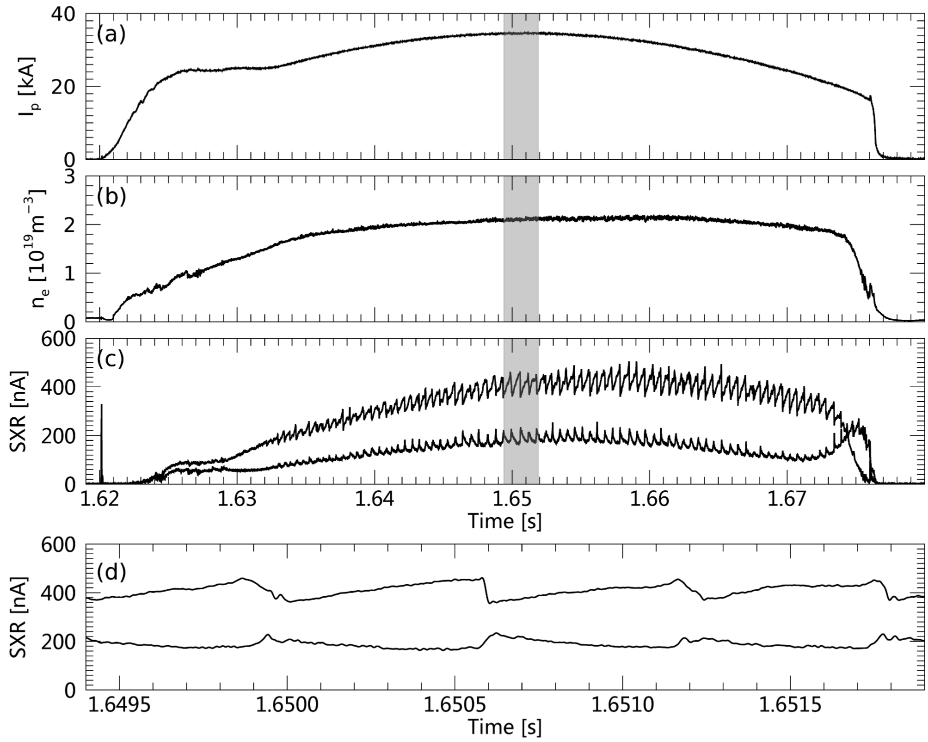

Figure 4.25: Signals from an example sawtoothing plasma. (a) plasma current, (b) electron density, (c) two SXR signals from the central camera of the two-color SXR system, (d) expanded view of (c) over time span of the gray bar.

An example of sawtoothing plasma with time trace of plasma current, density and two SXR signals from the central SXR camera is shown in Fig. 4.25. This plasma has a peak plasma current of $I_\mathrm{p} = 35\,\mathrm{kA}$ and an electron density of $\overline{n}_\mathrm{e} \sim 2.0 \times 10^{19}\,\mathrm{m}^{-3}$. The higher signal is from a channel viewing the plasma core, while the lower signal is from a channel viewing the plasma near the edge. The sawtooth signal in the core and inverted sawtooth signal near the edge are clearly seen in Fig. 4.25(d), which shows the SXR signals expanded at the time highlighted by the gray box in Fig. 4.25(c). The $q = 1$ surface must be between the two flux surfaces defined by the tangency radii of the two channels.

An equilibrium reconstruction has been performed at $t = 1.651\,\mathrm{s}$ at which time sawteeth are observed. The reconstructed current and safety factor profiles with uncertainties are shown in Fig. 4.26. In this reconstruction, the central safety factor is found to be $q \approx 2$, which is inconsistent with the well accepted premise that the central safety factor of sawtoothing discharges should be $q \approx 1$. Also, the large fitting uncertainties present in both the current profile and central q values highlight the limitation of using external magnetics to determine the

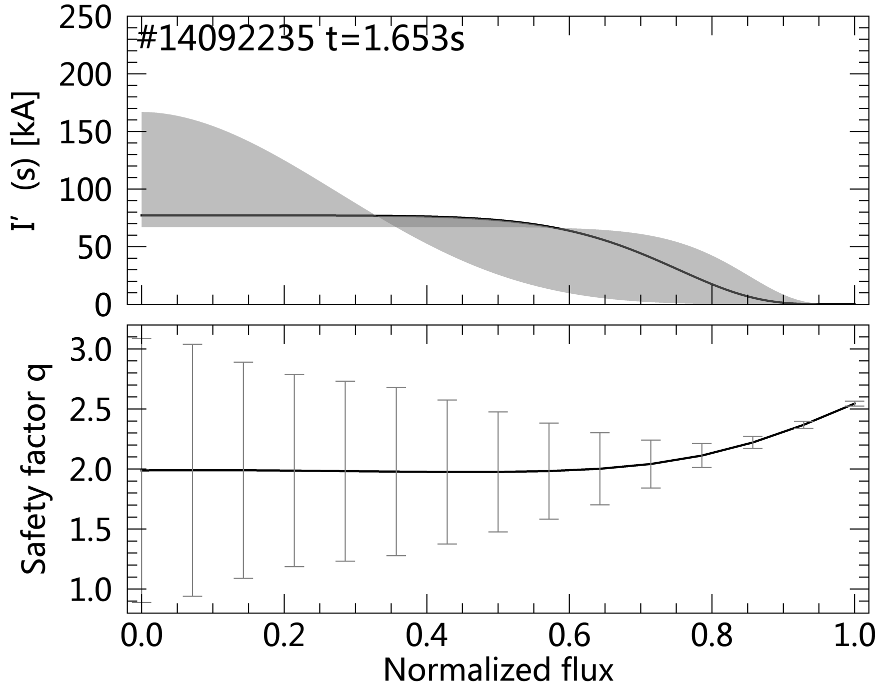

Figure 4.26: Reconstructed current and safety factor q profile at $t = 1.653\,\mathrm{s}$ when sawteeth are observed. The gray shadow marks the uncertainty in the current profile from reconstruction. The q profile is plotted with gray error bars.

current distribution in the plasma core. The unsymmetrical limits in the fitted current profile is an artifact of the two power model, in which the physical breadth of the profile increases nonlinearly as the value of α increases.

This result indicates that, accurate reconstructions of current and transform profiles, even in stellarator hybrids, require internal measurements of plasma parameters. And this has been achieved by including internal measurements from soft X-ray (SXR) emissions. Details of including SXR measurements in equilibrium reconstruction are described in the fellowing chapter.

Chapter 5

Improved equilibrium reconstructions with SXR measurements

5.1 Introduction

Knowledge of the internal plasma current and rotational transform profiles is required for an understanding of magnetohydrodynamic (MHD) stability of toroidal plasma and reliable operation of toroidal confinement devices. However, as demonstrated in Ch. 4, the experimental determination of the plasma current profile from external magnetics alone is inaccurate, and fails for sawtoothing plasmas. The resulting current profiles are much more broader than expected, and the reconstructed central safety factors are away from one. These results contradict the well accepted sawtooth theory, in which the sawtooth oscillation is driven by ohmic heating of the core plasma until the safety factor drops below one triggering the growth of an $m = n = 1$ kink-tearing mode. Additional internal measurements are required for better knowledge of the plasma current distribution, especially near the core of the plasma.

As in tokamaks, the plasma current profile and thus the q profile in a stellarator discharge could be determined from measurements of the internal poloidal magnetic field from motional Stark effect(MSE)[69–71] or Faraday rotation[72–74]. These diagnostics of course require a substantial investment of time and money, and often require specialized conditions. For example, MSE requires a neutral beam and toroidal field typically $2\,\mathrm{T}$ or greater, which is restrictive for small devices with low toroidal fields. As a result, it is of interest to develop and test alternative means of diagnosing the current profile suitable for smaller, lower-field experiments.

Currently in CTH, there is no direct method to determine the internal magnetic field distribution in plasmas from vector magnetic field measurements. Instead, we have used measurements from multiple SXR cameras in conjunction with external magnetic diagnostic data to reconstruct the current profiles from the equilibrium solution from the V3FIT code. We demonstrate that improved knowledge of the internal current distribution compared to using magnetic diagnostics only. Two implementations have been developed to incorporate SXR measurements in the V3FIT code. In the first approach, a single SXR camera array, at the mid plane of the vacuum vessel, is used to characterize the inversion radius of a sawtoothing plasma and locate the position of the $q = 1$ surface. Then the plasma equilibrium is reconstructed again using the extracted constraint of the location of the $q = 1$ surface along with magnetic diagnostic measurements. The second application is more straightforward, in which all SXR emissivity measurements are incorporated in the V3FIT fitting process to reconstruct the shape of magnetic flux surfaces and infer the internal current distribution. In both cases, we have obtained improved knowledge of the internal plasma current profile.

This chapter is organized as follows: the SXR camera system are described in Sec. 5.2. Sec. 5.3 and Sec. 5.4 describe in detail how we incorporate information of sawtooth inversion and SXR emissivity data in V3FIT to better fit the current profile in both cases. The results of reconstruction of an ensemble of sawtoothing plasma are also presented. Signal sensitivity of SXR cameras as well as validation of the implementation are discussed in Sec. 5.6

5.2 Soft X-ray camera system on CTH

Ten pinhole-type SXR/bolometer cameras have been installed on CTH at different toroidal and poloidal locations. All of them utilize photo-diode arrays with twenty detection elements each, separated by a distance of $0.114\,\mathrm{mm}$, giving a total of 200 channels. A $1\,\mathrm{mm}$-wide slit acts as a collimator such that only the radiation from one line-of-sight is incident on a particular photo-diode. The photo-diode array is located $3\,\mathrm{cm}$ behind the slits, though the separation between the slits and the the diode array is adjustable to provide wider or narrower fields of view depending on the application or location of the camera. Filters with different materials and thicknesses are placed in front of the detection diodes to block low energy photons. The SXR camera suite

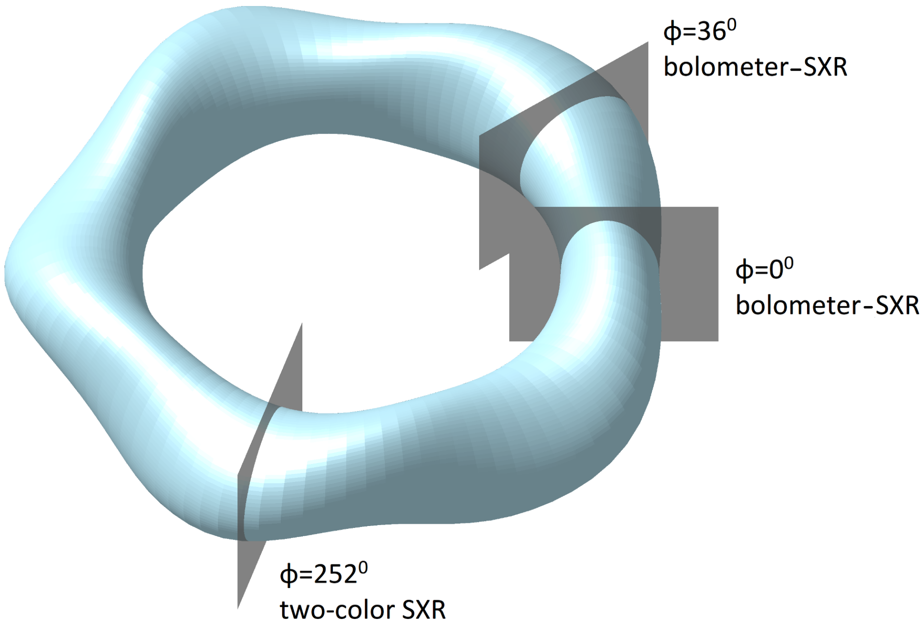

Figure 5.1: A rendering of the last closed flux surface of a CTH plasma with poloidal cross-sections (highlighted in grey) showing the toroidal angles where SXR cameras are installed, and used for 3D equilibrium reconstructions.

on CTH consists of three two-color cameras[37] and two bolometer-SXR systems[38]. Fig. 5.1 is a rendering of the last closed flux surface of a CTH plasma with poloidal cross-sections highlighted in grey, indicating the three toroidal locations where the SXR cameras are installed.

A two-color SXR camera system is mounted in a toroidal symmetry plane at $\phi = 252°$. It consists of three sets of two-color SXR cameras, with one set viewing from the outer mid-plane and another two sets at $60°$ above and below the mid-plane. At each poloidal location, two parallel 20-channel diode arrays view the plasma through collimators and compound filters with a $0.5\,\mu\mathrm{m}$ carbon layer and either a $1.0\,\mu\mathrm{m}$ or $3.0\,\mu\mathrm{m}$ aluminum layer. Fig. 5.2 shows the lines-of-sight of the three cameras with respect to the last closed flux surface of a typical plasma equilibrium and the position of the CTH vacuum vessel. Since CTH is highly non-axisymmetric, the shape of the plasma at different field-periods of the device is significantly different. It is desirable to have soft x-ray measurements not only at different poloidal locations but also at different toroidal locations. The bolometer-SXR camera shares a similar design as the two-color cameras but one of the photo-diode arrays has no light filter thus acting as a bolometer, while the other photo-diode array does view the plasma through a filter. One

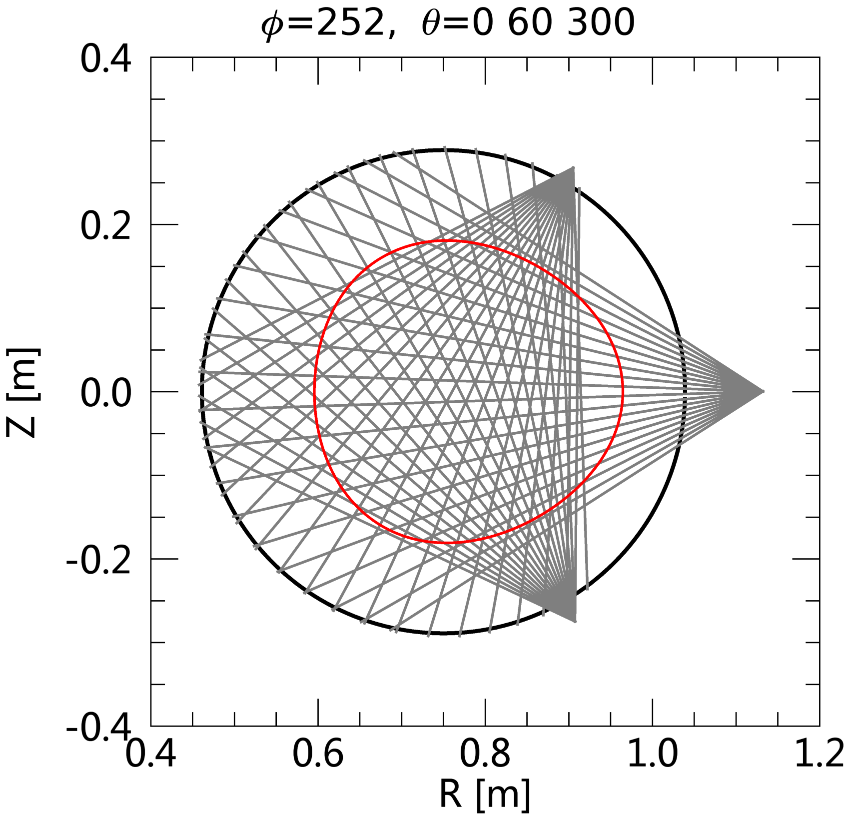

Figure 5.2: Position and chords view of the two-color SXR cameras at $\phi = 252°$. The last closed flux surface of a typical plasma is shown in red. The CTH vacuum vessel is represented by a black circle.

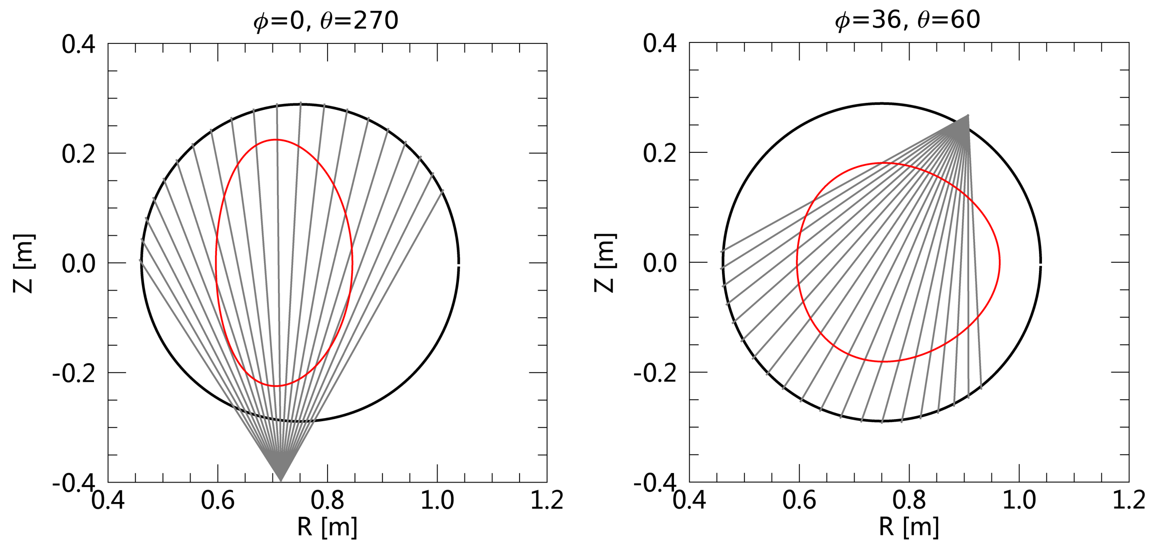

Figure 5.3: Position and chords view of two SXR-bolometer cameras at $\phi = 0°$ and $\phi = 36°$.

bolometer-SXR diode array, is installed at $\phi = 0°$ and $\theta = 270°$ to have a vertical view of the plasma in its most elongated cross-section, and uses the same thin aluminum/carbon filters as in the two-color system. An additional camera, is mounted at $\phi = 36°$ and $\theta = 60°$. Beryllium filters with thickness of $1.8\,\mu\mathrm{m}$ are used for the SXR camera. Their chordal sight lines are shown in Figs. 5.3.

5.3 Use of sawtooth inversion for current profile determination

In current-driven discharges that are sufficiently dense (nominally above $1.5 \times 10^{19}\,\mathrm{m}^{-3}$), the soft X-ray emission often exhibits characteristic sawtooth oscillations with an inversion of the phase of the sawtooth evident in the radial profile of the emission. Under the assumption that the radius of the inversion of the sawtooth signals corresponds to the magnetic surface at which $q = 1$, as in tokamaks, the values of the parameters used to fit the plasma current profile can be known with far greater precision than with magnetics alone. In V3FIT, this is performed as a secondary optimization step in which the inversion radius is identified with a flux surface found from the reconstruction performed with magnetics alone, and the current profile is then reconstructed again with the prior knowledge of $q = 1$ corresponding to a particular reconstructed flux surface. The details of this implementation are described below by taking the sawtoothing discharge at the end of Ch. 4 as an example.

To quantify the inversion radius of the sawtoothing, a singular value decomposition (SVD) is performed with the 20 chordal signals from the central camera in the two-color SXR system. The central camera is chosen for the calculation due to the vertical symmetry of the magnetic flux surfaces at $\phi = 252°$. SVD separates a spatio-temporal signal into orthogonal temporal modes and orthogonal spatial modes[75]. Each spatial mode corresponds to a unique temporal mode so that coherent structures and their associated phenomena can be identified. If a SXR signal is described as a function, $f(x,t)$, it can be expanded as a combination of spatial components, $v_n(x)$, and temporal components, $u_n(t)$, as shown in Eq. 5.1[76].

$$f(x,t) = \sum W_n v_n(x) u_n(t) \tag{5.1}$$

The spatial and temporal components $v_n(x)$ and $u_n(t)$ have the property:

$$\begin{aligned} v_i(x) \cdot v_j(x) &= \delta_{ij} \\ u_i(t) \cdot u_j(t) &= \delta_{ij} \,. \end{aligned} \tag{5.2}$$

Here δ_{ij} is the Kronecker delta function. The weight, W_n, is a measure of the total contribution of each spatial and temporal function relative to the overall signal. The modes that are associated with larger value of W_n are better correlated in time while random patterns in the signals will have smaller W_n[77]. As a result, SVD allows real physical phenomena to be discovered by filtering uncorrelated noise within the data.

To perform SVD on multiple SXR signals, a matrix consisting of 20 SXR chordal measurements, $\mathbf{F}_{ij} = f(x_i, t_j)$, is constructed with $f(x_i, t_j)$ representing the signal from specific channels. From Eq. 5.1, $\mathbf{F}_{ij}$ can be expanded as:

$$\mathbf{F}_{ij} = \mathbf{VWU}^* \,, \tag{5.3}$$

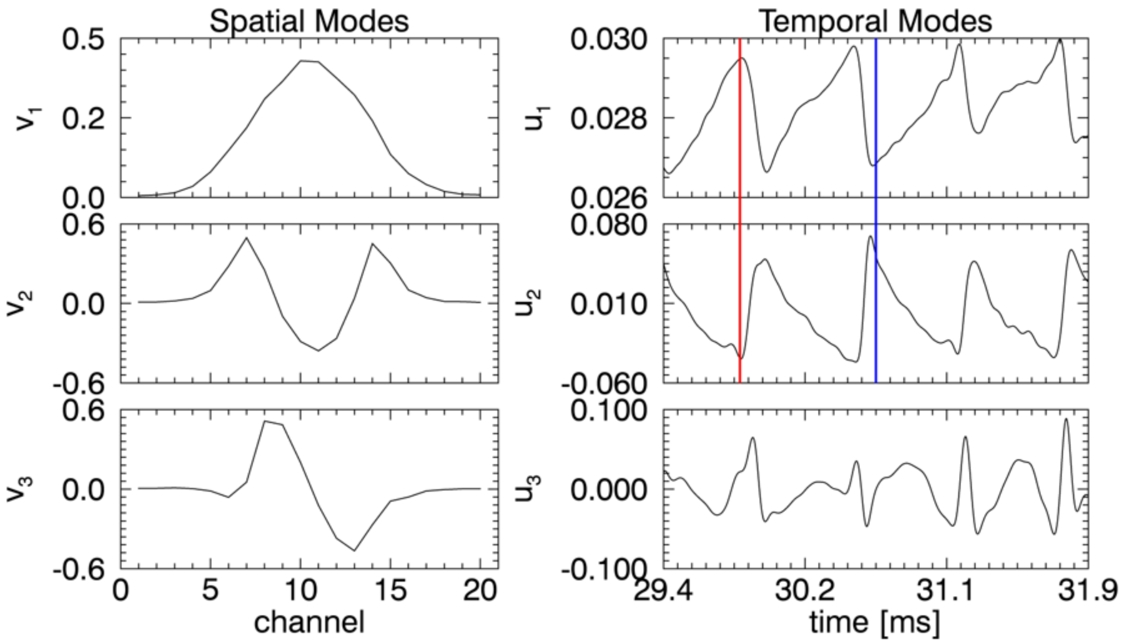

Figure 5.4: SVD analysis of a sawtoothing plasma segment in CTH (Shot:16033023, time window: $1.6494\,\mathrm{s}$ to $1.6519\,\mathrm{s}$). The largest three spatial modes are plotted on the left. The corresponding temporal modes are plotted on the right.

where $\mathbf{V} = [v_1(x), v_2(x), ...]$ and $\mathbf{U} = [u_1(t), u_2(t), ...]$ are vectors of spacial and temporal modes respectively, and $\mathbf{U}^*$ is the complex conjugate of the temporal mode vector.

The SVD analysis of the sawtoothing plasma (Shot:16033023) presented at the end of Ch.4 is shown in Fig. 5.4. The figure shows the analysis for the time segment between $1.6494\,\mathrm{s}$ and $1.6519\,\mathrm{s}$. The largest three spatial and temporal modes are plotted on the left and right respectively with subscripts referring to the mode number. The first spatial and temporal modes have the largest weight $W_1 = 373$, and demonstrate the time evolution of the sawtooth rise and crash. The second spatial profile, v_2, changes sign at channels 8 and 13, relative to the central channels. The sawtooth behavior in the second temporal mode is inverted relative to that of the first temporal channel. The inversion radius can be interpolated from the second spatial mode, i.e. where the second spatial mode crosses zero. The third spatial mode shows the $m = 1$ oscillation that is correlated with the sawtooth instability.

The location of the phase inversion of the sawtooth oscillations may be identified using a sum of the first two dominant spatial and temporal modes obtained by SVD. Fig. 5.5 shows a

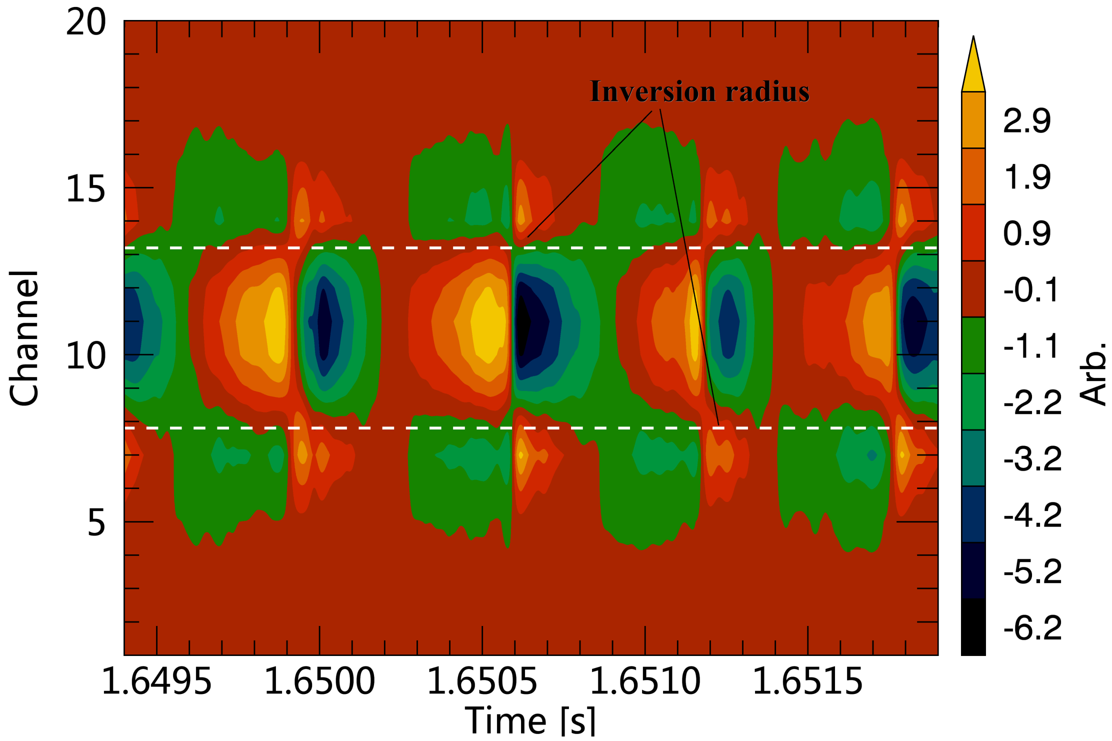

Figure 5.5: Contour plot of reconstructed SXR signals using the two dominant spatial and temporal modes obtained by SVD. The channel number of the SXR chords is plotted on the y-axis, and time on x-axis. The inversion radius is marked on the plot by white dashed lines.

contour plot of reconstructed SXR signals. To emphasize the sawtooth oscillation, the background equilibrium signal has been subtracted from each channel to suppress the SXR emission increase during the time duration of the figure. The contour plot shows several sawtooth cycles. The SXR emission of the core increases until the sawtooth crash, expelling thermal energy from the core region inside the inversion radius, and increasing the signal level from the SXR diagnostic channels outside the inversion radius. Using SVD, the inversion radii of the sawtooth are identifiable, and effectively correspond to channels 7.8 and 13.2, i.e. around channels 8 and 13.

The next step is to project the SXR sight lines associated with the inversion surface onto the flux surfaces calculated from an equilibrium reconstruction using external magnetics. The surface on which $q = 1$ is taken to be the reconstructed surface that is tangent to the sight lines identified with the sawtooth inversion radii. Here reconstruction is performed with a resolution of 30 surfaces in the normalized flux variable. As shown in Fig. 5.6, the inversion occurs near the second flux surface for this plasma.

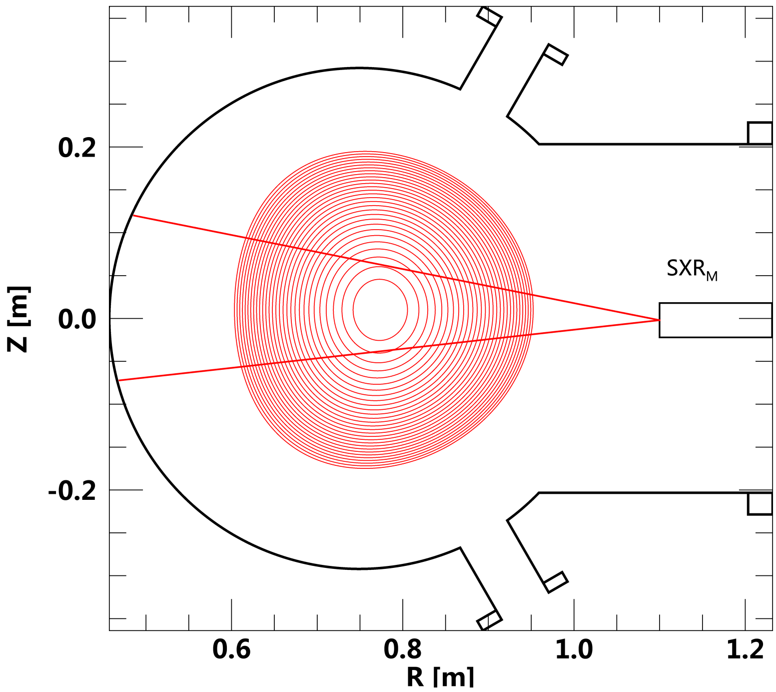

Figure 5.6: SXR viewing chords identified with the sawtooth inversion mapped onto the reconstructed flux surfaces.

We then set q to be $1 \pm \delta$ at a specific value of s (here at $s = 2/29$). Because the resolution is limited by the number of SXR camera channels (20) and flux surfaces (30), an uncertainty δ of 0.02 is chosen, so that q value can be allowed to vary by a finite amount at $s = 2/29$. This so-called prior setting, while not treated as an independent signal in V3FIT, nonetheless acts as an internal diagnostic, and therefore contributes to the overall value of χ^2 from the reconstruction fitting.

The reconstructed current and safety factor profiles making use of the prior knowledge of the position of the $q = 1$ surface are plotted in red in Figs. 5.7(a) and (b), and are significantly different from the results of the reconstruction using external magnetics alone. Inclusion of the information of the inversion surface in the reconstruction results in a substantially more peaked current profile with the reconstructed α value changed from 7.5 ± 4.6 to 1.7 ± 0.14, thus decreasing the fitted central q towards unity, consistent with the sawtoothing nature of the discharge. The fitted profiles shown in Figs. 5.7(a) and (b) exhibit lower uncertainties than in the previous case, demonstrating the effectiveness of the prior constraint in changing the shape

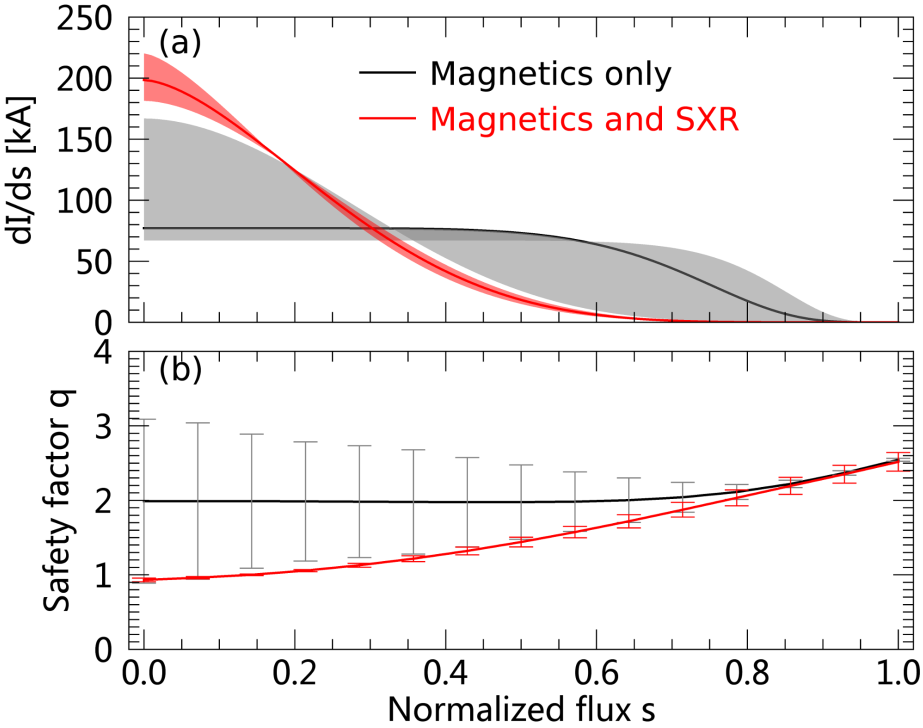

Figure 5.7: A comparison between reconstructed current and safety factor profiles from reconstructions done with magnetic data only and with the prior constraint of the location of the $q = 1$ surface. The reconstruction with magnetics only are shown in gray, and the reconstruction that utilized both magnetics and SXR signals is shown in red.

of the current profile by channeling more plasma current into the discharge center. With the inclusion of the SXR inversion analysis, the χ^2 is also reduced from 46.3 with magnetics alone to 35.9, indicating a better overall fit.

A subset of the reconstructed flux surfaces with and without the prior constraint of inversion radii are shown in Fig. 5.8. Since the reconstruction using the inversion information

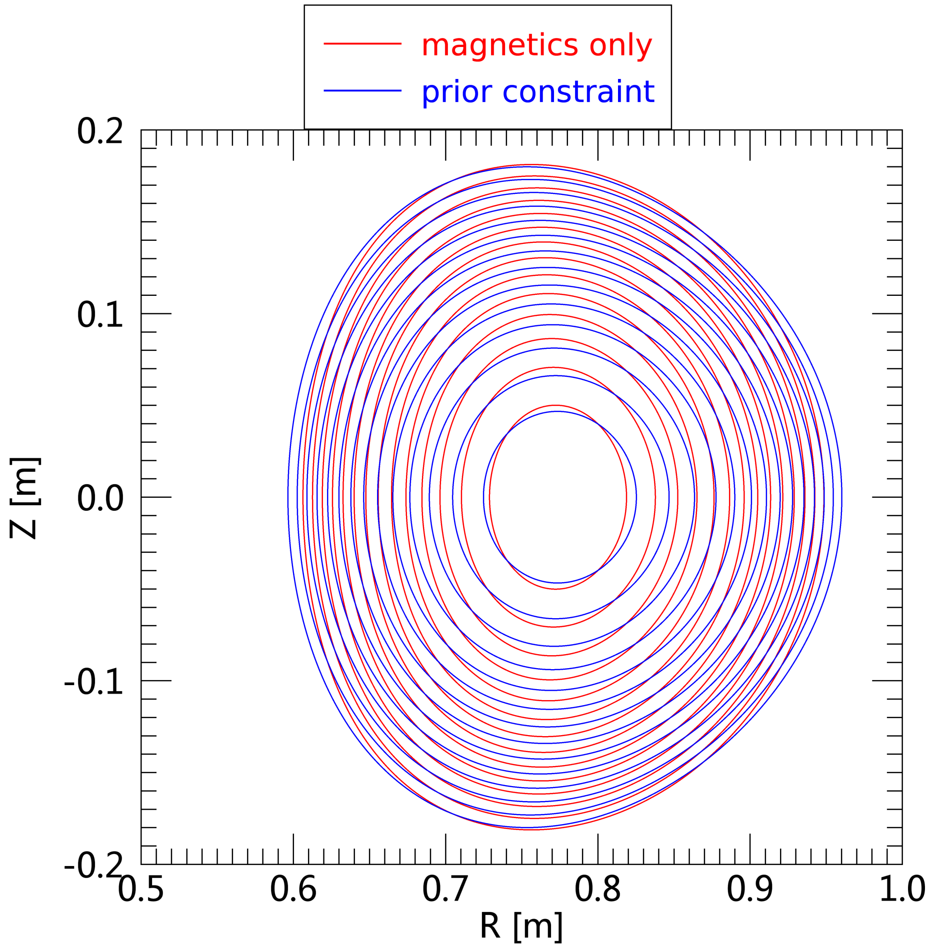

Figure 5.8: Comparison of reconstructed magnetic flux surfaces with and without the prior constraint.

channels more current into the core of the plasma, the flux surfaces near the center become more circular . Because the resolution of flux surfaces in the center of the plasma is lower than in the edge, and the resolution of the chords of SXR cameras is also limited, the index of the $q = 1$ surface does not change.

To check the influence of plasma pressure on reconstructions, we perform a series of reconstructions assuming electron temperatures of 0, 50, 100, 150 and $200\,\mathrm{eV}$. The approximate

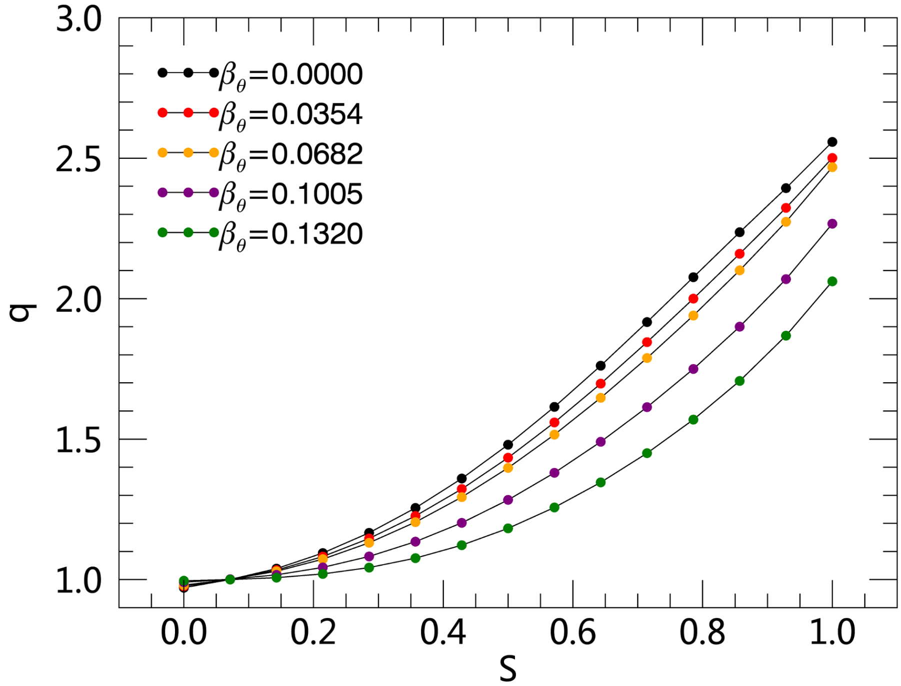

Figure 5.9: Resulting q-profiles as the pressure is scanned show the pressure has a limited effect on the reconstructed q-profile for a low-beta plasma configuration. Note that the quoted values of β_θ are in terms of percent.

central electron temperature is around $100\,\mathrm{eV}$ according to two-color SXR measurements. The resulting q-profiles from this set of reconstructions are shown in Fig. 5.9. Under low poloidal β, we obtain similar q-profile while the edge q diverges considerably with increasing β_θ.

The corresponding reconstructed current profile parameter α and final χ^2 are listed in Table. 5.1. As in tokamaks, we expect the Shafranov shift to depend nearly linearly on the

β_θ	0	0.035	0.068	0.100	0.132
α	1.6	1.7	1.7	2.0	2.4
χ^2	30.6	32.8	34.5	87.1	121.0

Table 5.1: Reconstructions with assumptions of different values of the pressure variable β_θ

parameter $\beta_\theta + l_i/2$. If the pressure is taken to be larger, then the fitting procedure would naturally lower the fitted value of $l_i/2$, or more specifically the peakedness of the plasma current profile. Larger β_θ thus leads to the broadening of the current profile, but since we have set a strong constraint on the location of the $q = 1$ surface, the broader profiles result in poorer equilibrium fits in V3FIT, and correspondingly larger values of χ^2.

Prior knowledge of the location of the $q = 1$ surface involves a specific physical interpretation of sawtooth activity and is a strong constraint on the safety factor profile. It limits the variation in the value of the central safety factor q_0, while external magnetic diagnostics predict the edge safety factor q_{edge}. Therefore, the implementation of sawtooth inversion information in V3FIT has provided precise information of the current distribution near the core of the plasma, acting like a single-point 'MSE-like' diagnostic. However, this procedure has several disadvantages. The biggest limitation is that this implementation is only usable for discharges with identifiable sawteeth in the x-ray emission, since the method is based on sawtooth inversion calculation. There remains a lack of reliable diagnostics to directly determine the current profile in all CTH plasmas regardless of sawtooth activity or not. The method also introduces errors due to the limitation of physical resolution of the SXR camera system and computational resolution of equilibrium code near the magnetic axis. It should also be pointed out that the application of this particular constraint on the location of the $q = 1$ surface is also not straightforward in the V3FIT fitting procedure. The inversion surface must first be identified before its location can be used as a prior constraint as discussed above. Furthermore, the prior method only uses SXR emissivity measurements from one diode array out of the eight available on the CTH system. Given the availability of the other internal SXR measurements, it is desirable to develop a more straightforward way to incorporate all SXR measurements in V3FIT, and reconstruct current profiles for either sawtoothing or non-sawtoothing discharges. This has been accomplished by reconstructing the shape of magnetic flux surfaces and thus inferring the plasma current distribution using diagnostic measurements from all SXR diode arrays, considered as flux surface functions in V3FIT.

5.4 Implementation of SXR emissivity measurements in V3FIT

5.4.1 Using flux surface geometry to determine the current distribution

The Shafranov shift, which describes the displacement of the centers of the magnetic flux surfaces with respect to the center of the bounding surface, nearly linearly depends on the parameter $\beta_\theta + l_i/2$. Thus changes of the geometry of magnetic flux surfaces will affect the value of the internal inductance, l_i, i.e. the current distribution within the plasma. Christiansen and Taylor demonstrated that the current distribution in an axisymmetric discharge with non-circular cross-section, in principle, can be completely determined from purely geometric information about the shape of the magnetic flux surfaces[78]. It was proved that if the magnetic flux surfaces were represented by a certain constant function $F(R, Z)$, then the current distribution could be a function $\lambda(F)$, which was determined from the gradient and Laplacian of F on each surface. Because the function $\lambda(F)$ depends on the change in $\nabla(F)$ on the flux surface, this calculation fails in the limit of large aspect-ratio and circular flux surfaces, but works well in highly non-circular plasmas. If the plasma temperature, density and impurity concentration may be assumed to be constant on a flux surface, the SXR volume emissivity should also be constant on that flux surface. Hence surfaces of constant emissivity can be interpreted to be magnetic flux surfaces. The plasma current distribution can then be determined via tomographic inversions of x-ray intensities from crossed one-dimensional imaging cameras.

The theory was first experimental tested in JET, where tomographic inversion of soft x-ray intensity measurements were used to determine the geometric shift and ellipticity of the flux surfaces, and to infer the current distribution[79]. The results were checked with that from equilibrium reconstruction using external magnetic diagnostic measurements. The comparison showed good agreement within the region where $0.2 < r/a < 0.8$ of the plasma, but equilibrium reconstruction with magnetic measurements was not sensitive enough to determine the central safety factor q_0 to within 20%. However, sensitivity to noise, which is inherent in any direct inversion process, introduced significant uncertainty in the calculated q_0.

A forward modeling approach using tangential soft x-ray pinhole camera (SXR PHC) measurements was developed on the Princeton Beta Experiment (PBX) to avoid the disadvantages of the direct inversion process[80,81]. Instead of using a tomographic inversion, the measured two-dimensional (2D) tangential SXR image of the plasma was projected toroidally and compared against the results from an equilibrium reconstruction using external magnetic diagnostics. The value of q_0 was iteratively adjusted in the reconstruction until the projection of the equilibrium reconstruction and SXR image had the best match. Although this implementation involved a manual iterative feedback loop, it demonstrated that the application of flux surface geometry from SXR emission measurements coupled with external magnetic diagnostics could successfully determine the plasma current distribution from equilibrium reconstruction.

The Pegasus Toroidal Experiment (PEGASUS) also used the tangential SXR image as a constraint in the equilibrium reconstruction code, along with other external magnetic diagnostic measurements, to determine the plasma current and safety factor q profiles[82,83]. The implementation included several steps. First the SXR intensity on the horizontal mid-plane of the pinhole camera is Abel-inverted[84] to get an SXR emissivity profile across the mid-plane of the plasma cross section. The obtained SXR emissivity profile is then mapped to a flux surface profile generated from a reconstructed plasma equilibrium using external magnetic diagnostics. Based on this mapping, a SXR emissivity image is calculated over the entire cross section of the plasma. This emissivity image is then projected toroidally to create a SXR intensity image. The resulting SXR intensity image is checked against the original CCD image to calculate the associated χ^2, which quantifies how well the two images match to each other. The current profile is reconstructed using a least squares linear fitting routine in the equilibrium code.

The above applications of SXR emissivity measurements are all indirect in that they assume iso-emissivity of SXR on a flux surface, and make use of multiple-step algorithms. More recently, a comprehensive method to self-consistently reconstruct the equilibrium current profiles with magnetic and SXR data using the equilibrium fitting code EFIT[40,42] was developed on DIII-D[85]. In conjunction with external magnetic data, this method provides accurate current and q profiles in reasonable agreement with those obtained using the MSE diagnostic. In this thesis, we experimentally extend this approach in which geometry of the flux surfaces is used to determine the plasma current distribution to a fully three-dimensional nonaxisymmetric configuration. A method has been developed to reconstruct magnetic flux surfaces and current profiles using a combination of 160 SXR emissivity signals and 51 external magnetic signals in the 3D equilibrium reconstruction code, V3FIT.

5.4.2 Implementation of SXR emissivity measurements in V3FIT

The SXR chordal model used in V3FIT is a one-dimensional line integration through the center of the solid angle observed by a particular photo-diode detector. To utilize SXR emissivity measurements, both geometric information (geometric input) and experimental measurements (data input) of all SXR channels are required in V3FIT. The position and orientation of each SXR camera diode are measured with a Coordinate-Measuring Machine to a nominal accuracy of 0.25 mm with respect to the CTH magnet coil system. Based on those measurements, coordinates of all the chordal sight lines with respect to the magnetic geometry are calculated and formatted as geometric inputs to V3FIT. Due to the flat geometry of the diode array and the placement of the viewing slit in the center of the diode array, the angular extent of the poloidal view is different for each diode within each SXR camera. Because the edge channels are further away from the slit than the central channels, there results an effective decrease in the slit width. This so-called geometric factor is accounted for when comparing integrated emissivity measurements in V3FIT[38] and is included in the geometric input file.

The data input contains processed SXR measurements from all chords of the cameras. A dedicated IDL program has been developed to process the raw SXR signals after each plasma discharge, and save the results to a separate node in the MDSplus[86] data tree. First, SXR signals from the data acquisition system are deconvoluted to correct for phase shifts and account for the gains from electronic amplifiers. The signals are then passed through a digital Butterworth filter with a cutoff frequency of $10\,\mathrm{kHz}$ in order to eliminate high frequency noise and increase the signal to noise ratio. Lastly, signals are further smoothed by averaging over a time window of $1\,\mathrm{ms}$.

With the known geometry of SXR chordal sight lines, parametrized emissivity profiles are specified in flux geometry to calculate the simulated SXR emission from a given VMEC equilibrium. Because the SXR cameras record emission above a certain energy threshold that is filter dependent, each set of SXR diodes with filters of the same thickness is used to create a filter-specific line segment emissivity profile. The large number of chords available expands the number of parameterizations that can be used. Each line-segment emissivity profile consists of ten line segments, the height of each segment representing the emission intensity at a specific flux surface. Line segments of length 0.1 (in normalized flux units) are reconstructed from the axis at $s = 0$ to the plasma boundary at $s = 1$, where the emission intensity is set to be zero. For each emissivity profile, there are 10 reconstructed parameters.

Using specified emissivity profiles and plasma equilibrium provided by VMEC, modeled SXR signals are calculated using line integration. With processed experimental inputs and modeled responses calculated by V3FIT, the corresponding value of χ^2 is calculated. The emissivity profiles along with other plasma parameters are optimized/reconstructed iteratively within V3FIT until a minimum value of χ^2 is obtained.

In order to deconvolve the flux surface geometry from the SXR emission, we make the reasonable assumption that X-ray emissivity is taken to be constant on a magnetic flux surface in non-pathological discharges. However, experimental indications of X-ray emission not being constant in a flux surface have been reported in larger experiments[87,88]. For example, a discrepancy between the X-ray contours and magnetic flux surfaces has been observed in Alcator C-Mod tokamak plasmas with MARFEs, leading to the conclusion that X-ray emissivity is not always constant on a flux surface, particularly in plasmas evidencing local thermal instability. Nonetheless, we will make the assumption that at least within the plasma core, the iso-emissivity contours may be aligned with the magnetic flux surfaces. SXR emission is a function of electron temperature, density and impurity concentrations. Since electron thermal transport parallel to the magnetic field is strong, considering electron temperature to be a good flux quantity is a reasonable approximation. Also, because there is no symmetry or quasi-symmetry in the magnetic field other than the usual stellarator field-period symmetry, we expect flows to be significantly damped, and hence centrifugal effects that might lead to density not being a good flux surface function should be small. The assumption of impurity concentration as a flux function is the one most difficult to justify. Without further measurements to independently quantify this assumption, we simply assume it and investigate the ability to fit the profiles.

5.4.3 Reconstruction results

As a comparison, the same plasma in Sec. 5.3 is reconstructed again using the 160 SXR chordal measurements in V3FIT instead of using the sawtooth inversion location. Reconstructed parameters include the total enclosed toroidal flux, current density profile parameter α, and three emissivity profiles consisting of 30 parameters to be determined. The final fitting between experimental measurements and modeled signals derived from reconstructed equilibrium are shown in Fig. 5.10. Here experimental inputs are plotted in red with gray error bars, while

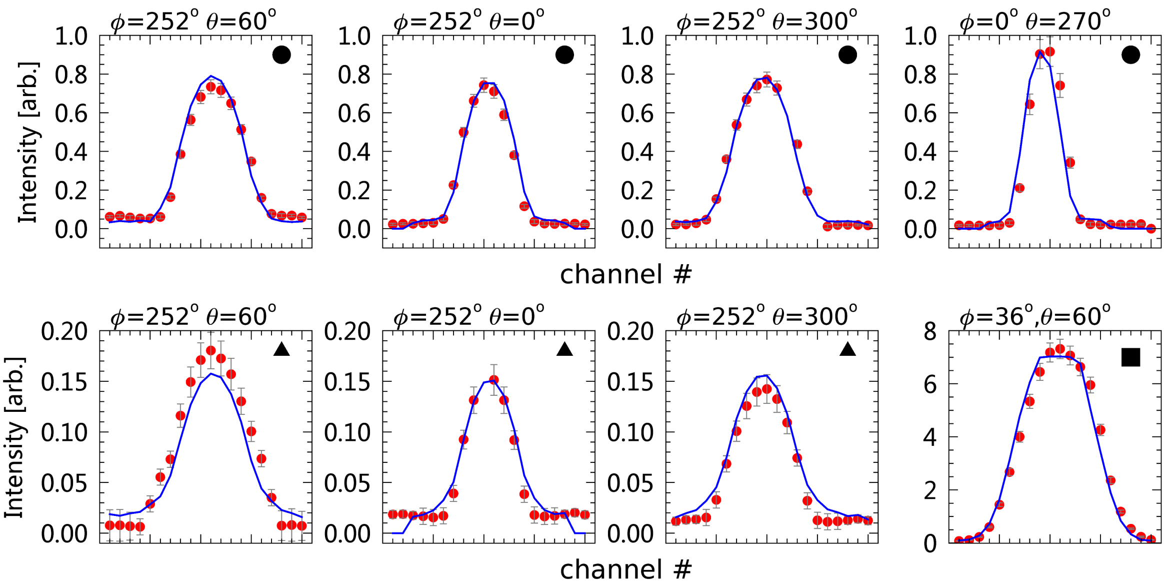

Figure 5.10: A comparison between experimental SXR measurements (red dots) and modeled signals (blue curve) derived from reconstructed equilibrium for select SXR cameras. The black symbols in the upper right portion of each graph (circles, triangles and square) are used to identify cameras with filters made of $1.8\,\mu\mathrm{m}$, $1.8\,\mu\mathrm{m}$ Aluminum-Carbon, $3\,\mu\mathrm{m}$ Aluminum-Carbon, and $1.8\,\mu\mathrm{m}$ Beryllium respectively. Cameras with similar filters only contribute to those individual emissivity profiles as experimental data.

the simulated signals are shown in blue. SXR cameras that use the same filters and the same emissivity profile are identified with similar markings in the upper right corner of the figures (circles, triangles, and a square). Here, three emissivity profiles are introduced. The two sets of signals match well for cameras in different poloidal and toroidal positions. The reasonable profile fit results support the assumption that SXR emissivity may be taken to be a constant on a flux surface for CTH plasmas.

The reconstruction result is checked against the one using the sawtooth inversion information discussed in Sec. 5.3. Fig. 5.11 presents a comparison of the resulting current and safety factor profiles in two cases. Both current and q profiles of the two cases match well with each other. It is important to note that the reconstruction directly using SXR data predicts the central safety factor q_0 to be close to unity even without applying the prior knowledge of the inversion radius. This provides some support of the model despite the uncertainty of the assumption of

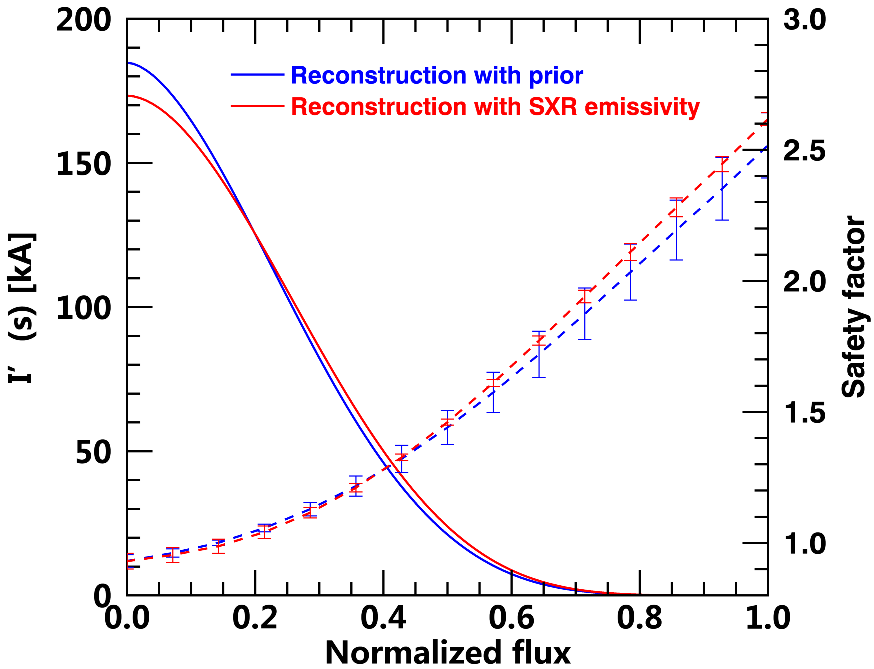

Figure 5.11: Comparison of the reconstructed current density and safety factor profiles from two cases of reconstructions. The results from reconstruction directly using SXR emissivity measurements are shown in red, while the ones from reconstruction using the prior constraint of the inversion radius are shown in blue.

iso-emissivity contours corresponding to magnetic flux surfaces. Provided no physical interpretation of the sawtooth, V3FIT is still able to channel sufficient current in the core of the plasma to drop the central q_0 around one by reconstructing the emissivity profiles and the geometry of magnetic flux surfaces.

A quantitative measure of the effectiveness of the diagnostic in determining current density profile is given by the so-called signal effectiveness calculated in V3FIT[21]. The detailed definition of the signal effectiveness is given in Appendix, C. It is a dimensionless, normalized ratio of the fractional reduction in the reconstructed parameter variance to the fractional reduction in the signal variance. It essentially tells how effective one particular diagnostic is in determining one specific plasma parameter. To test the sensitivity of different diagnostics to the change of current profile, a set of 140 discharges with different plasma parameters are picked and reconstructed with all magnetic and SXR diagnostics. The averaged values of the signal effectiveness for reconstructing the current profile width, or α parameter, for all of the magnetic and SXR diagnostics are shown in Fig. 5.12. The signal effectiveness values indicate

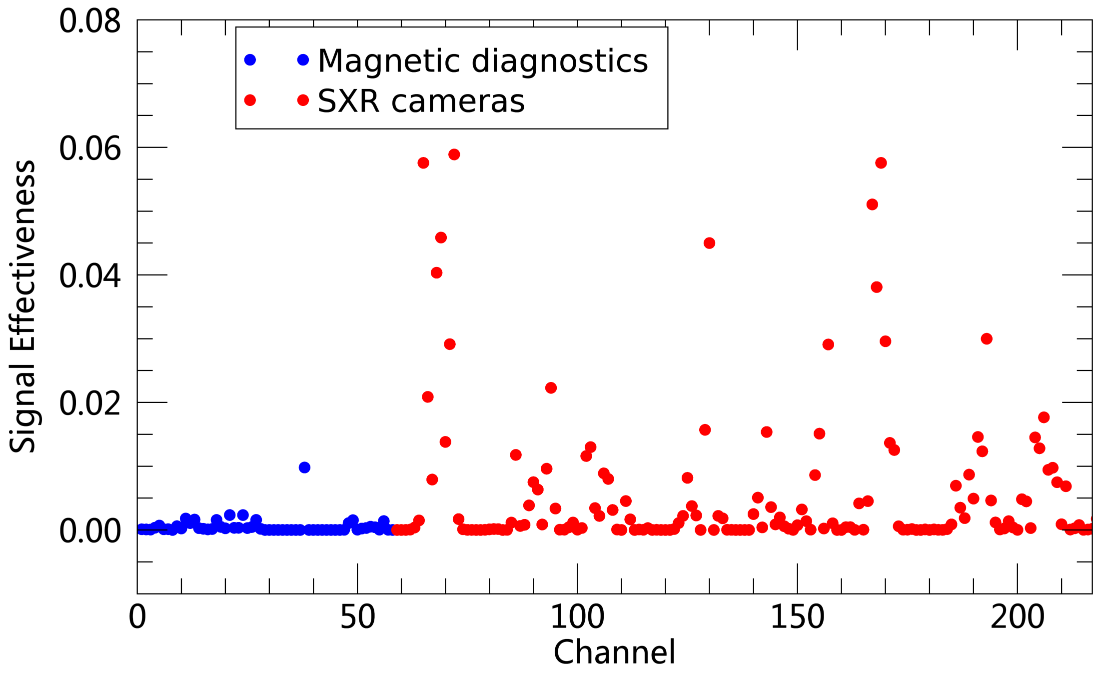

Figure 5.12: The signal effectiveness in reconstructing the α parameter which determines the broadness of the plasma current profile. Those from the magnetic diagnostics are shown in blue and those due to the SXR diagnostics are shown in red.

that the SXR measurements are generally much more effective in determining the current profile parameter α compared to magnetic measurements. The most effective magnetic diagnostic appears to be the full Rogowski coil which measures the total toroidal plasma current.

The details of the signal effectiveness of each SXR camera are shown in Fig. 5.13. There are a few highlights to point out. First, the material or thickness of the filters appears to have no effect on the strength of the signal effectiveness. Generally, the SXR chords at positions with higher gradients of signal strength are found to be more effective. SXR chords that view the very edge of the plasma are not as effective because there the signal values are too low. A few SXR channels from the two central SXR cameras have the strongest signal effectiveness. The SXR channels from the bottom SXR camera at the full period of CTH ($\phi = 0°$) are less effective compared to other SXR cameras at the half period ($\phi = 36°$ and $\phi = 252°$), except the very central channels that are sensitive to the shift of the magnetic axis. This is due to the fact that the geometry of flux surfaces at the full period of CTH is more rigid compared to that at the half period as discussed in Chap. 4.

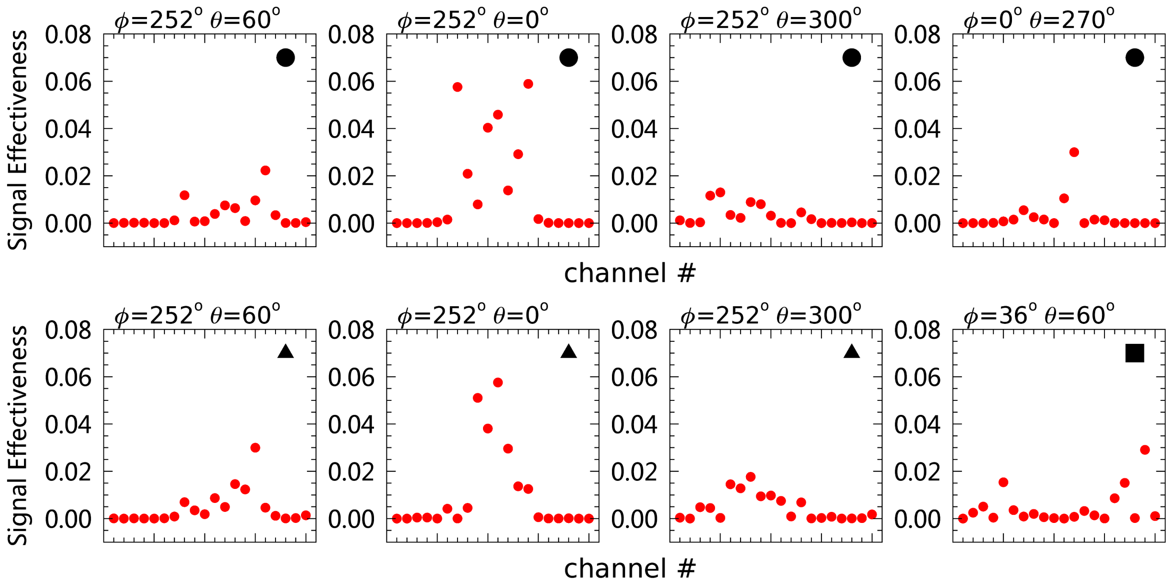

Figure 5.13: Signal effectiveness of all SXR cameras. The black symbols in the upper right portion of each graph (circles, triangles and square) are used to identify cameras with filters made of thin and thick aluminum/carbon foils, and thin beryllium foils respectively.

Similar reconstructions incorporating the SXR emissivity profiles are performed for a set of sixty-nine current-driven plasmas that all exhibit sawtoothing behavior. These discharges are very different in terms of plasma current, density, and external rotational transform settings (imposed stellarator transform). Reconstructions of each discharge are performed in three different ways: using external magnetic diagnostics only; using magnetic diagnostics along with a prior constraint of the location of the $q = 1$ surface; directly using all SXR and magnetic data.

The reconstructed edge safety factor values, $q_{\rm edge}$, are similar for the three methods of reconstruction, showing good agreement with less than 5% difference between methods. That the all three reconstruction methods give similar values for the edge safety factor again highlights the fact that external magnetic diagnostics are effective in determining global characteristics of the magnetic equilibrium only close to the last closed flux surface. The resulting central safety factor q_0 for the same set of sawtoothing shots using the three methods are plotted in Fig. 5.14 against the edge safety factor. It is seen that the central safety factors, q_0, obtained from reconstructions by directly using magnetic and SXR data are consistent with results using the prior constraint of the location of $q = 1$ surface to a percentage difference within 15%. Also from Fig. 5.14 it is seen that the q_0 values obtained from reconstructions using only magnetic

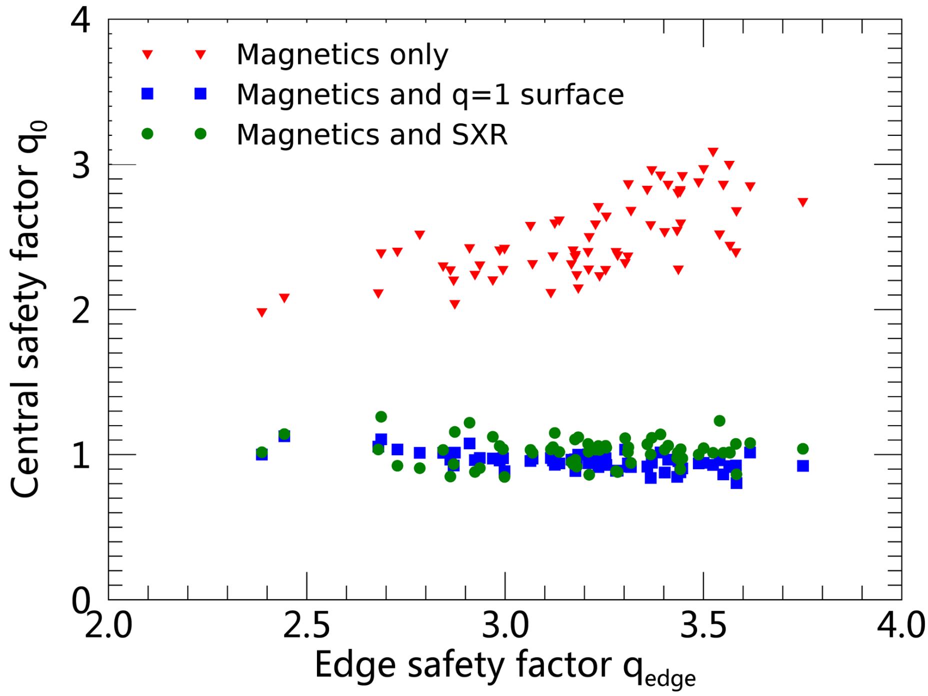

Figure 5.14: Reconstructed central safety factor q_0 values using three different methods.

diagnostics increases with the edge safety factor, and are far from unity for these sawtoothing discharges. This is a clear indication that external magnetics are incapable of correctly diagnosing the changes of the q profile, i.e. the internal current distribution in 3D plasmas as in axisymmetric plasmas.

5.5 Effects of the external vacuum rotational transform on CTH plasmas

Improved equilibrium reconstruction provides an important tool to study the effects of 3D shaping fields on the equilibria of CTH discharges. In this section, a set of plasmas are reconstructed using both SXR and magnetic data. These reconstructions are performed at the time when the plasma current reaches its maximum value, where the time derivative of the value of the plasma current is zero. Different rotational transforms are applied to these discharges. The reconstructed current profiles are compared in several conditions to explore the effects of the vacuum 3D magnetic fields on the current distribution within the plasma.

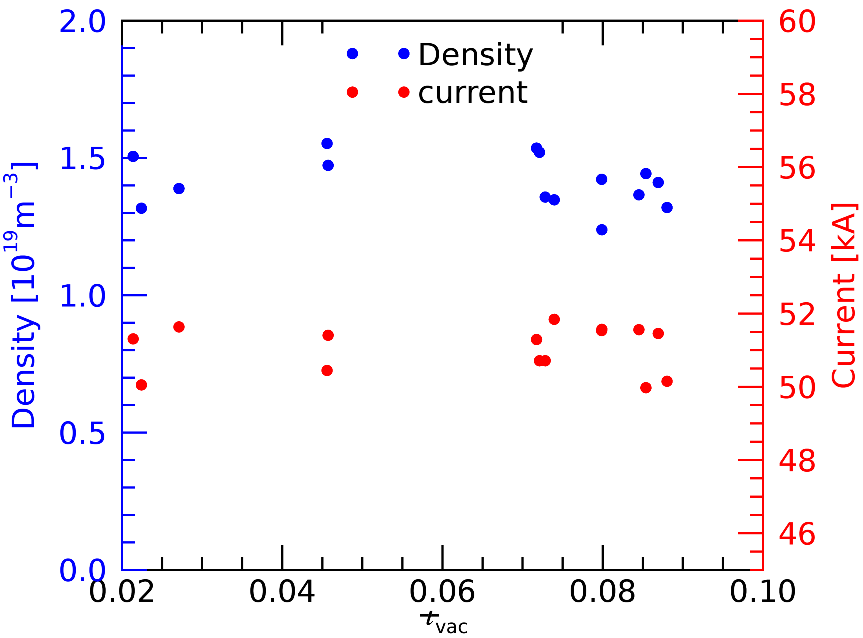

Figure 5.15: Group of discharges with similar current, density, and varying vacuum transforms

First, a group of discharges are chosen to have nearly the same plasma current ($50\,\mathrm{kA}$ - $52\,\mathrm{kA}$), but increasing vacuum rotational transform, varying from 0.02 to 0.09. The variance of the density is small as shown in Fig. 5.15.

The internal inductance l_i, familiar from the specification of tokamak equilibria, is defined as

$$l_i = \frac{\langle B_\theta^2 \rangle_V}{B_\theta^2(a)} \,. \tag{5.4}$$

It is the volume averaged square of the poloidal field, B_θ^2, normalized to the square of the poloidal field at the edge of the plasma, $B_\theta^2(a)$, where a is the minor radius of the plasma. The parameter l_i characterizes the breadth of the current profile in tokamaks. However, since much of the confining poloidal magnetic field in a hybrid stellarator is provided by the current in the external coils, l_i is relatively insensitive to the current profile in hybrid stellarator plasmas, and thus is not particularly useful for distinguishing between different current profiles in CTH plasmas. Instead, we use the full width at half maximum, FWHM, of the current profile in the normalized flux surface parameter s as a measure of the breadth of the current profile.

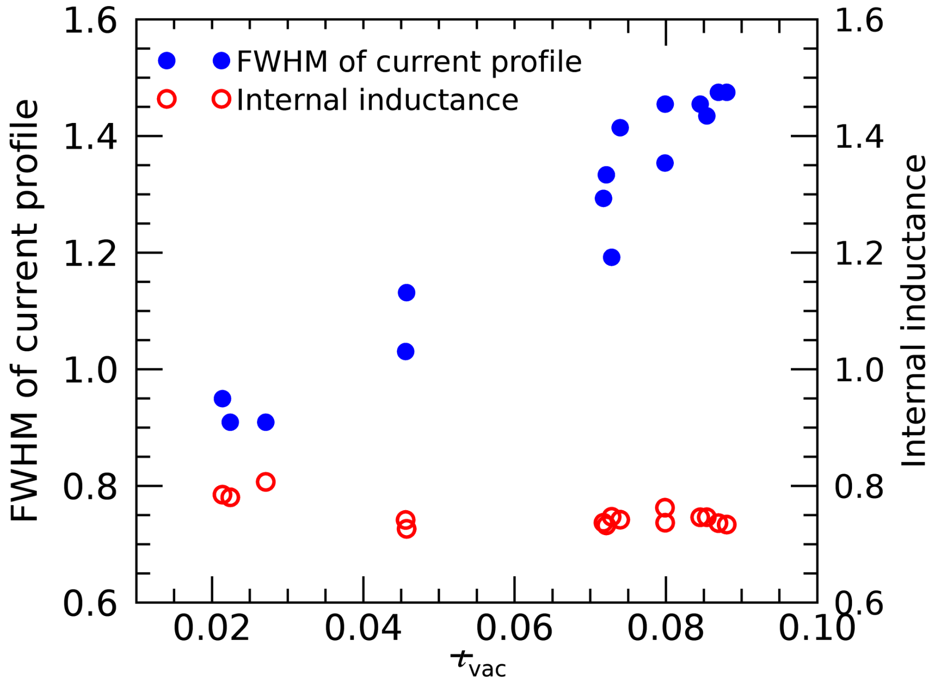

Figure 5.16: The FWHM of reconstructed current profiles and internal inductances are plotted versus the vacuum rotational transform.

The FWHMs of reconstructed current profiles and internal inductances are shown in Fig. 5.16. We find that the current profile becomes significantly broader with addition of vacuum rotational transform, i.e. increasing level of stellarator fields. By comparison, the internal inductance, l_i decreases only slightly as the current profile broadens. That the FWHM and l_i approach the similar magnitude at low values of vacuum transform is just a coincidence.

With the increase in vacuum rotational transform, the portion of the central transform from the central plasma current density must necessarily decrease to keep the net central transform near or below unity, thus leading to a broader current profile for a given value of plasma current. The variation of neoclassical resistivity may also play an important role here. The resistivity depends on the trapped electron fraction, which is strongly affected by the level of toroidal field ripple. These toroidal ripples in a stellarator will be the effective sum of several spectral terms of non-zero toroidal periodicity. The profile of the toroidal magnetic ripples may be different when the magnetic field configuration changes.

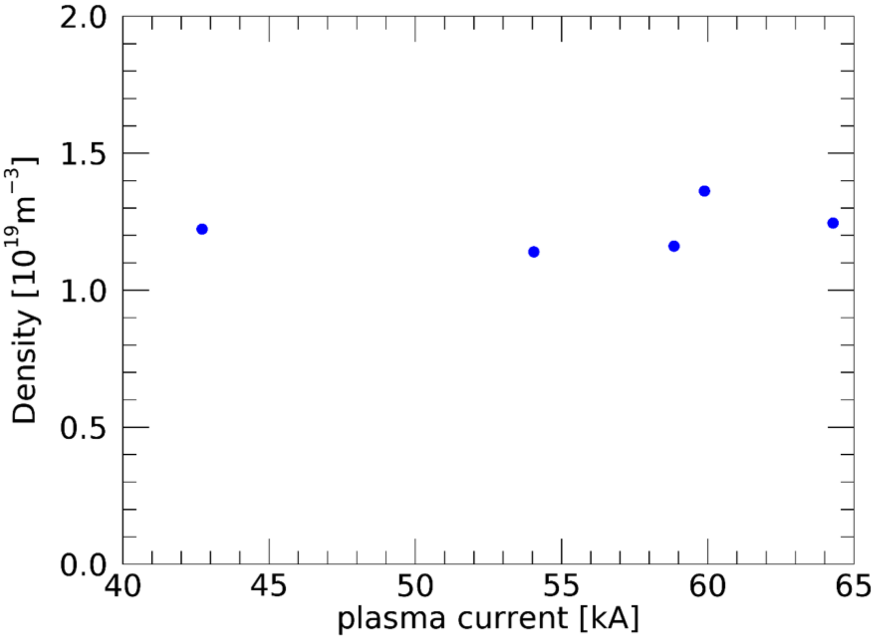

Figure 5.17: Group of discharges with similar densities but varying current

The effect of the value of total plasma current on the current profile is also investigated. A group of plasmas with similar density but different current as shown in Fig. 5.17 are reconstructed. The FWHMs of the reconstructed current profiles are shown in Fig. 5.18. With similar density and vacuum transform, the current profile naturally becomes broader with increasing plasma current. This is due to the fact that the vertical field needed to maintain the plasma in equilibrium depends on both plasma current and the internal inductance. If the external applied vertical field does not change when the total plasma current increases, the internal inductance decreases, resulting a broader current profile.

5.6 Discussion and conclusion

Determination of the plasma current and rotational transform profiles is important for understanding the thresholds for MHD instability and disruption. Previous work has shown that external magnetic diagnostics by themselves are not sufficient to accurately describe the internal state of hybrid discharges in CTH. Because direct measurement of the internal poloidal magnetic field is not available in CTH, we have developed two methods to incorporate SXR

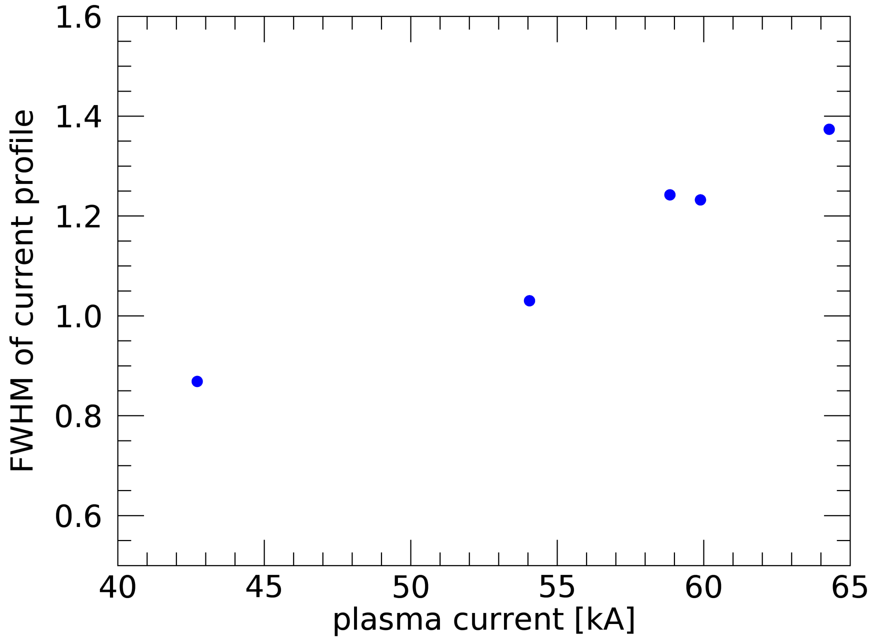

Figure 5.18: FWHM of reconstructed current profiles vs. amplitude of plasma current

measurements in the V3FIT code to improve the reconstruction of the internal plasma current distribution.

In current-driven discharges that are sufficiently dense, the soft X-ray emission often exhibits characteristic sawteeth with an inversion of the phase of the sawtooth evident in the radial profile of the emission. Under the assumption that the radius of the inversion of the sawtooth signals corresponds to the magnetic surface at which $q = 1$ as in tokamaks, the values of the parameters used to fit the plasma current profile can be known with far greater precision that with magnetics alone. In V3FIT, this is performed as a secondary optimization step in which the inversion radius is identified as a flux surface found from the reconstruction performed with magnetics alone, and the current profile is then reconstructed again with the prior knowledge of $q = 1$ corresponding to a particular reconstructed flux surface.

In the second more straightforward approach, measurements from eight SXR camera arrays at different toroidal and poloidal locations are used to reconstruct the geometry of flux surfaces and thus infer the current distribution within the plasma. The original approach of deriving the plasma current distribution from the geometric shape of the flux surfaces through consideration of the MHD equilibrium requirement is based on toroidally symmetric, non-circular cross-section configurations. We have shown that the concept remains valid and practical in a non-axisymmetric stellarator with significant plasma current.

Equilibrium reconstructions of sawtoothing plasmas using SXR and magnetic data predict the central safety factors to be around unity, in agreement with reconstruction results where external magnetic data was used in conjunction with the prior constraint of the location of the $q = 1$ surfaces extracted from SXR emissivity data. Many small-scale or low-field shaped plasmas do not have the ability to directly measure the internal magnetic field, but are equipped with x-ray diagnostic systems that have good temporal and spatial resolution. The technique described in this thesis provides an alternative method that can be used to measure the current distribution, 3D in our case, with reasonable accuracy as demonstrated.

Chapter 6

Density limit disruptions in CTH

The manifestation of a disruption of a magnetically-confined current-carrying toroidal plasma is a sudden loss of confinement immediately followed by a rapid drop of the plasma current and temperature. The disruption expels heat and particles to the edge of the plasma at a rate higher than in a normal discharge, leading to large, outward particle and heat flows to the vessel walls and, if present, divertor. The collapse of the plasma current produces larger than normal eddy currents in conducting plasma facing components and the structure of the confinement device, leading to potentially excessive force-loading, which may exceed material limits in large plasmas. In large tokamaks, the rapid loss of plasma and magnetic energy may thus cause damage. As a result, the avoidance and mitigation of disruptions is considered essential for future tokamak devices such as ITER.

Prior to some disruptions, plasmas often exhibit growing MHD activity that can drive the plasma equilibrium to an unstable disruptive state. Known causes of disruptions include operational limits on density (density limit), pressure (β limit) and current (low-q driven disruption), unstable vertical drifts, and operator or mechanical failure. Disruptions, however, do not routinely occur in current-free stellarators, in which the required rotational transform is produced by external currents. While the lack of plasma current should reduce the drive of current-driven MHD instabilities, it has also been suggested that the inherent 3D magnetic field structure may also play a role in the relative immunity of stellarator to disruption. In tokamak configurations with no vacuum transform, small levels of 3D fields are applied for resistive wall mode[89] and edge local mode[16] suppression, and error field correction[90], effectively controlling the growth of deleterious MHD instabilities. What is then the effect of higher levels of 3D magnetic shaping field, like $B_{\mathrm{3D}}/B_0 \sim 0.1$, on tokamak instabilities and disruptions?

In the stellarator/tokamak hybrid CTH device, the rotational transform from both external coil currents and ohmic driven toroidal plasma current may be applied simultaneously. Earlier hybrid devices have shown evidence of disruption avoidance and improved positional stability[7,8]. In this work, studies of disruptive behavior of current-carrying discharges show that disruptions in CTH hybrid discharges can be reproducibly modified by applying modest levels of externally generated rotational transform from the stellarator coils.

This chapter is organized as follows. First, the density limits of toroidal plasmas in different magnetic confined experiments are discussed in Sec. 6.1, including empirical scaling laws, disruptive phenomenology and underlying physics. Next, the density limiting behavior of CTH plasmas is described in Sec. 6.2. The effect of 3D shaping magnetic fields on the density limit is discussed in Sec. 6.3 An analytical approach of stabilization of MHD instabilities in a current-carrying stellarator is shown in Sec. 6.4. Finally, the conclusion and proposed future work are given in Sec. 6.5.

6.1 Density limits in toroidal plasmas

In various magnetic confinement experiments (tokamaks, reversed field pinches (RFP), stellarators, spheromaks and field-reversed configurations), it is found that there are limiting values of the density that can be achieved even with advanced heating or fueling techniques. Apparently, there is an independent limit on plasma density in addition to the operational limits imposed by MHD stability on plasma current and pressure. Attempts to raise the density beyond the limit result in a termination of the discharge either by disruption or slow collapse. Since the fusion reaction rate scales with n^2, the density limit plays an important role in contracting the parameters of plasmas intended to produce practical fusion power, including ITER.

6.1.1 Scaling law

Since the mid 1960s, many experiments on the density limit have been carried out on numerous tokamak devices operating over a wide range of parameters[91–93]. The data compiled from these experiments have enabled the formulation of scaling law for this phenomenon. Initially, a scaling law, known as "Murakami limit", was found where the maximum achievable density is given by $n_M < B_T/R$[93]. Here B_T is the toroidal field and R is the major radius. The Murakami limit was thought to represent as global power balance between radiation losses and ohmic heating, the latter being roughly proportional to the central current density, $j_o \sim B_T/R$. A subsequent scaling, the "Hugill limit" with the form $n_H = B/qR$, was proposed making use of additional data from devices with gas puffing and auxiliary heating[94]. It revealed an important relationship between the maximum attainable plasma density and the current density, since for circular, high aspect ratio limit, $B_T/qR \sim I_p/a^2$. A similar expression for the density limit had also been found in RFP devices[95,96]. In RFPs, the operating range was usually parameterized as I/N, where I is the plasma current and N represents the number of particles per unit toroidal length. The I/N scaling is equivalent to the Hugill limit B/qR or I_p/a^2.

With data from shaped plasmas, it was found that the coefficient in front of the Hugill limit B/qR could vary significantly from device to device. For strongly shaped plasmas, the difference could be a factor of 2 or more. With more data from an array of devices, a new scaling law was proposed by Greenwald[23] in which the maximum density limit is given by the equality:

$$n_{\mathrm{G}} = \frac{I_p}{\pi a^2} \tag{6.1}$$

It is assumed that the plasma has a roughly elliptical cross-section in the poloidal plane, with a horizontal width of $2a$ and the vertical height of $2\kappa a$ ($\kappa \geq 1$). I_p is the plasma current in MA, and a is the semi-minor radius of the plasma in units of m, and n_{G} is the maximum attainable line-averaged density expressed in units of $10^{20} m^{-3}$. The Greenwald limit in Eq. 6.1 is equal to the Hugill limit for circular cross-section plasmas, but is significantly higher for experiments with vertically-elongated plasmas. The empirical Greenwald density limit is currently the most common figure of merit to predetermine the maximum operating density of tokamak plasmas. Fig. 6.1 shows the Greenwald limit versus the measured densities of a set of discharges from three tokamak devices[4]. The empirical limit appears to define the operational limit well in both circular (Alcator C) and highly shaped plasmas (DIII and PBX).

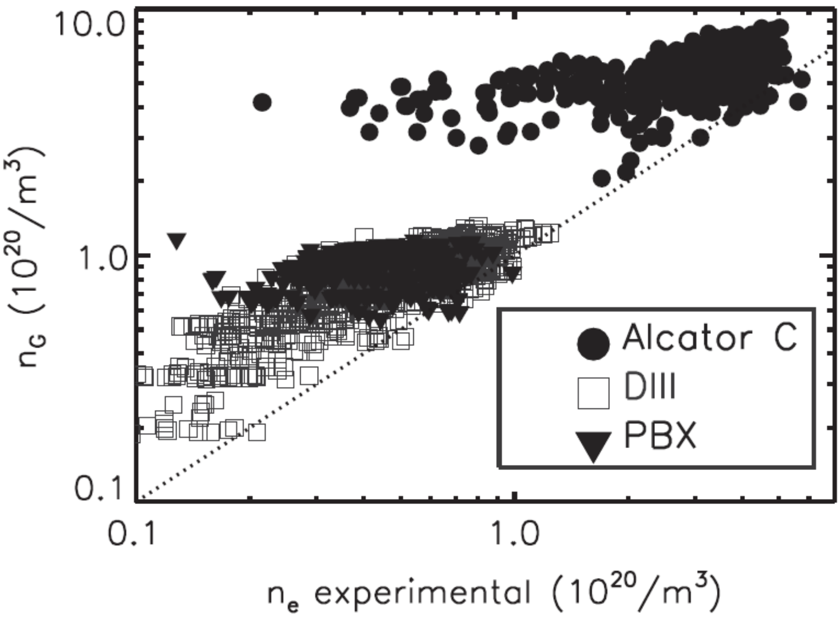

Figure 6.1: Measured densities are plotted against the Greenwald limit for a set of experiments. Figure from Ref [93].

The scaling of maximum operating density in current-free stellarators is different, particularly as there is little to no plasma current. The density limit observed in stellarators is not associated with disruptions, but correlates with the heating power. A scaling law was first reported from Heliotron E with scaling formula[97]:

$$n_{\text{limit}} = 0.25 \left(\frac{P_{\text{in}} B}{a^2 R} \right)^{0.5} . \tag{6.2}$$

Here n_{limit} is the line average electron density ($10^{20} m^{-3}$), P_{in} is the absorbed power (MW), B is the magnetic filed strength on the plasma axis (T), a is the average minor radius (m) and R is the major radius m. With more data from other experiments, a general power law has been formed to fit with exponents varying from $P_{\text{in}}^{0.5 \to 1.0} B^{0.5 \to 1.0} / R^{0 \to 1.5}$[97–99].

The stellarator density limit takes the form of a quenching of the stored plasma energy on the confinement time, suggestive of a mechanism driven by slow scale radiative collapse, independent of MHD stability issues. Accordingly, the densities achieved in stellarators may be significantly higher than in tokamaks of comparable dimensions if sufficient heating power is available.

6.1.2 Observations and underlying physics

Most extensive studies of density limit disruptions have been conducted in tokamak devices. They typically link the limit to physics near the boundary of the plasma. Several phenomena may be observed as the density is raised toward the density limit. They include the appearance of MARFEs [100,101], divertor detachment [102,103], a drop in H-mode confinement [104–106], changes in ELM activity [107], a transition from H-mode to L-mode [105,108,109], poloidal detachment [110,111], increase of coherent MHD oscillations concurrent with a peaking of the current profile [112,113], and finally major disruptions. The first four, MARFEs, divertor detachment, H-mode degradation and the changes in ELM activity can happen over a wide range of densities, varying from $0.3 - 0.9\, n_{\mathrm{G}}$. The other phenomena, the H/L mode transaction, poloidal detachment, shrinkage of current density profile, growing MHD activity and the disruptions, occur at or near the limit density n_{G}.

Cooling of the edge is a key element in all observations, suggesting that radiation may play an important role in density limit driven disruptions [4]. Observations of discharges with peaked density profiles that exceed the Greenwald density limit supports the hypothesis that the physics underlying the density limit is to be found in the edge of plasmas. Neutron beam injection (NBI) [114,115], pellet injection [116–118] and transport modification [119,120] have been used to obtain peaked density profiles with line-averaged densities in excess of Greenwald limit. In these experiments, the edge density remained below the limit to trigger disruptions while the increase in the line-averaged density came from particles in the core of the plasma. This finding is consistent with proposed mechanisms that attribute the density limit to physics in the edge of plasma.

The manifestation of the density limit is quite different in stellarators. A soft limit or thermal quench may be encountered in stellarator plasmas with sufficient high density [97]. If the density is reduced by lowering the gas puffing, a stellarator may recover from the quench [99]. Alternatively, thermal collapse could be triggered by strong gas fueling or by lowered heating power in an established high-density discharge. During the collapse, a large increase in radiation from low Z impurities is observed similar to MARFEs and poloidal detachments phenomena in tomakaks, suggesting an important role of radiation in the limit. But it is still not clear that the collapse is due to the same edge physics as in tokamaks.

6.1.3 Physical mechanisms

Although density limit disruptions have been observed for several decades, there is not a first-principles theory available that is universally accepted, or even agreement on the essential mechanisms. However, there is a general agreement on the final scenario of the density limit, in which edge plasma cools, current profile narrows, growing MHD instabilities (usually $m/n = 1/2$ tearing mode) occur followed by a loss of MHD equilibrium, and final disruption[22]. All phenomena of the density limit in tokamaks are associated with the cooling of edge plasma, suggesting a unifying mechanism. Several theories and models have been proposed to explain the cause of the edge cooling.

Because the radiated power form a plasma increases with density[121] and plasmas with high levels of impurities tend to be thermally unstable and cannot achieve high densities[92], several radiation models have been considered, including core radiation from high Z impurities[93], formation of thermal condensation or MARFEs[122], radial detachment[123,124], and divertor detachment[125,126]. These models were able to reproduce some features of disruptions in certain cases with good quantitative agreement. However, they are not entirely satisfactory as they require assumptions about edge transport, which is not well understood yet, and make predictions about power and impurity scaling that is not consistent with experimental observations[4].

Another approach focuses on the enhanced turbulent transport. There is evidence that increased edge transport at high densities is responsible for the edge cooling[127–131]. Accordingly, several models have been developed to explain the increase of transport at high densities and its relation to the density limit[132–135]. Simulation work has successfully discovered regimes of extremely large turbulent transport, which, to a certain extent, is consistent with experimental observations. However, further investigation is needed to find a comprehensive and well-characterized edge turbulence model. Present transport-based models are not able to make quantitative predictions. Both radiation and transport models have experimental ramifications that need to be pursued.

More recently, the thermo-resistive effect, is being reconsidered to explain the physics behind the tokamak density limit. It combines several important effects with regard to tearing stability, including thermal effects on the 3D resistivity distribution[136–140]. Specifically, it is a combination of nonlinearly-growing tearing modes leading to current profile narrowing and a model of radiation driven islands. Some new features are included: island asymmetry due to finite island width; a radiation model based on local coronal equilibrium; current perturbations due to perturbed resistivity; numerical solution of the cylindrical eigenfunctions and tearing mode driven instability parameter Δ'. The thermal-resistive formalism is found to be able to quantitatively reproduce the Greenwald density limit. To justify this mechanism, further investigation with experimental data of high spatial resolution is needed, which can be quite challenging.

6.2 Density limit disruptions observed in CTH

Studies of density limit disruptions are carried out in CTH in discharges with the rotational transform produced by both the toroidal plasma current and current in the coils. The density limit manifests itself as a major disruption in CTH despite some transform being provided by external coils. The density limit is reached by ramping the density using strong fueling from the edge.

Fig. 6.2 shows two discharges with similar vacuum transform of of $\iota_{\rm vac} = 0.05$. The density signals are line-averaged densities from the central channel of the interferometer system. In one discharge (12090650), the density was kept constant at a low value, and the discharge did not disrupt. In the other discharge (12092048), strong gas puffing caused the density to ramp up until a disruption occurred. The phenomenology of these terminations are similar to tokamak disruptions. There is a negative loop voltage spike coincident with a positive current spike followed by a sharp collapse of plasma current. In addition, there is a growing coherent MHD precursor to the disruption detected with poloidal magnetic pick-up coils.

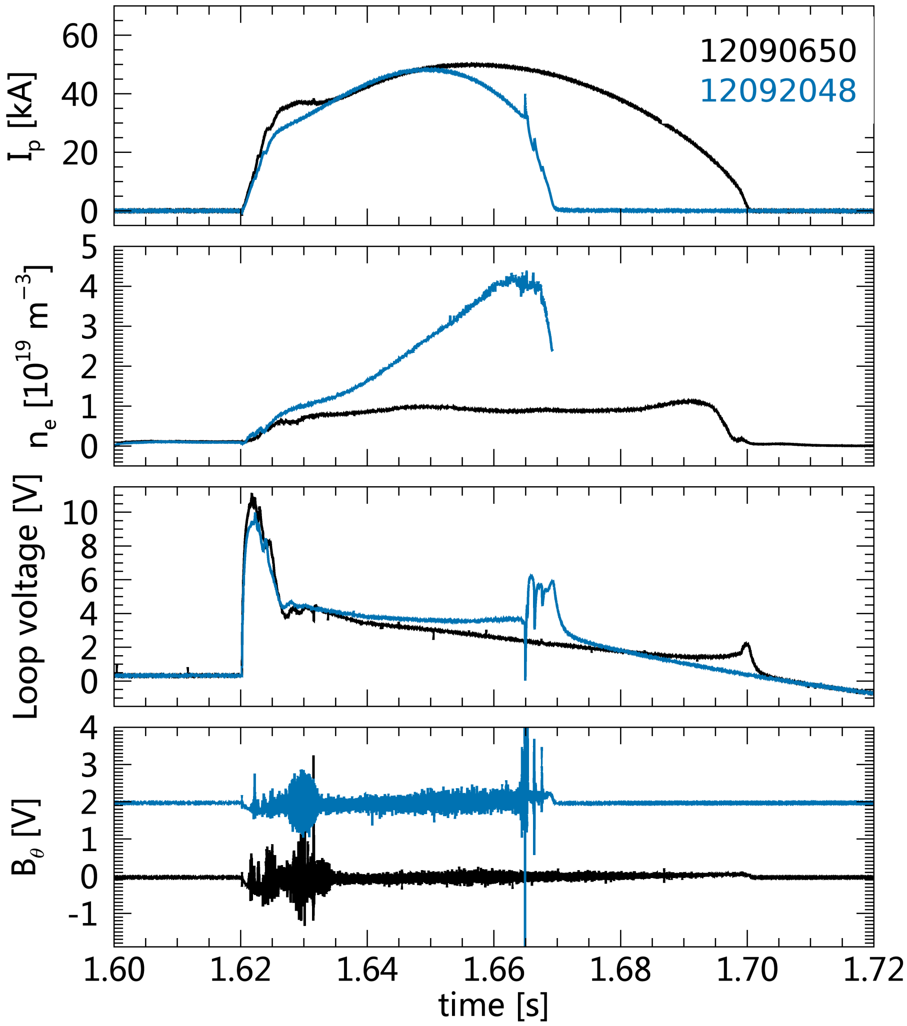

Figure 6.2: Two discharges with different density but similar vacuum transform of $\iota_{\mathrm{vac}} = 0.05$. From top to bottom are plasma current I_p, line-averaged density n_e, loop voltage and poloidal magnetic coils B_θ.

Another disrupting plasma 14092626 is shown in Fig.6.3, displaying the evolution of plasma current, density, loop voltage, and magnetic fluctuation measured by one of the poloidal magnetic pick-up coils. A expanded view of the magnetic pick-up signals (precursors to the disruption) is shown on the right. Before the disruption occurring, during the time interval

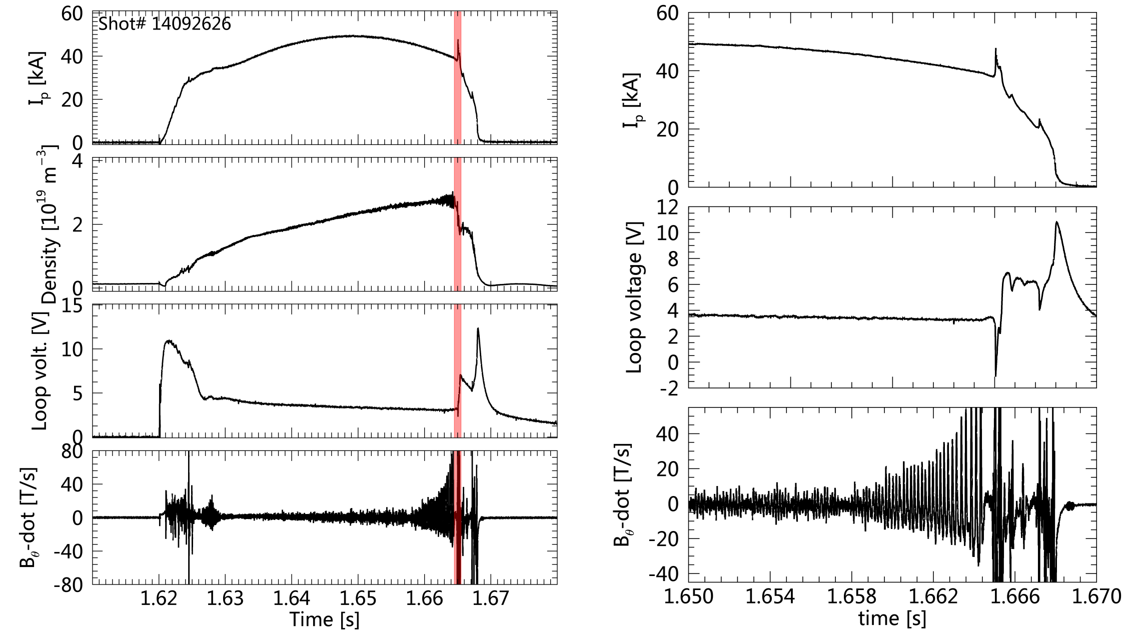

Figure 6.3: A disrupting plasma showing the time evolution of plasma current, density, loop voltage and magnetic fluctuations measured by one of the magnetic pick-up coils. Disruption occurs during the time interval highlighted in red; the expanded view of the red box is shown at the right.

within the red box in the left-hand figure, the same precursors as in a tokamak are observed: strong MHD fluctuations growing early, a positive current spike followed by sudden current quench, sharp termination of density at sufficient level, negative loop voltage spike. The negative voltage spike is believed to result from a sharp drop of plasma inductance.

CTH is equipped with several sets of toroidal and poloidal magnetic pickup coils, which are used to measure MHD fluctuations. The pick-up signals are used to analyze the magnetic fluctuations of the discharge in Fig.6.3 before disruption. A contour plot of the result is shown in Fig.6.4. The data shows a mode structure, with poloidal mode number $m = 2$ and toroidal mode number $n = 1$, consistent of tearing mode at the flux surface with rotational transform $\iota = 1/2$. The mode rotates and locks approximately $1\,\mathrm{ms}$ before disruption. To evaluate the time evolution of the $2/1$ mode, singular value decomposition (SVD) is applied to the data.

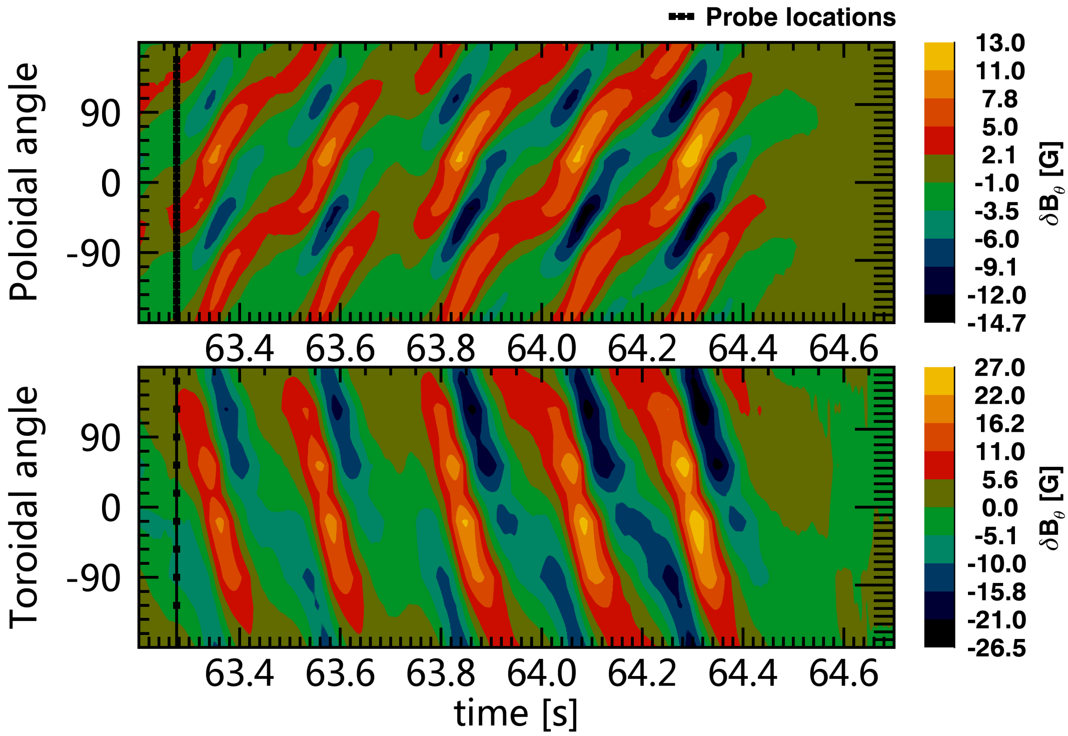

Figure 6.4: Contour plot of the magnetic fluctuations prior to the disruption (Shot:14092626). Time is plotted on the x-axis. Measurements from a poloidal array of 16 pickup coils and a toroidal array of 10 coils are shown on the top and bottom panel respectively. The black band near the left y-axis shows the poloidal and toroidal position of these coils. The color represents the amplitude (positive and negative) of the magnetic fluctuation δB.

The extracted amplitude of the $2/1$ mode is shown in Fig. 6.5. It is clear that the $2/1$ tearing mode grows until the discharge terminates.

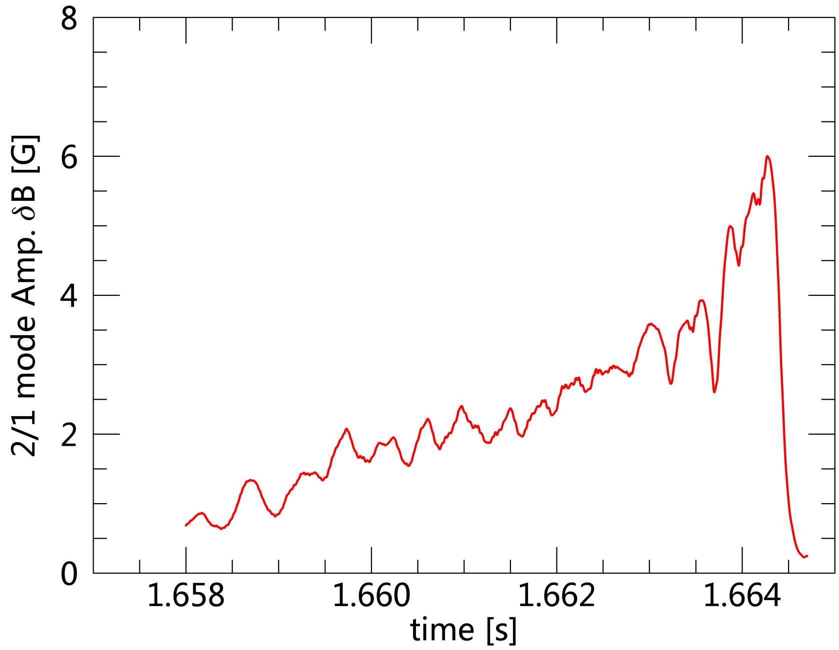

Figure 6.5: Time evolution of the amplitude of $m/n = 2/1$ tearing mode extracted from the magnetic fluctuations using singular value decomposition (Shot:14092626)

A growing oscillation in the plasma density trace occurs, as shown in the upper plot of Fig.6.6, indicating strong poloidal perturbation of the magnetic flux surface by the MHD instability. Sawtooth relaxations are frequently observed in these high-density CTH plasmas. Sawtooth activity shown in this figure turns into sinusoidal oscillations prior to disruption. Fig.6.7 shows the result of SVD analysis of the SXR signals within the time window between $1.6634\,\mathrm{s}$ and $1.6644\,\mathrm{s}$. As a comparison, the magnetic perturbation in the same time interval measured by one of the poloidal pick-up coils is shown in Fig.6.8. The largest temporal modes from the SXR signals are oscillating with the same frequency as the magnetic perturbation signals. Fig.6.9 shows the reconstructed SXR signals using the first three dominant modes. The contour plot shows a clear $m = 1$ structure. Prior to the disruption, as the $m/n = 2/1$ MHD fluctuation grows and destroy flux surfaces in the edge of the plasma , it naturally drives the $m/n = 1/1$ mode at the $q = 1$ surface near the core of the plasma. The $m = 0$ sawtooth

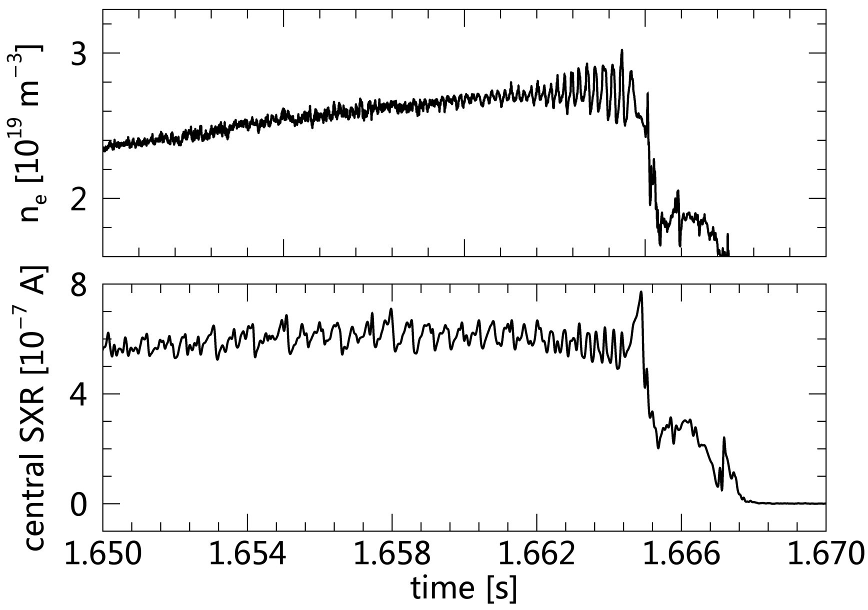

Figure 6.6: Strong oscillations grow up in the plasma density (Shot:14092626). The sawtooth relaxations in the SXR signal turn into sinusoidal oscillations prior to disruption.

relaxations turn into sinusoidal oscillations with the same frequency as the magnetic perturbations. The $m/n = 2/1$ mode near the edge of the plasma and the $m/n = 1/1$ mode in the center are coupled and eventually terminate the magnetic confinement through fast magnetic reconnection.

Reconstructions are performed with both SXR and magnetic data for the discharge in Fig.6.3, to determine the evolution of the current profile. The values of the reconstructed edge safety factor q_{edge} and the FWHM of reconstructed current profile are shown in Fig. 6.10. Before the disruption, a sudden radial narrowing of the current profile is observed, resulting a steeper current gradient. The growing $m/n = 2/1$ tearing mode is recorded by magnetic pickup probes, as shown in Fig. 6.5. This is consistent with classic picture of density limit disruptions in tokamaks, in which the density limit is preceded by the appearance of tearing modes, frequently with poloidal mode number $m = 2$ and toroidal mode number $n = 1$, growing exponentially on a resistive growth timescale[141]. The standard hypothesis suggests the peaking of current profile leads to the growth of tearing modes[142–144], i.e. steep current gradient at a low-order rational surface.

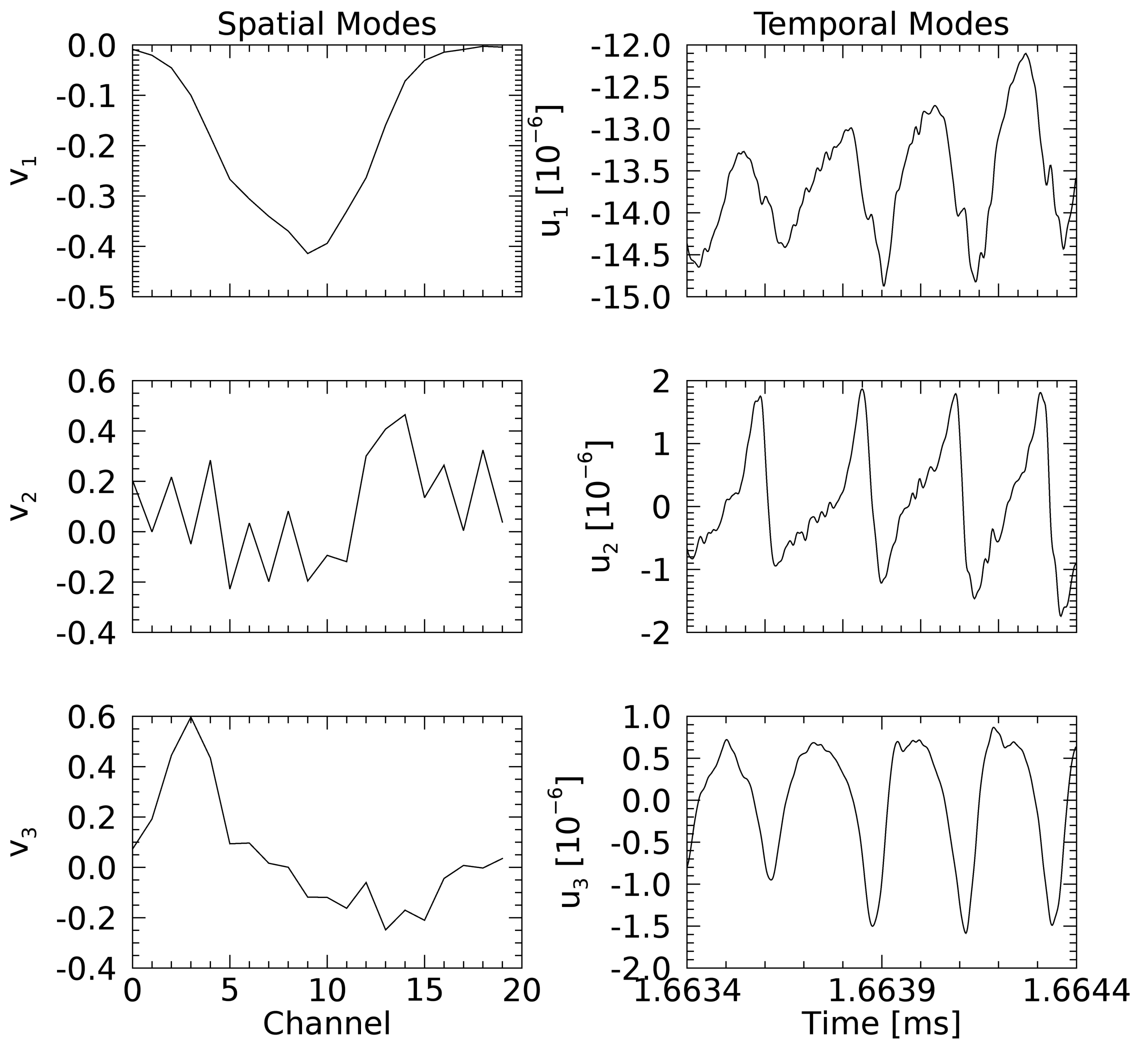

Figure 6.7: SVD analysis of the SXR signals within a time window between $1.6634\,\mathrm{s}$ and $1.6644\,\mathrm{s}$. The largest three spatial and temporal modes are plotted on the left and right respectively.

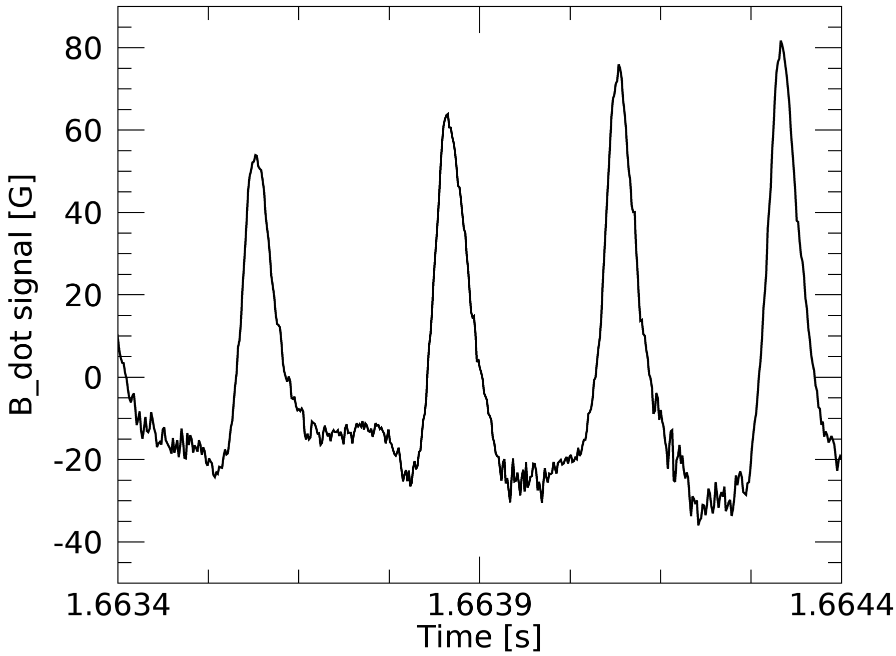

Figure 6.8: Magnetic perturbation signal in the time window between $1.6634\,\mathrm{s}$ and $1.6644\,\mathrm{s}$.

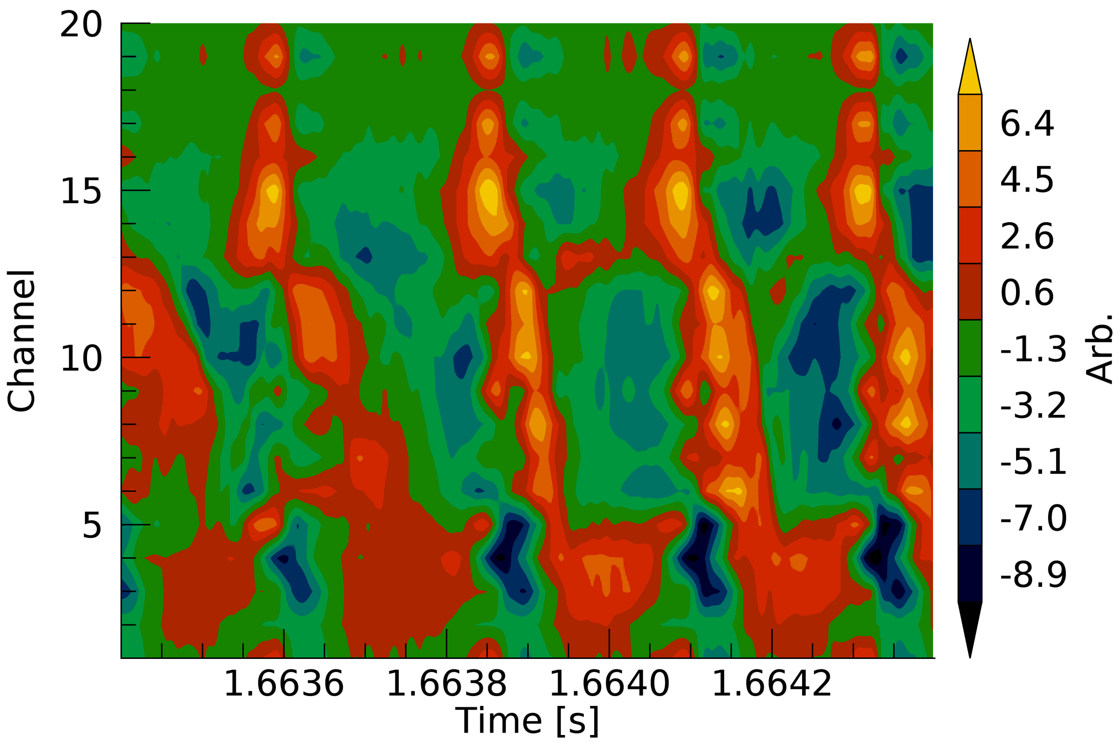

Figure 6.9: Contour plot of reconstructed SXR signals using the three dominant spatial and temporal modes obtained by SVD. The channel number of the SXR chords is plotted on the y-axis, and the time on the x-axis.

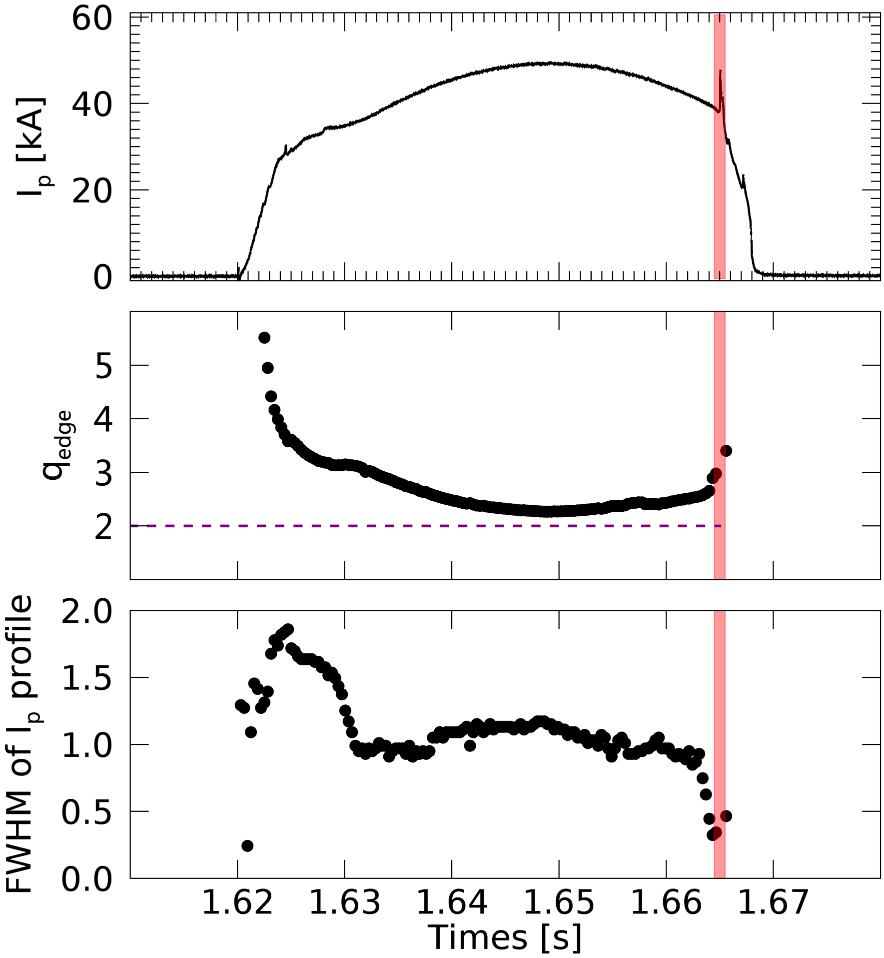

Figure 6.10: Time evolution of the plasma current, reconstructed edge safety factor q_{edge} and FWHM of reconstructed current profile for discharge 14092626

What is more, we also find that the density at disruption is observed to be independent of plasma current evolution. Fig. 6.11 shows two discharges with similar vacuum transform of of

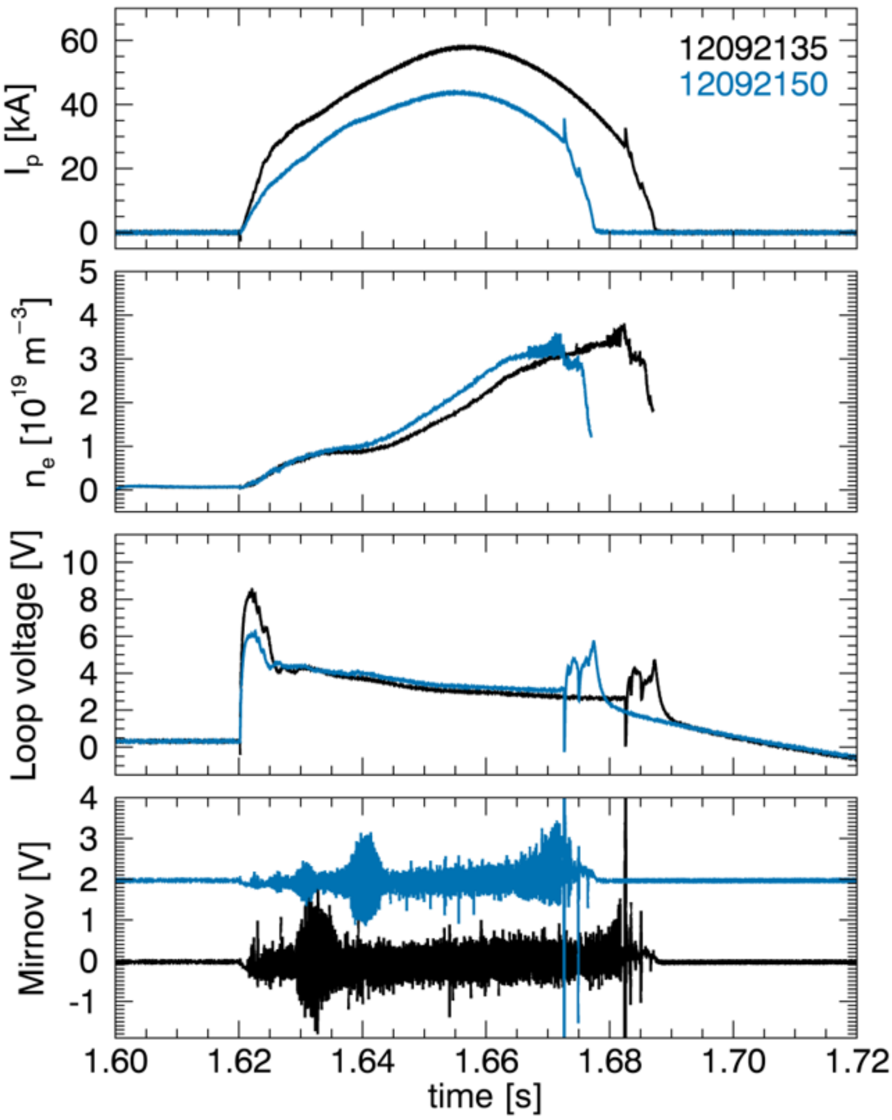

Figure 6.11: Two discharges with different programmed loop voltage but similar vacuum transform of $\iota_{\rm vac} = 0.07$. From top to bottom are plasma current I_p, line-averaged density n_e, loop voltage and Mirnov loop signals.

$\iota_{\rm vac} = 0.07$. They have different programmed loop voltage, and consequently exhibit different evolution of the plasma current. But they both disrupted at similar plasma current and density. The disruption occurrence correlates with plasma current and density as in tokamaks.

The phenomenology of density limit disruptions in current-carrying discharges of CTH is seen to be similar to tokamak terminations. What makes CTH special is that it has the flexibility to change the amount of 3D fields applied to the plasma independent of plasma current. The following analysis includes experimental data from three groups of density limit disrupting plasmas (506 discharges) taken between 2012 and 2016 with different levels of imposed vacuum transform, plotted in Fig. 6.12. They are categorized with low $(0.02 - 0.04)$, medium

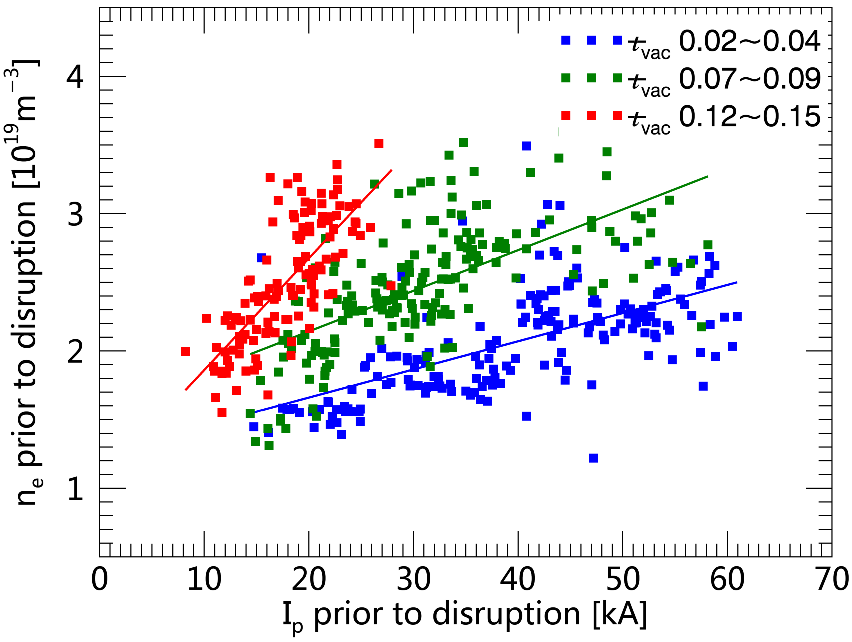

Figure 6.12: Line-average densities and currents just prior to disruption for three groups of plasmas with different levels of imposed vacuum transform. The blue, green, and red symbols represent discharges with vacuum transform ranges of $0.02-0.04$, $0.07-0.09$, and $0.12-0.15$ respectively.

$(0.07 - 0.09)$ and high $(0.12 - 0.15)$ vacuum transforms. The density is the maximum attainable one in a discharge. The default density reading calculated from the interferometer measurements uses a fixed plasma width of $0.25\,\mathrm{m}$. A correction is made by including the actual width of the plasma at where the interferometer is located using reconstructed plasma equilibrium. The recorded density at disruption follows the trend of Greenwald limiting behavior in that it increases with the plasma current. However, there is an additional dependence on the level of imposed vacuum transform evident from the slope of the trend lines. As the level of vacuum transform increases, the slope of the relationship also increases, i.e. for a given current, higher density is achieved with the addition of vacuum transform in a discharge that would have otherwise disrupted at lower imposed vacuum transform.

A contour plot that includes all discharges with density limit disruptions during the same time is shown in Fig. 6.13. The x and y-axes represent the plasma currents and densities prior to disruptions. The color bar identifies the level of vacuum transform applied. Fig. 6.13 shows

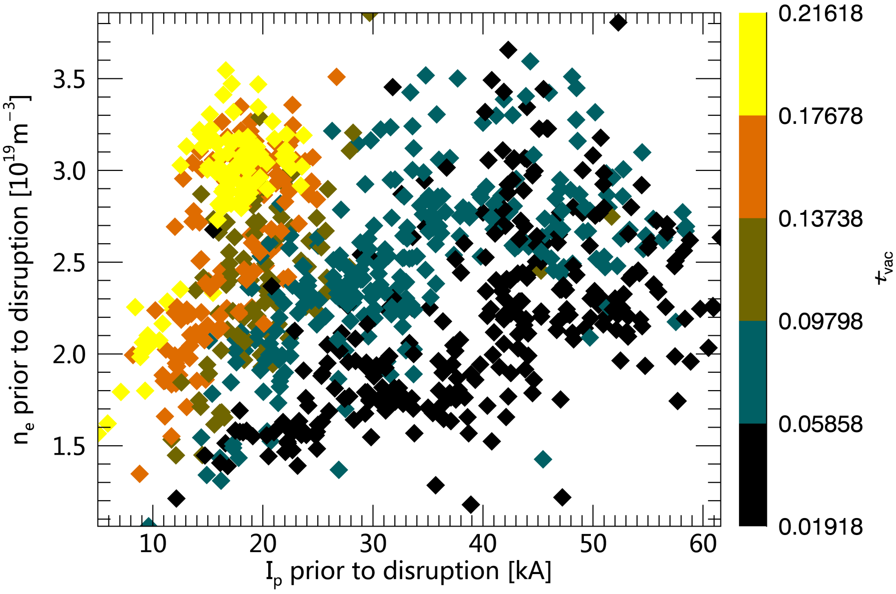

Figure 6.13: Contour plot showing currents and densities prior to disruption for over 800 density limit disrupting discharges with different levels of imposed vacuum transform.

clear boundaries between different groups of discharges with different levels of imposed vacuum transform. As noted before, the density achieved prior to the disruption scales with the current and the density at which disruption occurs rises for given current with addition of vacuum transform.

For the same set of discharges, the values of the density before disruption are normalized to the empirical Greenwald limit and plotted versus the vacuum transform. The result is shown in Fig. 6.14. The original form of the Greenwald limit, $I_\mathrm{p}/\pi a^2$, is generalized for magnetic configurations with toroidal symmetry and is essentially the averaged toroidal current density. Since plasmas in CTH are three-dimensional and highly non-axisymmetric and the shape of the

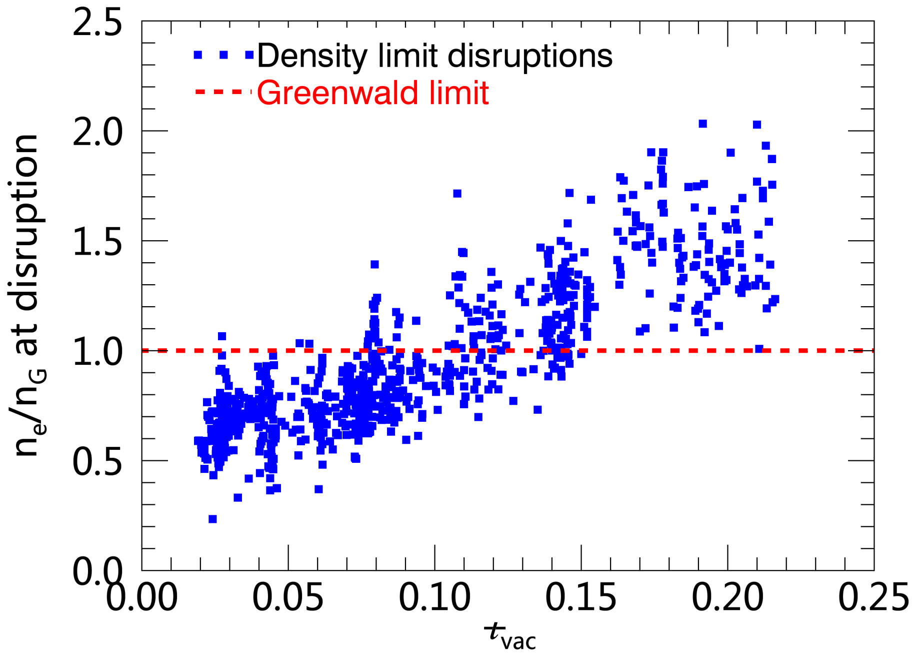

Figure 6.14: Densities before disruption, normalized to the empirical Greenwald density limit, versus the level of vacuum transform.

poloidal cross-section varies in the toroidal location, the expression of the Greenwald limit in CTH is calculated using toroidal averaged poloidal cross-sectional area A_{AVG} from equilibrium reconstructions as $n_{\mathrm{G}} = I_{\mathrm{p}}/A_{\mathrm{AVG}}$. At the lowest value of vacuum transform close to the tokamak limit of CTH, disruptions happened with density near $0.5\ n_{\mathrm{G}}$. As the vacuum transform is increased, the normalized density limit increases by a factor of nearly 4, where some discharges disrupted with density at around $2.0\ n_{\mathrm{G}}$. Attempt to use the semi-minor radius at the half period of the plasma (where the interferometer is located) as the a in the expression results in similar patterns. However, in contrast to earlier work on W7-A[8] and JIPPT-II[147], we have not found a threshold value of vacuum transform that eliminates disruptions. Experimentally, we find that we can achieve similar densities without disruption at lower plasma current when the vacuum transform is raised. Operationally, discharges with higher vacuum transform tend to have lower current for a given ohmic drive. We believe that the confinement is lower in hybrid discharges with increasing vacuum transform.

Continued effort to improve the reconstruction of current profiles in CTH serves the purpose of a better understanding of the effects of strong 3D shaping on MHD induced instabilities and disruptions. With improved equilibrium reconstruction capability using soft X-ray measurements, a sub set of discharges are reconstructed when both SXR and magnetic data are available. For each discharge, equilibrium reconstruction is performed just before disruption. The reconstructed parameters include the total toroidal flux, SXR emissivity profiles, and the current profile parameter α. The FWMH of the reconstructed current profile is used as a measure of the current profile peakedness. Fig. 6.15 shows the FWHM of th current profile versus the vacuum transform, ι_{vac}. Assuming that the current profile narrows prior to a disruption

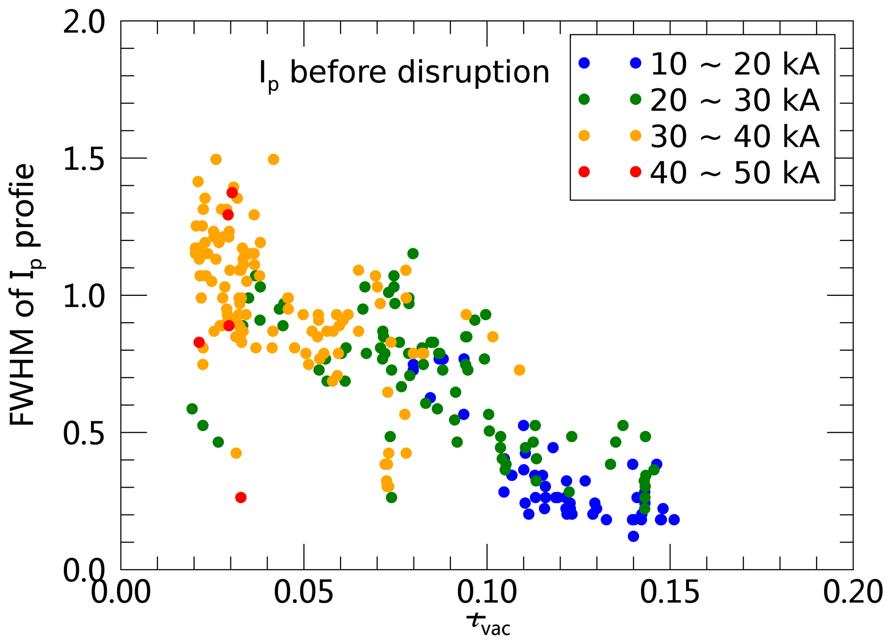

Figure 6.15: FWHM of reconstructed current profiles before disruption plotted versus the vacuum transform ι_{vac}

as indicated in Fig. 6.10, Fig. 6.15 reveals a trend that the current profiles narrow to a greater extent before disruption as the external transform is raised. In other words, disruptions at high vacuum transform take place with very peaked current profiles, despite that higher vacuum transforms typically are associated with broader equilibrium current profiles in plasmas with moderate density (see Fig. 5.16).

The level of imposed vacuum transform or 3D magnetic fields has substantial effects on the density limit behavior of CTH plasmas. Equilibrium reconstruction is helpful to provide time evolution of the current density profile in order to investigate the effect of 3D shaping fields. Two disrupting plasmas with different levels of vacuum transform are shown in Fig. 6.16. They

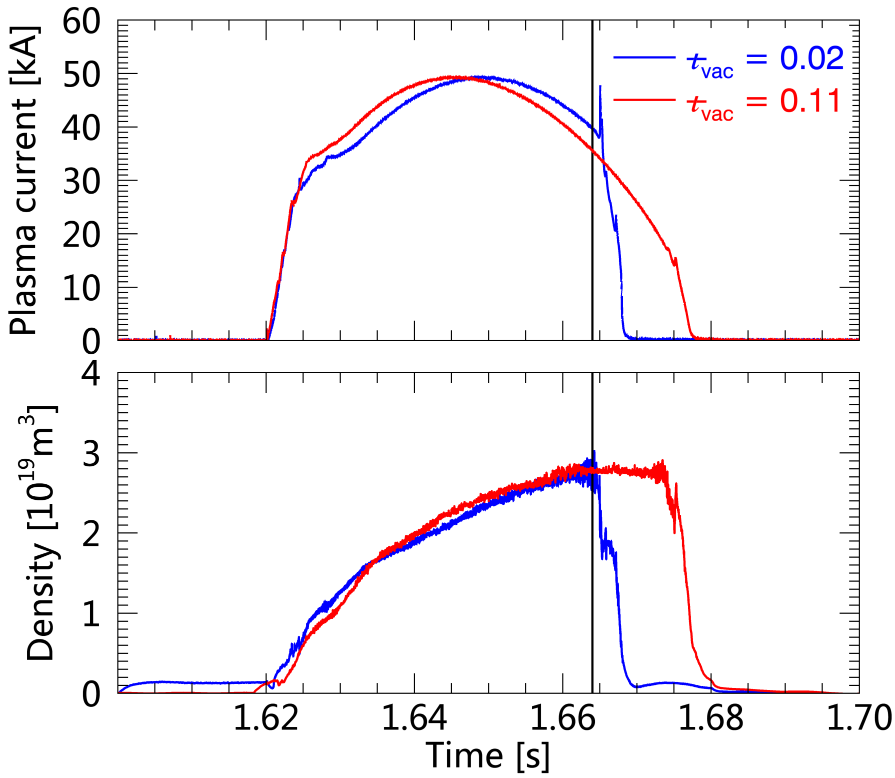

Figure 6.16: Two discharges with low (blue, shot:14092626) and high (red, shot:14110713) levels of vacuum transforms ending in density limit disruptions. both discharges have similar currents and densities until the blue discharge with lower vacuum transform disrupts earlier. The red discharge with higher vacuum transform disrupted later at a similar density but lower current.

both ended in density limit disruptions. The discharge shown in blue has a lower vacuum transform of 0.02, while the discharge shown in red has a higher vacuum transform of 0.11. Both discharges have similar current and density traces up to the time when the shot with lower vacuum transform disrupts earlier. The discharge with higher vacuum transform disrupted later at a similar density but lower current. To investigate the time evolution of current profiles, reconstructions are performed for two discharges at the same time slice when the low vacuum transform discharge disrupted. The reconstructed safety factor q and current profiles at that

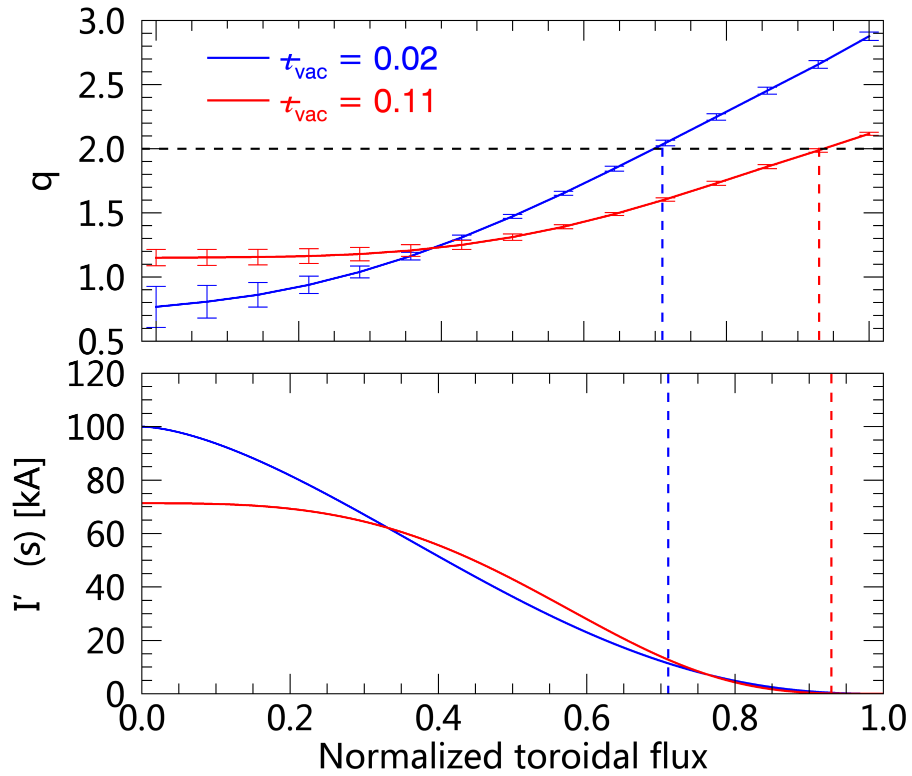

Figure 6.17: Comparison of reconstructed current (bottom) and safety factor q (top) profiles at the moment when the low vacuum transform discharge disrupted while the discharge with higher vacuum transform did not. The intersection of the black dashed lines indicate where the rational surface $\iota = 1/2$ ($q = 2$) is radially located in each discharge.

moment for the two discharges are shown in Fig. 6.17. The addition of vacuum transform broadens both current and transform profiles, effectively moving the $q = 2$ surface towards the edge of the plasma, and thus reducing the current profile gradient at this rational surface where tearing modes may be driven. It therefore allows for a more peaked current profile before the plasma becomes MHD unstable to the $m/n = 2/1$ mode.

6.4 Stabilization of MHD instabilities

It has been demonstrated both theoretically and experimentally that resistive tearing and kink modes can be stabilized by interaction between current and safety factor q profiles[142,143,145]. A characteristic stability parameter for tearing modes, Δ', is derived from a finite-resistivity approach. It has been shown that the condition for tearing-mode instability is $\Delta' > 0$. Stability diagrams for tearing modes with different mode numbers m have been calculated using a series of plasma current models corresponding to increasingly flattened current distributions, to find the stable regimes. Based on the analysis, in terms of the possibility of operating at low q_{edge} values without encountering instability, the flatter profile is preferable to the peaked one.

Stabilization of MHD instabilities in a current-carrying stellarator has been analytically investigated [146,147]. The computation of stability diagrams in a cylindrical current-carrying stellarator with circular cross section is presented in Appendix. D. Based on the theoretical calculation, for the $l = 2$ stellarator with $\iota_{\text{vac}} > 0.5$, the magnetohydrodynamic stability against kink and tearing modes is improved compared to that in tokamaks.

Comparisons of theoretical calculation and experimental observation are reported in the Wendelstein VII-A [8] and Wendelstein VII-AS stellarators [148]. On WVII-A, the Δ'-analysis was applied to calculate the dependence of saturated amplitude of tearing modes on the current density profile. It was found that the addition of external rotational transform shifts the resonant $q = 2$ surface towards the edge of plasma, where the current density gradient is smaller, and stabilizes the $m/n = 2/1$ tearing mode, as observed experimentally. What is more, the current disruption is suppressed in ohmically heated discharges with external transform larger than 0.15. A similar code is used on WVII-AS to numerically calculate the stability of the current density radial profiles against tearing modes, and the predictions are compared with experimental observations. Again, the Δ'-analysis is in quantitative agreement with the experimental data, which are obtained over a wide range of current density profiles at different heating scenarios. In the later experiment, no threshold behavior of disruption free hybrid operation was identified. To some extent, control of the instabilities may be achieved by adjusting the external rotational transform, and hence the location of the relevant rational surface with respect to the current density profile.

These studies shed lights on the investigation of the effect of strong 3D shaping on density limit disruptions in CTH plasmas. With improved equilibrium reconstruction, better knowledge of the current density and safety factor q profiles is attainable, based on which we have applied similar 1-D Δ' calculation to CTH plasmas. A Fortran code is developed to solve the Euler equation (Eq. D.5) with current density and safety factor q profiles obtained from equilibrium

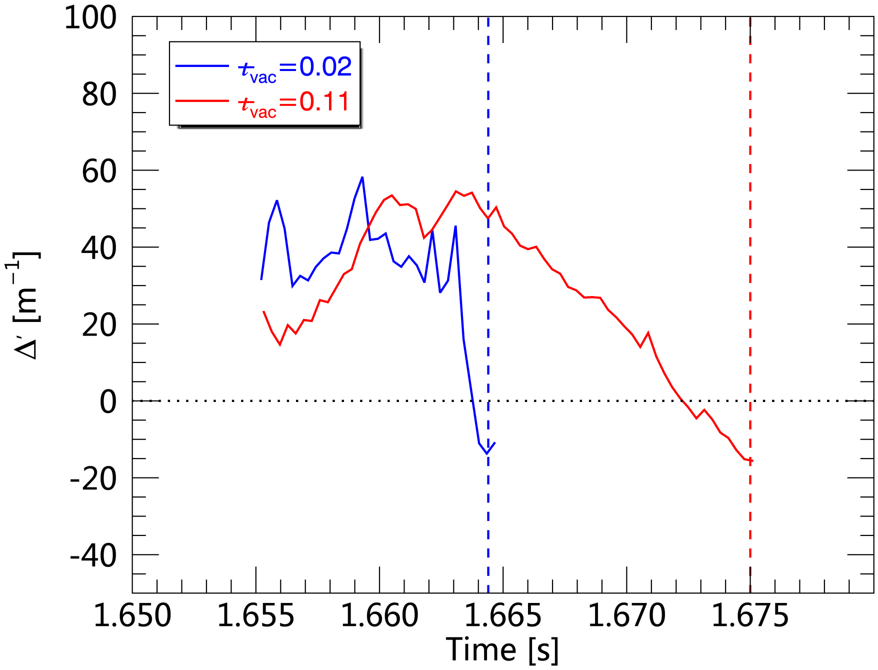

Figure 6.18: A comparison of the time evolution of the tearing mode stability parameter Δ' for two cases in Fig. 6.16. The blue and red dashed lines mark the timing when the two discharges disrupt. The black dotted line indicates the predicted stabilization boundary for Δ'.

reconstructions using both SXR and magnetic data. The value of Δ' is calculated for a given tearing mode, which is the $m/n = 2/1$ tearing mode in this case.

Taking the two discharges shown in Fig. 6.16 as examples, the time evolution of the Δ' before disruption is calculated and compared in Fig. 6.18. As mentioned before, the two discharges shown in blue and red have vacuum transform values at 0.02 and 0.11 respectively. The evolution of plasma current and density is similar up to the point where the blue shot (lower vacuum transform) disrupted early. The high vacuum transform discharge continued to evolve and disrupted later with a similar density but lower current. In Fig. 6.18, the blue and red dashed lines indicate when the two discharges disrupt, and the black dotted line indicates the predicted stabilization boundary for $\Delta' = 0$. For both of the two discharges, the value of Δ' decreases continuously as the current profile narrows approaching the disruption and crosses zero before disruption. Simultaneously, the $m/n = 2/1$ tearing mode grows, and plasma becomes more unstable until disruption occurs. At the time when the stability parameter Δ' of the low vacuum transform discharge goes negative, Δ' of the high vacuum transform plasma remains above zero. Stabilization provided by addition of external applied vacuum transform suppresses growth of tearing modes and the subsequent disruption. The discharge shown in red survived at similar current and density.

This calculation somehow provides qualitative analysis of the stability of $2/1$ tearing mode in CTH plasmas, giving that it represents a 1-D model of a 3-D plasma equilibrium. It supports the statement that interactions between the current profile shrinkage and internal tearing mode lead to density limits in CTH. While the cause of the current profile peaking, whether it is due to the cooling of the edge of the plasma, and/or increased turbulent transport, has not been investigated in this work. It also suggests that the suppression of density limit disruptions with additional vacuum transform is through profile control of the current density and safety factor.

That said, the Δ' calculation does not always successfully correlate with disruptions. For some cases, it was not able to predict the unstable regime when discharges approached disruptions. Two factors may affect the validate of the calculation. First, the whole derivation is based on a simple cylindrical geometric approach that neglects toroidal curvature and the elliptical plasma cross-section. However, CTHplasmas are not only toroidal, but fully 3D and highly non-axisymmetric. The simplified model might naturally not be able to capture the 3D physics inherent to CTH plasmas. Secondly, the current profile parametrization applied to reconstructions analysis in this thesis only depends on a single fitting parameter α, and may not be sufficient to describe the actual shape of the profile in some cases. Thus, the current distribution within the plasma may not be modeled with sufficient accuracy for all discharges. Further studies are needed to characterize the nature of the disruption onset relative to the current profile width.

6.5 Discussion and future work

Because the existence of density limits in toroidally confined plasmas has significant impacts on fusion programs around the world, extensive understanding of the physics behind the Greenwald limit, in particular, is of great importance. We have shown that the density-limiting behavior of CTH plasmas is qualitatively similar to that seen in tokamaks, and is consistent with the classic final scenario of the density limit: current profile shrinkage leads to growing MHD instabilities (usually $m/n = 1/2$ tearing mode) followed by loss of MHD equilibrium, and final disruptions. The hybrid plasmas of CTH also show a unique feature that increased external rotational transform leads to stable operation at densities above the Greenwald limit. While we do not yet have a full understanding of the increased density limit with increasing external transform, evidence provided by improved reconstructions of the plasma current profile by including SXR emissivity measurements in V3FIT suggest that the externally-applied transform largely has the effect of raising the net transform across the whole profile, and thus shifting the $q = 2$ surface outward relative to its position in tokamak discharges, reducing the current density gradient, resulting in a MHD stable regime.

Further investigation to utilize the Δ' calculation with improved knowledge of current density and safety factor q profiles confirms that density limit disruptions are associated with interactions between current profile peaking and growing internal tearing mode. It also suggests that the suppression of density limit disruptions with additional vacuum transform is through profile control of the current density and safety factor. However, the calculation fails to predict the unstable regimes in some of the disrupting discharges. We need either an advanced three-dimensional model to calculate the stability parameter Δ' or a better measure of the current density profile. Most likely the combination of the two is preferred.

In tokamaks, the Greenwald limit can be exceeded by imposing peaked density profiles with additional fueling in the core. There is evidence that the separation between densities from the central channel and the edge channel of the interferometer system increases with increasing external transform. To determine whether the increase in the density limit with vacuum transform is related to changes in the equilibrium plasma density profile as well as the underlying vacuum transform profile, better resolution in the density diagnostic is needed to resolve density profiles. As a result, the current three-channel interferometer is been upgrading with additional channels to give improved profile measurements.

The physics underlying the density limit in CTH plasmas may be ascribed to a global radiative instability, radiative instability localized to a specific rational surface, or enhanced transport near the plasma edge. With regard to the investigation of radiative behavior prior to a density limit disruption, two new bolometer cameras have been installed on CTH to measure the total radiated power. Initial line-integrated data from the multi-chorded bolometric arrays show evidence of coherent modulation of the radiated power prior to disruption. Further analysis such as tomographic reconstruction and calibrated data are needed before ascribing radiation to localized features. A new single point Thomson scattering system is under construction, which can be used to calibrate the two-color SXR camera system. Coupled with improved bolometric analysis, better knowledge of the evolution of radiation and temperature profile is attainable. Measurements of radiated power will also contribute to accession of radiative island instability criterion. A new Langmuir triple probe will be developed for the proposed island divertor to measure edge fluctuation spectra and levels of turbulence as the discharge approaches disruption. These measurements are supposed to give an indication of any systematic change in edge turbulence prior to disruption with changing external vacuum transform.

A better scientific understanding of the ubiquitous tokamak density limit would greatly benefit worldwide fusion programs. CTH is a unique platform which can vary the disruption criterion with its flexibility of vacuum field configurations. The studies of effects on MHD stability and disruption behavior of strong 3D shaping could facilitate future stellarators, specifically the quasi-axisymmetric stellarator. What is more, these studies provide an unusual linkage between 3D toroidal confinement physics and 3D helical geometric physics. Understanding the density limiting disrupting behavior of a hybrid stellarator would finally reduce scientific and operational uncertainties in a proposal for a future quasi-axisymmetric stellarator.

Chapter 7

Summary and future work

7.1 Summary

A key finding of this work is that diagnosing the internal magnetic structure of the hybrid plasma solely with measurements of the magnetic field external to the plasma is not useful as is generally fond in axisymmetric toroidal plasmas. Even in stellarator plasmas with typical geometries characterized by high elongation and non-axisymmetric 3D shaping, the variation of the magnetic field outside the plasma yields little of the details of the internal current profile. This finding is made particularly clear when we perform equilibrium reconstruction of sawtoothing plasmas in CTH using external magnetic diagnostics alone. The resulting reconstructed current profiles are broad, and the reconstructed central safety factors are away from one. These results contradict well accepted sawtooth theory, in which the sawtooth oscillation is driven by ohmic heating of the core plasma until the safety factor drops below one triggering the growth of an $m/n = 1/1$ kink-tearing mode.

Because there is no diagnostic tool to directly measure the internal poloidal magnetic field, we have developed two methods to incorporate multi-channel SXR measurements into the V3FIT code to improve the reconstruction of the internal plasma current distribution. Reconstruction of the current profile from knowledge of the inversion location of sawteeth in the radial brightness profile of the SXR emission is performed as a secondary optimization step in V3FIT, in which the inversion radius is identified as a flux surface found from the reconstruction performed with magnetics alone, and the current profile is then reconstructed again with the prior knowledge of $q = 1$ corresponding to a particular reconstructed flux surface.

In the second approach, measurements from eight SXR camera arrays at different toroidal and poloidal locations are used to reconstruct the geometry of flux surfaces (shape and centroids) and thus infer the current distribution within the plasma. The original approach of deriving the plasma current distribution from the geometric shape of the flux surfaces through consideration of the MHD equilibrium requirement was based on toroidally symmetric, non-circular cross-section configurations. We have shown that the concept remains valid and practical in a non-axisymmetric stellarator with significant plasma current.

Equilibrium reconstructions of sawtoothing plasmas using SXR and magnetic data predict the central safety factors to be around unity in agreement with reconstruction results in which external magnetic data was used in conjunction with the prior constraint of the location of the $q = 1$ surfaces extracted from SXR emissivity data. The technique described in this thesis provides an alternative method that can be used to measure the current distribution, 3D in our case, with reasonable accuracy as demonstrated.

Regarding the Greenwald density limit, we have shown that the density-limiting behavior of CTH plasmas is qualitatively similar to that seen in tokamaks, and is consistent with the current accepted scenario of the density limit: current profile shrinkage leads to growing MHD instabilities (usually $m/n = 2/1$ tearing mode), leading to destruction of nested magnetic flux surface, loss of plasma confinement, and final disruptions. Our investigation of the hybrid plasmas on CTH also show a unique feature that increased external rotational transform leads to stable operation at densities above the Greenwald limit. While we do not yet have a full understanding of the increase of the density limit with increasing external transform, evidence provided by improved reconstructions of the plasma current profile suggest that the externally-applied transform largely has the effect of raising the net transform across the whole profile, and thus shifting the $q = 2$ surface outward relative to its position in tokamak discharges, reducing the current density gradient, resulting a MHD stable regime. Further investigation to utilize Δ' calculation with improved knowledge of current density and safety factor q profiles confirms that density limit disruptions are associated with interactions between current profile peaking and growing internal tearing mode. It also suggests that the suppression of density limit disruptions with additional vacuum transform is through profile control of the current density and safety factor. However, the calculation fails to predict the unstable regimes in some of the disrupting discharges. We need either a more advanced three-dimensional tearing mode model to calculate the stability parameter Δ' or a better measure of the current density profile. Most likely, the combination of the two is necessary.

7.2 Future work

A better scientific understanding of the ubiquitous tokamak density limit would greatly benefit worldwide fusion programs. CTH is a unique platform which can vary the disruption criterion with its flexibility of vacuum field configurations. The studies of effects on MHD stability and disruption behavior of strong 3D shaping could facilitate future stellarators, specifically the quasi-axisymmetric stellarator. What is more, these studies provide an unusual linkage between 3D toroidal confinement physics and 3D helical geometric physics.

Further investigation of the stability criteria of the density limit discharges in CTH requires reliable and accurate knowledge of the internal current density profile. The SXR camera suit has been proven to be the most powerful diagnostic tool in determine the current distribution within the plasma. Since currently there is only one SXR camera in the full period of CTH, we would like to install more to extend the 3D equilibrium reconstruction of CTH plasmas. An increase of the resolution of the current SXR cameras is also preferred.

The physics underlying the density limit in CTH plasmas may be ascribed to a global radiative instability, radiative instability localized to specific rational surface, or enhanced transport near the plasma edge. With regard to the investigation of radiative behavior prior to a density limit disruption, two new bolometer cameras have been installed on CTH to measure the total radiated power. Initial line-integrated data from the multi-chorded bolometric arrays show evidence of coherent modulation of the radiated power prior to disruption. Further analysis such as tomographic reconstruction and calibrated data are needed before ascribing radiation to localized features. A new single point Thomson scattering system is under construction, which can be used to calibrate the two-color SXR camera system. Coupled with improved bolometric analysis, better knowledge of the evolution of radiation and temperature profile is attainable. Measurements of radiated power will also contribute to accession of radiative island instability criterion. A new Langmuir triple probe will be developed for the proposed island divertor to measure edge fluctuation spectra and levels of turbulence as the the discharge approaches disruption. These measurements are supposed to give an indication of any systematic change in edge turbulence prior to disruption with changing external vacuum transform.

In tokamaks, the Greenwald limit can be exceeded by imposing peaked density profile with additional fueling in the core. There is evidence that the separation between densities from the central channel and the edge channel of the interferometer system increases with increasing external transform. To determine whether the increase in the density limit with vacuum transform is related to changes in the equilibrium plasma density profile as well as the underlying vacuum transform profile, better resolution in the density diagnostic is needed to resolve density profiles. As a result, the current three-channel interferometer is been upgrading with additional channels to give improved profile measurements.

Appendices

Appendix A

V3FIT data and configuration files

To perform a equilibrium reconstruction, V3FIT requires various inputs, including profile modeling in the VMEC equilibrium, VMEC and V3FIT execution inputs, geometric information and experimental data of all diagnostics, etc. There inputs are stored in formatted text files, which are called by reconstruction execution programs, such as the Reconstruction Shot Runner and Batch Runner in Appendix. B. The major two input files is the V3FIT data file that contains all diagnostic information, and the V3FIT configuration file that contains VMEC and V3FIT execution settings. This appendix gives a brief description of these input files and their stored places.

V3FIT data file This input file defines all variables used in VMEC and V3FIT and loads corresponding values from the tree. These variables include various currents from extern coils, vacuum vessel, helical coil frames and plasma, and all diagnostic channels including magnetic diagnostics, interferometer system and soft-x ray cameras. It loads both geometric information and experimental data from all diagnostics in order.

Path: `Z:\_Users\Ma\Public\V3FIT_data_config_files\ALL_Mag_SXR_Bol_decon.v3Data`

V3FIT configuration file

This input file contains all configuration settings for VMEC and V3FIT code. VMEC configurations include initialization of the current and pressure profiles and VMEC execution parameters. V3FIT configurations include V3FIT execution parameters, diagnostic signal setting, reconstructed signal setting, etc. A LabVIEW program, 'Reconstruction Config.vi' at `Z:\LabView\UserPrograms\ReconstructionShotRunner\v3fit`, is written to create and edit the V3FIT configuration file.
Path: `Z:\_Users\Ma\Public\V3FIT_data_config_files\all_mag_sxr_bol_decon.v3config`

LIST file for all magnetic diagnostics

This file is called by the V3FIT data file. It is a list of all magnetic diagnostic '.nc' files in the same folder. These formatted files contain geometric information of magnetic diagnostics and response functions between magnetic diagnostics and various current sources.
Path: `/home/inst/xzm0005/recon/diagnostics/All/V3/diagnostic.all_mdsig.LIST`

CTH diagnostic file

This file contains the geometric information of all magnetic diagnostics in Cartesian coordinates.
Path: `/home/inst/xzm0005/recon/diagnostics/All/V3/diagnostic.all`

SXR chord file This file is called by the V3FIT data file. It contain the geometric information of all SXR camera chords in cylindrical coordinates.
Path: `/home/inst/jlh0029/pub/SC_ALL_July_2016_decon.txt`

Interferometer chord file

This file is called by the V3FIT data file. It contain the geometric information of three channels of the interferometer system.

Path: `/home/hartwgj/pub/ipch.cth_3ch`

Coils_dot file for CTH magnetic coils

This file contains the Cartesian coordinates for all the magnet coils on CTH, including HF coil, TVF coil, SVF coil, TF coil, RF coil and OH coil. It also contains the geometric model for the vacuum vessel and helical coil frames. This file along with the CTJ diagnostics file mentioned above is used to compute the mutual inductances or response functions between magnetic diagnostics and the CTH magnet coils.

Path: `/home/v3fit/public/input_files/mgrid/mgrid_cth.18b.mo.f5sa_ec6a.nc`

Appendix B

Reconstruction shot runner and batch runner

VMEC and V3FIT code execution environment is installed in a remote server with Linux system. Two user-friendly, LabVIEW based graphical user interfaces are developed to communicate with the remote server and perform equilibrium reconstructions. The two programs can run on different platforms including PCs and Macs. A brief description of the two programs, 'Reconstruction Shot Runner' and 'Reconstruction Batch Runner', and related input file is given in this appendix.

Reconstruction Shot Runner

This program is designed to perform serious reconstructions of a single discharge. The user interface is shown in Fig. B.1 To perform equilibrium reconstructions, the shot runner requires the shot number, time range and time interval. Then using V3FIT data file and configuration file, the shot runner loads all related plasma parameters and models, all diagnostic measurements and geometric models, and all VMEC and V3FIT execution parameters.

Path: `Z:\LabView\UserPrograms\ReconstructionShotRunner\Windows\ReconstructionShotRunner`

Reconstruction Batch Runner

The Reconstruction Batch Runner is a separate program that enable reconstructing a list of discharges at specific time slices. The user interface is shown in Fig. B. The batch Runner utilizes a shot list file to perform equi-

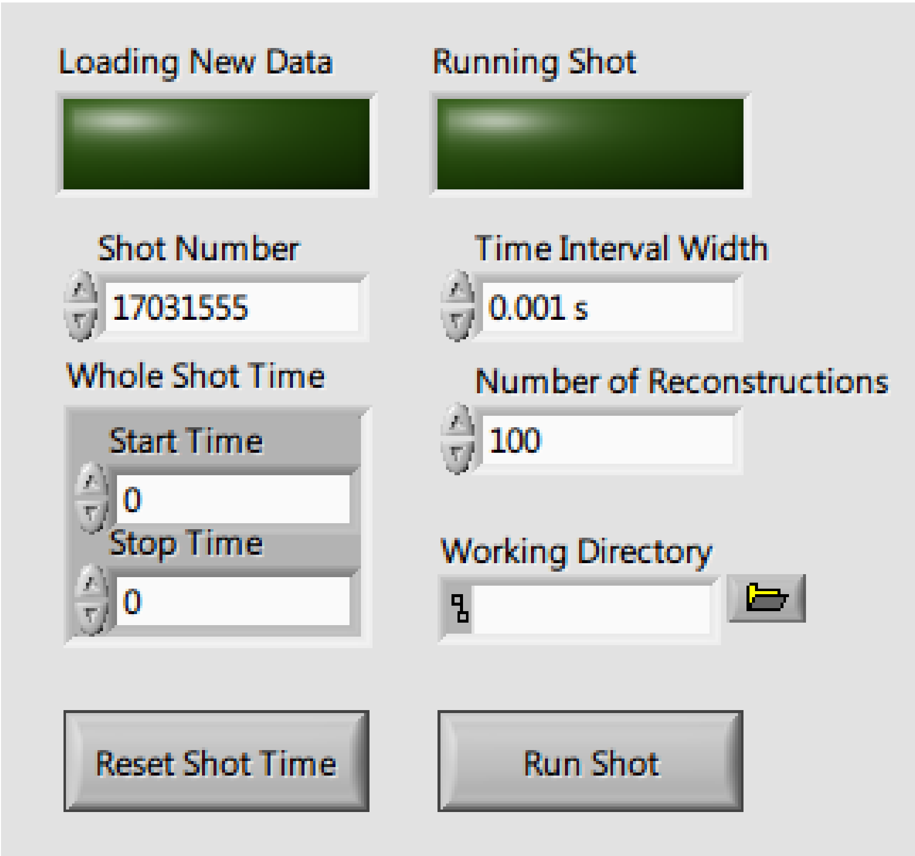

Figure B.1: User interface of Reconstruction Shot Runner

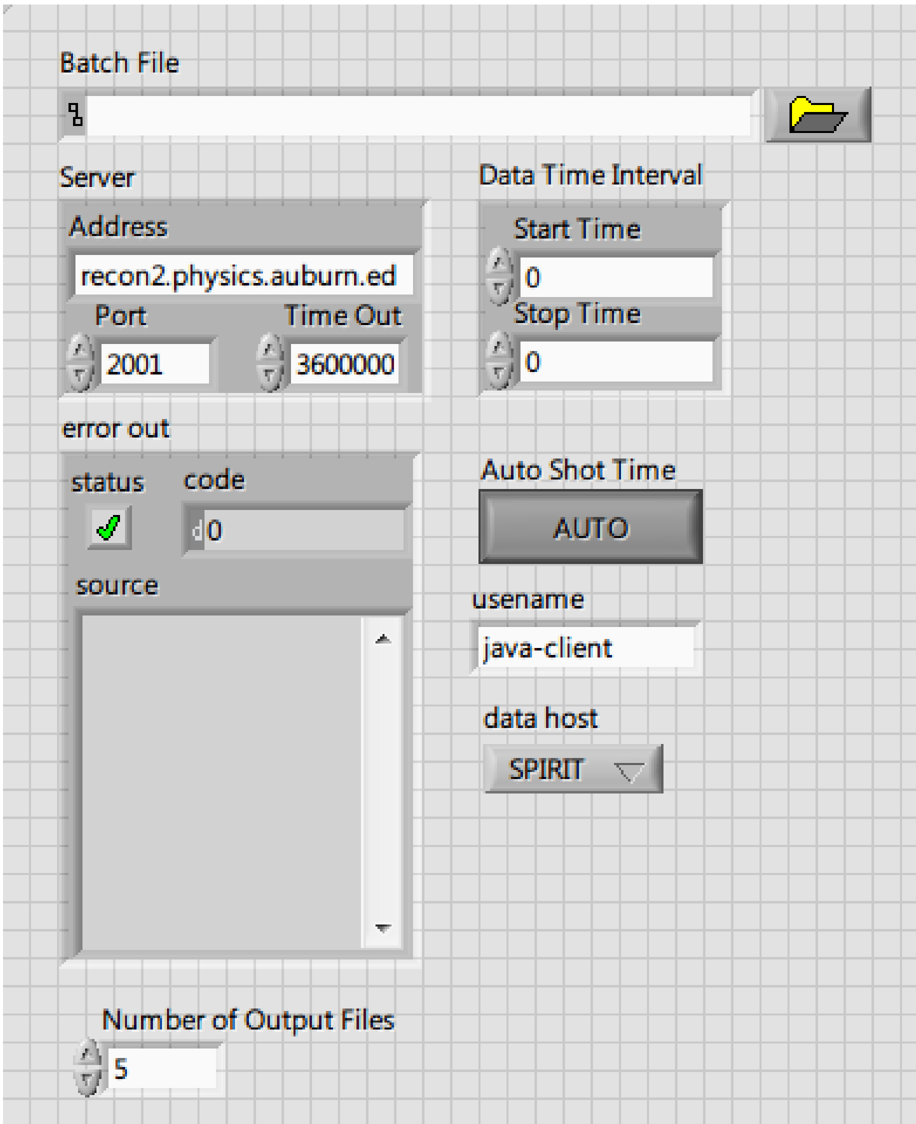

Figure B.2: User interface of Reconstruction Shot Runner librium reconstructions of any number of discharges at any number of time slices.

Path: `Z:\LabView\UserPrograms\ReconstructionShotRunner\v3fit\ReconstructionBatchRunner`

CTH shot list file

The shot list file is called by the batch runner to perform serious reconstructions of a list of discharges at specific time slices. It also includes the paths of the V3FIT data file and configuration file.

Path: `Z:\_Users\Ma\Public\CTH_shot_list_file\example.cthsl`

Appendix C

Parameter uncertainty and signal effectiveness

C.1 Parameter uncertainty

Knowing the uncertainties in the reconstructed parameters is important to evaluate how effective the reconstruction is in determining these parameters with the given set of diagnostic signals. In other words, the uncertainties in the reconstructed parameters provide an additional indication of the confidence of the reconstructed parameters, along with the minimized χ^2 value.

In V3FIT, observed signals are assumed to be uncorrelated and have a Gaussian noise distribution. A signal covariance matrix, $\boldsymbol{C}^{\text{Signal}}$, is defined as:

$$\boldsymbol{C}^{\text{Signal}} = \sigma_i \sigma_j \delta_{ij} \,. \tag{C.1}$$

The Jacobian in Eq.3.1 maps the signal space to parameter space, thus the uncertainties in parameter space can be calculated from the uncertainties in signal space as:

$$\left(\boldsymbol{C}^{\text{Param}}\right)^{-1} = \boldsymbol{J}^{\text{T}} \left(\boldsymbol{C}^{\text{Signal}}\right)^{-1} \boldsymbol{J} \,. \tag{C.2}$$

Since the signal covariance matrix is diagonal its inverse is merely the reciprocal of the diagonal elements. Then the parameter uncertainties are obtained from the square root of the diagonal elements of the inverted parameter covariance matrix. Using these uncertainties, the off-diagonal terms of the parameter covariance matrix may be normalized into a correlation matrix.

With the parameter covariance matrix known, the uncertainty and correlations of parameters can be propagated to the modeled signals. If we define another Jacobian of the mode,

$$\boldsymbol{K} = \frac{\partial M(\boldsymbol{p})}{\partial p_i}\,, \tag{C.3}$$

then the model covariance matrix can be calculated as:

$$\left(\boldsymbol{C}^{\text{Model}}\right)^{-1} = \boldsymbol{K}\left(\boldsymbol{C}^{\text{Param}}\right)\boldsymbol{K}^{\text{T}}\,. \tag{C.4}$$

Similarly, the uncertainties of modeled signals are taken from the square root of the diagonal of the model covariance matrix.

C.2 Signal effectiveness

In order to make effective use of equilibrium reconstruction, it is important to understand the sensitivity of parameters to the diagnostic signals. To quantify this, V3FIT defines the signal effectiveness as:

$$R_{ij} = \frac{\sigma_i}{\sigma_j^P}\frac{\partial \sigma_j^P}{\partial \sigma_i} \tag{C.5}$$

where σ_j^P is taken from the diagonal of the parameter covariance matrix $\boldsymbol{C}^{\text{Param}}$. R_{ij} is a dimensionless, normalized ratio of the fractional reduction in the reconstructed parameter variance to the fractional reduction in the signal variance. It essentially tells how effective a specific diagnostic is in determining a particular plasma parameter.

Signal effectiveness defined in this way can be useful in deciding the optimized positions to install diagnostics, or what diagnostics are needed and in what locations are best to improve the measurement of a certain plasma parameter. Signal effectiveness calculation has been applied to the design and installation of new saddle coils in CTH, details of which will be discussed in the following chapter. It has also been used to explain why SXR emissivity measurements can more effectively reconstruct the current density profile than measurements from external magnetic diagnostics.

Appendix D

Stabilization of MHD instabilities

The computation of stability diagrams is carried out in a cylindrical current-carrying stellarator with circular cross section. By using stellarator expansion and low-β ordering, the free energy integral of the system[149] is given by:

$$W = \frac{4\pi^2}{k} \int_0^b r dr \left[\left(\frac{d\psi}{dr} \right)^2 + \frac{\alpha}{r^2} \psi^2 \right] , \tag{D.1}$$

where

$$\begin{aligned} \psi &= \frac{krB_0}{2\pi} \upsilon \xi \\ \upsilon &= -\frac{n}{m} + \iota^p(r) + \iota^{vac}(r) = -\frac{n}{m} + \iota(r) \\ \alpha &= m^2 + \frac{1}{r\upsilon} \frac{d}{dr} \left(r^3 \frac{d\iota^\sigma}{dr} \right) . \end{aligned} \tag{D.2}$$

Here, b and a is the wall radius and the plasma radius respectively. ψ represents the potential of magnetic field with ξ denoting a small perturbation of the plasma. The total rotational transform, ι, is a sum of the rotational transform due to the plasma current, ι^p, and the rotational transform due to the vacuum external helical field, ι^{vac}. In a tokamak, the later term vanishes. m and n are poloidal and toroidal mode number respectively. It is assumed that the current density vanishes at the plasma surfaces and the region from $r = a$ to $r = b$ is vacuum.

From Eq. D.1, the perturbation δW resulting from small perturbed $\delta \upsilon$ is given by

$$\delta W = -\frac{4\pi^2}{k} \int_0^b r dr \left[\left(\frac{d\psi}{dr} \right)^2 + \frac{m^2}{r^2} \psi^2 \left(\frac{m/r}{m\iota(r) - n} \right) \frac{a}{B_0} \frac{dj}{dr} \psi^2 \right] \delta(\upsilon^2) . \tag{D.3}$$

Here we use the approximation:

$$ \iota^{\sigma}(r) = \frac{aB_\theta}{rB_0} = \frac{4\pi a}{kr^2 B_0} \int J_r dr \,. \tag{D.4} $$

Then the Euler equation of free energy integral is:

$$ \frac{1}{r}\frac{d}{dr}\left(r\frac{d\psi}{dr}\right) - \frac{m^2}{r^2}\psi - \left(\frac{m/r}{m\iota(r) - n}\right)\frac{a}{B_0}\frac{dj}{dr}\psi = 0 \,. \tag{D.5} $$

The stability parameter, Δ', is calculated using the solution of $\psi(r)$ from Eq. D.5 as:

$$ \Delta'(w) = \frac{1}{\psi(r_s)}\left[\frac{d\psi(r_s+\epsilon)}{dr} - \frac{d\psi(r_s-\epsilon)}{dr}\right]_{\epsilon\to 0} \,. \tag{D.6} $$

Here r_s is the radius of the resonant magnetic surface where $\iota(r_s) = n/m$. It can been seen that Δ' depends on the external rotational transform ι^{vac} and rotational transform ι^{p} due to plasma current, or equivalently the current density profile. By integrating Eq. D.5, it can be shown that Δ' is proportional to δW of Eq. D.3. This means that the mode is unstable as long as $\Delta' < 0$ or $\delta W > 0$.

References

[1] Donald A. Spong. 3d toroidal physics: Testing the boundaries of symmetry breaking. *Physics of Plasmas*, 22(5):055602, 2015.

[2] H.-S. Bosch and G.M. Hale. Improved formulas for fusion cross-sections and thermal reactivities. *Nuclear Fusion*, 32(4):611, 1992.

[3] John Wesson and D. J. Campbell. *Tokamaks*, volume p.749. Clarendon Press, 2004.

[4] Martin Greenwald. Density limits in toroidal plasmas. *Plasma Physics and Controlled Fusion*, 44(8):R27, 2002.

[5] J. Freidberg. *Ideal MHD*. Cambridge University Press, 2014.

[6] K. Ikeda. Progress in the iter physics basis. *Nuclear Fusion*, 47(6), 2007.

[7] H. Ikezi, K. F. Schwarzenegger, and C. Ludescher. Semi-stellarator field stabilization of tokamak plasma. *The Physics of Fluids*, 22(10):2009–2013, 1979.

[8] W 7-A Team. Stabilization of the (2, 1) tearing mode and of the current disruption in the w7-a stellarator. *Nuclear Fusion*, 20(9):1093, 1980.

[9] M Hirsch, J Baldzuhn, C Beidler, R Brakel, R Burhenn, A Dinklage, H Ehmler, M Endler, V Erckmann, Y Feng, J Geiger, L Giannone, G Grieger, P Grigull, H-J Hartfu, D Hartmann, R Jaenicke, R Knig, H P Laqua, H Maaberg, K McCormick, F Sardei, E Speth, U Stroth, F Wagner, A Weller, A Werner, H Wobig, S Zoletnik, and for the W7-AS Team. Major results from the stellarator wendelstein 7-as. *Plasma Physics and Controlled Fusion*, 50(5):053001, 2008.

[10] O. Motojima, H. Yamada, A. Komori, N. Ohyabu, K. Kawahata, O. Kaneko, S. Masuzaki, A. Ejiri, M. Emoto, H. Funaba, M. Goto, K. Ida, H. Idei, S. Inagaki, N. Inoue, S. Kado, S. Kubo, R. Kumazawa, T. Minami, J. Miyazawa, T. Morisaki, S. Morita, S. Murakami, S. Muto, T. Mutoh, Y. Nagayama, Y. Nakamura, H. Nakanishi, K. Narihara, K. Nishimura, N. Noda, T. Kobuchi, S. Ohdachi, Y. Oka, M. Osakabe, T. Ozaki, B. J. Peterson, A. Sagara, S. Sakakibara, R. Sakamoto, H. Sasao, M. Sasao, K. Sato, M. Sato, T. Seki, T. Shimozuma, M. Shoji, H. Suzuki, Y. Takeiri, K. Tanaka, K. Toi, T. Tokuzawa, K. Tsumori, K. Tsuzuki, I. Yamada, S. Yamaguchi, M. Yokoyama, K. Y. Watanabe, T. Watari, Y. Hamada, K. Matsuoka, K. Murai, K. Ohkubo, I. Ohtake, M. Okamoto, S. Satoh, T. Satow, S. Sudo, S. Tanahashi, K. Yamazaki, M. Fujiwara, and A. Iiyoshi. Initial physics achievements of large helical device experiments. *Physics of Plasmas*, 6(5):1843–1850, 1999.

[11] A. Komori, H. Yamada, O. Kaneko, and et al. Development of net-current free heliotron plasmas in the large helical device. In *22nd IAEA Fusion Energy Conference*, Geneva, 2008.

[12] M C Zarnstorff, L A Berry, A Brooks, E Fredrickson, G-Y Fu, S Hirshman, S Hudson, L-P Ku, E Lazarus, D Mikkelsen, D Monticello, G H Neilson, N Pomphrey, A Reiman, D Spong, D Strickler, A Boozer, W A Cooper, R Goldston, R Hatcher, M Isaev, C Kessel, J Lewandowski, J F Lyon, P Merkel, H Mynick, B E Nelson, C Nuehrenberg, M Redi, W Reiersen, P Rutherford, R Sanchez, J Schmidt, and R B White. Physics of the compact advanced stellarator ncsx. *Plasma Physics and Controlled Fusion*, 43(12A):A237, 2001.

[13] J. M. Canik, D. T. Anderson, F. S. B. Anderson, C. Clark, K. M. Likin, J. N. Talmadge, and K. Zhai. Reduced particle and heat transport with quasisymmetry in the helically symmetric experiment. *Physics of Plasmas*, 14(5):056107, 2007.

[14] M. Okabayashi, J. Bialek, A. Bondeson, M.S. Chance, M.S. Chu, A.M. Garofalo, R. Hatcher, Y. In, G.L. Jackson, R.J. Jayakumar, T.H. Jensen, O. Katsuro-Hopkins, R.J. La Haye, Y.Q. Liu, G.A. Navratil, H. Reimerdes, J.T. Scoville, E.J. Strait,

M. Takechi, A.D. Turnbull, P. Gohil, J.S. Kim, M.A. Makowski, J. Manickam, and J. Menard. Control of the resistive wall mode with internal coils in the diiid tokamak. *Nuclear Fusion*, 45(12):1715, 2005.

[15] S.A. Sabbagh, J.W. Berkery, R.E. Bell, J.M. Bialek, S.P. Gerhardt, J.E. Menard, R. Betti, D.A. Gates, B. Hu, O.N. Katsuro-Hopkins, B.P. LeBlanc, F.M. Levinton, J. Manickam, K. Tritz, and H. Yuh. Advances in global mhd mode stabilization research on nstx. *Nuclear Fusion*, 50(2):025020, 2010.

[16] T.E. Evans, R.A. Moyer, J.G. Watkins, T.H. Osborne, P.R. Thomas, M. Becoulet, J.A. Boedo, E.J. Doyle, M.E. Fenstermacher, K.H. Finken, R.J. Groebner, M. Groth, J.H. Harris, G.L. Jackson, R.J. La Haye, C.J. Lasnier, S. Masuzaki, N. Ohyabu, D.G. Pretty, H. Reimerdes, T.L. Rhodes, D.L. Rudakov, M.J. Schaffer, M.R. Wade, G. Wang, W.P. West, and L. Zeng. Suppression of large edge localized modes with edge resonant magnetic fields in high confinement diii-d plasmas. *Nuclear Fusion*, 45(7):595, 2005.

[17] Y Liang, H R Koslowski, P R Thomas, E Nardon, S Jachmich, B Alper, P Andrew, Y Andrew, G Arnoux, Y Baranov, M Bcoulet, M Beurskens, T Biewer, M Bigi, K Crombe, E De La Luna, P de Vries, T Eich, H G Esser, W Fundamenski, S Gerasimov, C Giroud, M P Gryaznevich, D Harting, N Hawkes, S Hotchin, D Howell, A Huber, M Jakubowski, V Kiptily, A Kreter, L Moreira, V Parail, S D Pinches, E Rachlew, O Schmitz, O Zimmermann, and JET-EFDA Contributors. Active control of type-i edge localized modes on jet. *Plasma Physics and Controlled Fusion*, 49(12B):B581, 2007.

[18] Allen H Boozer. Stellarators and the path from iter to demo. *Plasma Physics and Controlled Fusion*, 50(12):124005, 2008.

[19] Allen H. Boozer. Use of nonaxisymmetric shaping in magnetic fusion. *Physics of Plasmas*, 16(5):058102, 2009.

[20] J. D. Hanson, S. F. Knowlton, B. A. Stevenson, and G. J. Hartwell. Equilibrium and stability of current-carrying discharges in the non-axisymmetric cth experiment. *Contributions to Plasma Physics*, 50(8):724–730, 2010.

[21] James D.Hanson, Steven P. Hirshman, Stephen F. Knowlton, Lang L. Lao, Edward A. lazarus, and John M. Shields. V3fit: A code for three-dimensional equilibrium reconstruction. *Nuclear Fusion*, 49(7):186–208, 2009.

[22] F C Schuller. Disruptions in tokamaks. *Plasma Physics and Controlled Fusion*, 37(11A):A135, 1995.

[23] M. Greenwald, J.L. Terry, S.M. Wolfe, S. Ejima, M.G. Bell, S.M. Kaye, and G.H. Neilson. A new look at density limits in tokamaks. *Nuclear Fusion*, 28(12):2199, 1988.

[24] Benjamin A. Stevenson. *3D Reconstruction of Plasma Equilibria using Magnetic Diagnostics on the Compact Toroidal Hybridtitle*. PhD thesis, Auburn University, 2011.

[25] F.S.B. Anderson, A.F. Almagri, D.T. Anderson, P.G. Matthews, J.N. Talmadge, and J.L. Shohet. Helically symmetric experiment, (hsx) goals, design and status. *Fusion Techology*, 27(6), 1995.

[26] B.E. Nelson, L.A. Berry, A.B. Brooks, M.J. Cole, J.C. Chrzanowski, H.-M. Fan, P.J. Fogarty, P.L. Goranson, P.J. Heitzenroeder, S.P. Hirshman, G.H. Jones, J.F. Lyon, G.H. Neilson, W.T. Reiersen, D.J. Strickler, and D.E. Williamson. Design of the national compact stellarator experiment (ncsx). *Fusion Engineering and Design*, 66:169 – 174, 2003. 22nd Symposium on Fusion Technology.

[27] V. Bykov, F. Schauer, K. Egorov, A. Tereshchenko, P. van Eeten, A. Dbner, M. Sochor, D. Zacharias, A. Dudek, W. Chen, P. Czarkowski, L. Sonnerup, J. Fellinger, D. Hathiramani, M.Y. Ye, and W. Dnner. Structural analysis of w7-x: Overview. *Fusion Engineering and Design*, 84(2):215 – 219, 2009. Proceeding of the 25th Symposium on Fusion Technology.

[28] Stephen F. Knowlton James D. Hanson R.F. Kelly C. Montgomery Joshua T. Peterson, Greg J. Hartwell. Initial vacuum magnetic field mapping in the compact toroidal hybrid. *Journal of Fusion Energy*, 2007.

[29] Joshua T. Peterson. *VACUUM MAGNETIC FLUX SURFACE MEASUREMENTS MADE ON THE COMPACT TOROIDAL HYBRID*. PhD thesis, Auburn University, 2008.

[30] J.D. Hanson and J.R. Cary. Elimination of stochasticity in stellarators. *Plasma Physics and Fusion Techology*, 15(05), 1983.

[31] I. H. Hutchinson. *Principles of plasma diagnostics*. Cambridge, 2002.

[32] T. Equipe. Tokamak plasma diagnostics. *Nuclear Fusion*, 18(5):647, 1978.

[33] E. J. Strait. Magnetic diagnostic system of the diii-d tokamak. *Review of Scientific Instruments*, 77(2), 2006.

[34] M. C. ArchMiller, M. R. Cianciosa, D. A. Ennis, J. D. Hanson, G. J. Hartwell, J. D. Hebert, J. L. Herfindal, S. F. Knowlton, X. Ma, D. A. Maurer, M. D. Pandya, and P. Traverso. Suppression of vertical instability in elongated current-carrying plasmas by applying stellarator rotational transform. *Physics of Plasmas*, 21(5):056113, 2014.

[35] M. D. Pandya, M. C. ArchMiller, M. R. Cianciosa, D. A. Ennis, J. D. Hanson, G. J. Hartwell, J. D. Hebert, J. L. Herfindal, S. F. Knowlton, X. Ma, S. Massidda, D. A. Maurer, N. A. Roberds, and P. J. Traverso. Low edge safety factor operation and passive disruption avoidance in current carrying plasmas by the addition of stellarator rotational transform. *Physics of Plasmas*, 22(11):110702, 2015.

[36] X. Ma, D. A. Maurer, S. F. Knowlton, M. C. ArchMiller, M. R. Cianciosa, D. A. Ennis, J. D. Hanson, G. J. Hartwell, J. D. Hebert, J. L. Herfindal, M. D. Pandya, N. A. Roberds, and P. J. Traverso. Non-axisymmetric equilibrium reconstruction of a current-carrying stellarator using external magnetic and soft x-ray inversion radius measurements. *Physics of Plasmas*, 22(12), 2015.

[37] J.L. Herfindal, J.D. Dawson, D.A. Ennis, G.J. Hartwell, S.D.Loch, and D.A. Maurer. Design and initial operation of a two-color soft x-ray camera system on the compact toroidal hybrid experiment. *Review of Science Instrument*, 85(11), 2014.

[38] Jeffrey Lloyd Herfindal. *Control of Sawtooth Oscillation Dynamics using Externally Applied Stellarator Transform*. PhD thesis, Auburn University, 2016.

[39] M. C. Miller, J. D. Hanson, G. J. Hartwell, S. F. Knowlton, D. A. Maurer, and B. A. Stevenson. Design and implementation of a multichannel millimeter wave interferometer for the compact toroidal hybrid experiment. *Review of Scientific Instruments*, 83(10):–, 2012.

[40] L.L. Lao, H. St. John, R.D. Stambaugh, A.G. Kellman, and W. Pfeiffer. Reconstruction of current profile parameters and plasma shapes in tokamaks. *Nuclear Fusion*, 25(11):1611, 1985.

[41] J.k. Anderson, C.B. Forest, T.M. Biewer, J.S. Sarff, and J.C. Wright. Equilibrium reconstruction in the madison symmetric torus reversed field pinch. *NUCLEAR FUSION*, 44(1):162–171, 2004.

[42] L.L. Lao, J.R. Ferron, R.J. Groebner, W. Howl, H. St. John, E.J. Strait, and T.S. Taylor. Equilibrium analysis of current profiles in tokamaks. *Nuclear Fusion*, 30(6):1035, 1990.

[43] S.A. Sabbagh, S.M. Kaye, J. Menard, F. Paoletti, R.E. Bell M. Bell, and J.M. Bialek. Equilibrium properties of spherical torus plasmas in nstx. *Nuclear Fusion*, 41(11):1601, 2001.

[44] M. Brix, N.C. Hawkes, A. Boboc, V. Drozdov, S.E. Sharapov, and et al. Accuracy of efit equilibrium reconstruction with internal diagnostic information at jet. *Review of Scientific Instruments*, 79(10), 2008.

[45] L.E. Zakharov, J. Lewandowski, E.L. Foley, F.M. Levinton, H.Y. Yuh, V. Drozdov, and D.C. MacDonald. The theory of variances in equilibrium reconstruction. *Physics of Plasmas*, 15(9), 2008.

[46] J.D. Hanson, D.T. Anderson, M. Cianciosa, P. Franz, J.H. Harris, G.H. Hartwell, S.P. Hirshman, S.F. Knowlton, L.L. Lao, E.A. Lazarus, L. Marrelli, D.A. Maurer, J.C.

Schmitt, A.C. Sontag, B.A. Stevenson, and D. Terranova. Non-axisymmetric equilibrium reconstruction for stellarators, reversed field pinches and tokamaks. *Nuclear Fusion*, 53(8):083016, 2013.

[47] J. C. Schmitt, J. N. Talmadge, D. T. Anderson, and J. D. Hanson. Modeling, measurement, and 3-d equilibrium reconstruction of the bootstrap current in the helically symmetric experiment. *Physics of Plasmas*, 21(9):–, 2014.

[48] D. Terranova, D. Bonfiglio, and et al. A 3d approach to equilibrium, stability and transport studies in rfx-mod improved regimes. *Plasma Physics and Controlled Fusion*, 52(12), 2010.

[49] S. Lazerson, N. Pablant, D. Gates, H. Neilson, and et al. 3d equilibrium reconstruction in stellarators and tokamaks with stellopt. *Bulletin of the American Physical Society*, 57, 2012.

[50] J. Geiger, M. Endler, and A. Werner. Magnetic diagnostics for equiibrium reconstruction at w7-x. *Contributions to Plasma Physics*, 50(8):736–740, 2010.

[51] A. Reiman, L. Ku, D. Monticello, S. Hirshman, S. Hudson, C. Kessel, E. Lazarus, D. Mikkelsen, M. Zarnstorff, L. A. Berry, A. Boozer, A. Brooks, W. A. Cooper, M. Drevlak, E. Fredrickson, G. Fu, R. Goldston, R. Hatcher, M. Isaev, C. Jun, S. Knowlton, J. Lewandowski, Z. Lin, J. F. Lyon, P. Merkel, M. Mikhailov, W. Miner, H. Mynick, G. Neilson, B. E. Nelson, C. Nhrenberg, N. Pomphrey, M. Redi, W. Reiersen, P. Rutherford, R. Sanchez, J. Schmidt, D. Spong, D. Strickler, A. Subbotin, P. Valanju, and R. White. Recent advances in the design of quasiaxisymmetric stellarator plasma configurations. *Physics of Plasmas*, 8(5):2083–2094, 2001.

[52] S.P. Hirshman and W.I. van RIJ. Three-dimensinal free boundary calculations using a spectral green‘s function method. *Computer Physics Communications*, 43(1):143–155, 1986.

[53] S.P. Hirshman and D.K. Lee. Momcon: a spectral code for obtaining three-dimensional magnetohydrodynamic equilibria. *Computer Physics Communications*, 39(2):161–172, 1986.

[54] S. Tsaun and Hogun Jhang. Real-time plasma boundary reconstruction in the kstar tokamak using finite element method. *Fusion*, 82:163–174, 2007.

[55] R. Yoshino. Plasma control experiments in jt-60u. *Proceedings of the 36th IEEE Conference on Decision and Control*, pages 3709–3714, 1997.

[56] S. Cauffman and R. Majeski. Ion cyclotron emission on the tokamak fusion test reactor. *Review of Science Instrument*, 66:817, 1995.

[57] B J Braams. The interpretation of tokamak magnetic diagnostics. *Plasma Physics and Controlled Fusion*, 33(7):715, 1991.

[58] E. J. Strait, E. D. Fredrickson, J. M. Moret, and M. Takechi. Magnetic diagnostics. *Fusion Science and Technology*, 53(2):304–334, 2008.

[59] James Bialek, Allen H. Boozer, M. E. Mauel, and G. A. Navratil. Modeling of active control of external magnetohydrodynamic instabilities. *Physics of Plasmas*, 8(5):2170–2180, 2001.

[60] A. Zolfaghari, A. Brooks, A. Michaels, J. Hanson, and G. Hartwell. Calculation of eddy currents in the cth vacuum vessel and coil frame for use in mhd equilibrium reconstruction of the plasma discharge. *Fusion Science and Technology*, 64(3):498–501, September 2013.

[61] Keiichi Sakurai and Shyugo Tanahashi. Positional stability of a current-carrying plasma in an l=2 stellarator field. *Journal of the Physical Society of Japan*, 49(2):759–762, 1980.

[62] P. J. Traverso, D. A. Maurer, D. A. Ennis, G. J. Hartwell, M. M. Goforth, S. D. Loch, A. J. Pearce, and M. R. Cianciosa. Thomson scattering diagnostic system design for the compact toroidal hybrid experimenta). *Review of Scientific Instruments*, 85(11):–, 2014.

[63] P.Holmes, J.L. Lumley, and G.Berkooz. *Turbuence, Coherent structures, dynamical system and symmetry*. Cambridge University Press, 1996.

[64] I.H. Hutchinson R.S. Granetz and D.O. Overskei. Disruptive mhd activity during plasma current rise in alcator a tokamak. *Nuclear Fusion*, 19(12):1587, 1979.

[65] J.L. Luxon and B.B. Brown. Magnetic analysis of non-circular cross-section tokamaks. *Nuclear Fusion*, 22(6):813, 1982.

[66] L.L. Lao, H. St. John, R.D. Stambaugh, and W. Pfeiffer. Separation of betap and li in tokamaks of non-circular cross-section. *Nuclear Fusion*, 25(10):1421, 1985.

[67] J P Freidberg, M Graf, A Niemszewski, S Schultz, and A Shajii. Why beta p and l i cannot be separately measured in a near circular tokamak. *Plasma Physics and Controlled Fusion*, 35(11):1641, 1993.

[68] V.D. Pustovitov. Magnetic diagnostics: General principles and the problem of reconstruction of plasma current and pressure profiles in toroidal systems. *Nuclear Fusion*, 41(6):721, 2001.

[69] F. M. Levinton, R. J. Fonck, G. M. Gammel, R. Kaita, H. W. Kugel, E. T. Powell, and D. W. Roberts. Magnetic field pitch-angle measurments in the pbx-m tokamak using the motional stark effect. *Phys. Rev. Lett.*, 63:2060–2063, Nov 1989.

[70] F. M. Levinton. The multichannel motional stark effect diagnostic on tftr. *Review of Scientific Instruments*, 63(10):5157–5160, 1992.

[71] T Fujita, H Kuko, T Sugie, N Isei, and K Ushigusa. Current profile measurements with motional stark effect polarimeter in the jt-60u tokamak. *Fusion Engineering and Design*, 34:289 – 292, 1997.

[72] W. Kunz and Equipe TFR. First measurement of poloidal-field-induced faraday rotation in a tokamak plasma. *Nuclear Fusion*, 18(12):1729, 1978.

[73] H. Soltwisch. Current distribution measurement in a tokamak by fir polarimetry (invited). *Review of Scientific Instruments*, 57(8):1939–1944, 1986.

[74] H. Soltwisch. Measurement of current density changes during sawtooth activity in a tokamak by farinfrared polarimetry. *Review of Scientific Instruments*, 59(8):1599–1604, 1988.

[75] Nadine Aubry, Régis Guyonnet, and Ricardo Lima. Spatiotemporal analysis of complex signals: Theory and applications. *Journal of Statistical Physics*, 64(3):683–739, 1991.

[76] T. Dudok de Wit, A.L. Pecquet, J.C. Vallet, and R. Lima. The biorthogonal decomposition as a tool for investigating fluctuations in plasmas. *Physics of Plasmas*, 1(10):3288–3300, 1994.

[77] T Dudok de Witt. Enhancement of multichannel data in plasma physics by biorthogonal decomposition. *Plasma Physics and Controlled Fusion*, 37(2):117, 1995.

[78] J.P. Christiansen and J.B. Taylor. Determination of current distribution in a tokamak. *Nuclear Fusion*, 22(1):111, 1982.

[79] J.P. Christiansen, J.D. Callen, J.J. Ellis, and R.S. Granetz. Determination of current distribution in jet from soft x-ray measurements. *Nuclear Fusion*, 29(5):703, 1989.

[80] A. Holland, R. J. Fonck, E. T. Powell, and S. Sesnic. Tomographic imaging of mhd activity in tokamaks by combining diode arrays and a tangentially viewing pinhole camera. *Review of Scientific Instruments*, 59(8):1819–1821, 1988.

[81] E.T. Powell, R.J. Fonck, R. Kaita, N. Asakura, R.E. Bell, S.M. Kaye, H.W. Kugel, B. LeBlanc, F.M. Levinton, M. Okabayashi, S.F. Paul, D.W. Roberts, S. Sesnic, and H. Takahashi. Current distribution modification measurements in the pbx-m tokamak. *Nuclear Fusion*, 33(10):1493, 1993.

[82] K. Tritz, R. Fonck, and T. Thorson. Application of x-ray imaging to current profile measurements in the pegasus experiment. *Review of Scientific Instruments*, 70(1):595–598, 1999.

[83] K. Tritz, R. Fonck, M. Reinke, and G. Winz. Tangential soft x-ray imaging for shape and current profile measurements. *Review of Scientific Instruments*, 74(3):2161–2164, 2003.

[84] Abel Niels Henrik. Résolution dun probleme de mécanique. *J. Reine u. Angew. Math*, 1826.

[85] J.P. Qian, L.L. Lao, Q.L. Ren, H. Rinderknecht, F. Volpe, C. Zhang, and B.N. Wan. Equilibrium reconstruction of plasma profiles based on soft x-ray imaging in diii-d. *Nuclear Fusion*, 49(2):025003, 2009.

[86] Joshua Stillerman and Thomas W. Fredian. The mdsplus data acquisition system, current status and future directions. *Fusion Engineering and Design*, 43(3):301 – 308, 1999.

[87] P. Smeulders. Tomography of quasi-static deformations of constant-emission surfaces of high-beta plasmas in asdex. *Nuclear Fusion*, 26(3):267, 1986.

[88] M C Borras and R S Granetz. Discrepancies between soft x-ray emissivity contours and magnetic flux surfaces in alcator c-mod. *Plasma Physics and Controlled Fusion*, 38(3):289, 1996.

[89] C. Cates, M. Shilov, M. E. Mauel, G. A. Navratil, D. Maurer, S. Mukherjee, D. Nadle, J. Bialek, and A. Boozer. Suppression of resistive wall instabilities with distributed, independently controlled, active feedback coils. *Physics of Plasmas*, 7(8):3133–3136, 2000.

[90] J.T. Scoville and R.J. La Haye. Multi-mode error field correction on the diii-d tokamak. *Nuclear Fusion*, 43(4):250, 2003.

[91] L.A. Artsimovich. Tokamak devices. *Nuclear Fusion*, 12(2):215, 1972.

[92] V.A. Vershkov and S.V. Mirnov. Role of impurities in current tokamak experiments. *Nuclear Fusion*, 14(3):383, 1974.

[93] M. Murakami, J.D. Callen, and L.A. Berry. Some observations on maximum densities in tokamak experiments. *Nuclear Fusion*, 16(2):347, 1976.

[94] S.J. Fielding, J. Hugill, G.M. McCracken, J.W.M. Paul, R. Prentice, and P.E. Stott. High-density discharges with gettered torus walls in dite. *Nuclear Fusion*, 17(6):1382, 1977.

[95] S. Costa, R. De Angelis, S. Ortolani, and M.E. Puiatti. Total radiation measurements in the eta-beta ii experiment. *Nuclear Fusion*, 22(10):1301, 1982.

[96] J. Hugill and et al. High density operation in dite with neutral beam injection. Technical report, Culham Laboratory Report, 1983.

[97] S. Sudo, Y. Takeiri, H. Zushi, F. Sano, K. Itoh, K. Kondo, and A. Iiyoshi. Scalings of energy confinement and density limit in stellarator/heliotron devices. *Nuclear Fusion*, 30(1):11, 1990.

[98] ItohKimitaka and ItohSanae-Inoue. Detached and attached plasma in stellarators. *Journal of the Physical Society of Japan*, 57(4):1269–1272, 1988.

[99] L Giannone, J Baldzuhn, R Burhenn, P Grigull, U Stroth, F Wagner, R Brakel, C Fuchs, H J Hartfuss, K McCormick, A Weller, C Wendland, NBI Team, ECRH Team, W7-AS Team, K Itoh, and S-I Itoh. Physics of the density limit in the w7-as stellarator. *Plasma Physics and Controlled Fusion*, 42(6):603, 2000.

[100] B. Lipschultz, B. LaBombard, E.S. Marmar, M.M. Pickrell, J.L. Terry, R. Watterson, and S.M. Wolfe. Marfe: an edge plasma phenomenon. *Nuclear Fusion*, 24(8):977, 1984.

[101] B. Lipschultz. Review of marfe phenomena in tokamaks. *Journal of Nuclear Materials*, 145:15 – 25, 1987.

[102] G.F. Matthews. Plasma detachment from divertor targets and limiters. *Journal of Nuclear Materials*, 220:104 – 116, 1995.

[103] C S Pitcher and P C Stangeby. Experimental divertor physics. *Plasma Physics and Controlled Fusion*, 39(6):779, 1997.

[104] M. Greenwald, R.L. Boivin, F. Bombarda, P.T. Bonoli, C.L. Fiore, D. Garnier, J.A. Goetz, S.N. Golovato, M.A. Graf, R.S. Granetz, S. Horne, A. Hubbard, I.H. Hutchinson, J.H. Irby, B. LaBombard, B. Lipschultz, E.S. Marmar, M.J. May, G.M. McCracken, P. O'Shea, J.E. Rice, J. Schachter, J.A. Snipes, P.C. Stek, Y. Takase, J.L. Terry, Y. Wang, R. Watterson, B. Welch, and S.M. Wolfe. H mode confinement in alcator c-mod. *Nuclear Fusion*, 37(6):793, 1997.

[105] N Asakura, K Shimizu, H Shirai, Y Koide, and T Takizuka. Degradation of energy and particle confinement in high-density elmy h-mode plasmas on jt-60u. *Plasma Physics and Controlled Fusion*, 39(9):1295, 1997.

[106] W Suttrop, A G Peeters, F Ryter, J Stober, and the ASDEX Upgrade team. Physics and scaling of the h-mode transition in asdex upgrade. *Plasma Physics and Controlled Fusion*, 41(3A):A569, 1999.

[107] H Zohm. Edge localized modes (elms). *Plasma Physics and Controlled Fusion*, 38(2):105, 1996.

[108] V. Mertens, M. Kaufmann, J. Neuhauser, J. Schweinzer, J. Stober, K. Buchl, O. Gruber, G. Haas, A. Herrmann, A. Kallenbach, and M. Weinlich. High density operation close to greenwald limit and h mode limit in asdex upgrade. *Nuclear Fusion*, 37(11):1607, 1997.

[109] F Ryter, W Suttrop, B Brsehaber, M Kaufmann, V Mertens, H Murmann, A G Peeters, J Stober, J Schweinzer, H Zohm, and ASDEX Upgrade Team. H-mode power threshold and transition in asdex upgrade. *Plasma Physics and Controlled Fusion*, 40(5):725, 1998.

[110] G.M. McCracken, J. Allen, K. Axon, R. Barnsley, S.J. Fielding, D.H.J. Goodall, N. Hawkes, J. Hugill, P.C. Johnson, G.F. Matthews, and C.S. Pitcher. A study of detached plasmas in the dite tokamak. *Journal of Nuclear Materials*, 145:181 – 185, 1987.

[111] J.D. Strachan, F.P. Boody, C.E. Bush, S.A. Cohen, B. Grek, L. Grisham, F.C. Jobes, D.W. Johnson, D.K. Mansfield, S.S. Medley, W. Morris, H.K. Park, J.F. Schivell, G. Taylor, K.L. Wong, S. Yoshikawa, M.C. Zarnstorff, and S.J. Zweben. Experimental results from detached plasmas in tftr. *Journal of Nuclear Materials*, 145:186 – 190, 1987.

[112] Robert G. Kleva and J. F. Drake. Density limit disruptions in tokamaks. *Physics of Fluids B: Plasma Physics*, 3(2):372–383, 1991.

[113] Plasma Control ITER Physics Expert Group on Disruptions, MHD, and ITER Physics Basis Editors. Chapter3: Mhd stability operational limits and disruptions. *Nuclear Fusion*, 39(12):2251, 1999.

[114] M.G. Bell, G.L. Schmidt, P.C. Efthimion, B. Grek, R.A. Hulse, D.K. Owens, H.K. Park, A.T. Ramsey, J.F. Schivell, and G. Taylor. Attainment of high plasma densities in tftr with injection of multiple deuterium pellets. *Nuclear Fusion*, 32(9):1585, 1992.

[115] R. Maingi, M.A. Mahdavi, T.W. Petrie, L.R. Baylor, T.C. Jernigan, R.J. La Haye, A.W. Hyatt, M.R. Wade, J.G. Watkins, and D.G. Whyte. Density limit studies on diii-d. *Journal of Nuclear Materials*, 266269:598 – 603, 1999.

[116] Y. Kamada, N. Hosogane, R. Yoshino, T. Hirayama, and T. Tsunematsu. Study of the density limit with pellet fuelling in jt-60. *Nuclear Fusion*, 31(10):1827, 1991.

[117] A. Stabler, K. McCormick, V. Mertens, E.R. Muller, J. Neuhauser, H. Niedermeyer, K.-H. Steuer, H. Zohm, F. Dollinger, A. Eberhagen, G. Fussmann, O. Gehre, J. Gernhardt, T. Hartinger, J.V. Hofmann, E. Kakoulidis, M. Kaufmann, G. Kyriakakis, R.S. Lang, H.D. Murmann, W. Poschenrieder, F. Ryter, W. Sandmann, U. Schneider, G. Siller, F.X. Soldner, N. Tsois, O. Vollmer, and F. Wagner. Density limit investigations on asdex. *Nuclear Fusion*, 32(9):1557, 1992.

[118] R. Maingi, M. A. Mahdavi, T. C. Jernigan, R. J. La Haye, A. W. Hyatt, L. R. Baylor, D. G. Whyte, M. R. Wade, T. W. Petrie, J. W. Cuthbertson, A. W. Leonard, M. Murakami, R. T. Snider, R. D. Stambaugh, J. G. Watkins, W. P. West, and R. D. Wood. Investigation

of physical processes limiting plasma density in high confinement mode discharges on diii-d. *Physics of Plasmas*, 4(5):1752–1760, 1997.

[119] F. X. Söldner, E. R. Müller, F. Wagner, H. S. Bosch, A. Eberhagen, H. U. Fahrbach, G. Fussmann, O. Gehre, K. Gentle, J. Gernhardt, O. Gruber, W. Herrmann, G. Janeschitz, M. Kornherr, K. Krieger, H. M. Mayer, K. McCormick, H. D. Murmann, J. Neuhauser, R. Nolte, W. Poschenrieder, H. Röhr, K. H. Steuer, U. Stroth, N. Tsois, and H. Verbeek. Improved confinement in high-density ohmic discharges in asdex. *Phys. Rev. Lett.*, 61(0):1105–1108, Aug 1988.

[120] C. L. Fiore, J. E. Rice, P. T. Bonoli, R. L. Boivin, J. A. Goetz, A. E. Hubbard, I. H. Hutchinson, R. S. Granetz, M. J. Greenwald, E. S. Marmar, D. Mossessian, M. Porkolab, G. Taylor, J. Snipes, S. M. Wolfe, and S. J. Wukitch. Internal transport barriers on alcator c-mod. *Physics of Plasmas*, 8(5):2023–2028, 2001.

[121] A. Gibson. Radiation limits to tokamak operation. *Nuclear Fusion*, 16(3):546, 1976.

[122] J. F. Drake. Marfes: Radiative condensation in tokamak edge plasma. *The Physics of Fluids*, 30(8):2429–2433, 1987.

[123] P.N. Guzdar, C.S. Liu, and J.Q. Dong. Thermal equilibria of detached plasmas and density limits. *Nuclear Fusion*, 28(10):1791, 1988.

[124] M. Z. Tokar. On threshold of radial detachment in tokamaks. *Physics of Plasmas*, 7(6):2432–2438, 2000.

[125] J. Neuhauser and R. Wunderlich. A radially continuous two-chamber model for the high-recycling divertor edge layer. *Journal of Nuclear Materials*, 145:877 – 880, 1987.

[126] H Capes, P Ghendrih, A Samain, A Grosman, and J P Morera. Thermal equilibrium in a diverted plasma. *Plasma Physics and Controlled Fusion*, 32(2):103, 1990.

[127] D. L. Brower, C. X. Yu, R. V. Bravenec, H. Lin, N. C. Luhmann, W. A. Peebles, Ch. P. Ritz, B. A. Smith, A. J. Wootton, Z. M. Zhang, and S. J. Zhao. Confinement degradation

and enhanced microturbulence as long-time precursors to high-density-limit tokamak disruptions. *Phys. Rev. Lett.*, 67(2):200–203, Jul 1991.

[128] M.M. Marinak. Behaviour of the particle transport coefficients near the density limit in the microwave tokamak experiment. *Nuclear Fusion*, 35(4):399, 1995.

[129] F. Sardei, P. Grigull, Y. Feng, G. Herre, D. Hildebrandt, J. Kilinger, F. Wagner, and H. Wolff. Boundary layer study on the wendelstein 7-as stellarator. *Journal of Nuclear Materials*, 220:736 – 740, 1995.

[130] R.A. Moyer, J.W. Cuthbertson, T.E. Evans, G.D. Porter, and J.G. Watkins. The role of turbulent transport in diii-d edge and divertor plasmas. *Journal of Nuclear Materials*, 241:633 – 638, 1997.

[131] B. LaBombard, R. L. Boivin, M. Greenwald, J. Hughes, B. Lipschultz, D. Mossessian, C. S. Pitcher, J. L. Terry, S. J. Zweben, and Alcator Group. Particle transport in the scrape-off layer and its relationship to discharge density limit in alcator c-mod. *Physics of Plasmas*, 8(5):2107–2117, 2001.

[132] F A Haas and A Thyagaraja. A phenomenological interpretation of transport limits and slow-time evolution in tokamaks. *Plasma Physics and Controlled Fusion*, 28(8):1093, 1986.

[133] D. R. Thayer and P. H. Diamond. Thermally driven convective cells and tokamak edge turbulence. *The Physics of Fluids*, 30(12):3724–3734, 1987.

[134] R. W. Harvey and R. O. Dendy. A trapped passing fluid model for tokamak neoclassical transport. *Physics of Fluids B: Plasma Physics*, 4(4):902–910, 1992.

[135] B. N. Rogers, J. F. Drake, and A. Zeiler. Phase space of tokamak edge turbulence, the $L-H$ transition, and the formation of the edge pedestal. *Phys. Rev. Lett.*, 81(20), 1998.

[136] D. A. Gates and L. Delgado-Aparicio. Origin of tokamak density limit scalings. *Phys. Rev. Lett.*, 108(16):165004, 2012.

[137] D.A. Gates, L. Delgado-Aparicio, and R.B. White. Physics of radiation-driven islands near the tokamak density limit. *Nuclear Fusion*, 53(6):063008, 2013.

[138] R. B. White, D. A. Gates, and D. P. Brennan. Thermal island destabilization and the greenwald limit. *Physics of Plasmas*, 22(2):022514, 2015.

[139] D. A. Gates, D. P. Brennan, L. Delgado-Aparicio, Q. Teng, and R. B. White. Thermo-resistive disruptions and the tokamak density limit. *Physics of Plasmas*, 23(5):056113, 2016.

[140] Q. Teng, D.P. Brennan, L. Delgado-Aparicio, D.A. Gates, J. Swerdlow, and R.B. White. A predictive model for the tokamak density limit. *Nuclear Fusion*, 56(10):106001, 2016.

[141] F. Salzedas, F. C. Schüller, A. A. M. Oomens, and the RTP Team. Exponentially growing tearing modes in rijnhuizen tokamak project plasmas. *Phys. Rev. Lett.*, 88(7):075002, 2002.

[142] Harold P. Furth, John Killeen, and Marshall N. Rosenbluth. Finite resistivity instabilities of a sheet pinch. *The Physics of Fluids*, 6(4):459–484, 1963.

[143] H. P. Furth, P. H. Rutherford, and H. Selberg. Tearing mode in the cylindrical tokamak. *The Physics of Fluids*, 16(7):1054–1063, 1973.

[144] J.A. Wesson, R.D. Gill, M. Hugon, F.C. Schller, J.A. Snipes, D.J. Ward, D.V. Bartlett, D.J. Campbell, P.A. Duperrex, A.W. Edwards, R.S. Granetz, N.A.O. Gottardi, T.C. Hender, E. Lazzaro, P.J. Lomas, N. Lopes Cardozo, K.F. Mast, M.F.F. Nave, N.A. Salmon, P. Smeulders, P.R. Thomas, B.J.D. Tubbing, M.F. Turner, and A. Weller. Disruptions in jet. *Nuclear Fusion*, 29(4):641, 1989.

[145] A. H. Glasser, H. P. Furth, and P. H. Rutherford. Stabilization of resistive kink modes in the tokamak. *Phys. Rev. Lett.*, 38(5):234–237, 1977.

[146] K. Matsuoka, K. Miyamoto, K. Ohasa, and M. Wakatani. Magnetohydrodynamic instabilities in a current-carrying stellarator. *Nuclear Fusion*, 17(6):1123, 1977.

[147] K. Matsuoka and K. Miyamoto. Stabilization of mhd-instabilities in a current-carrying stellarator. *Nuclear Fusion*, 19(6):837, 1979.

[148] E. Sallander, A. Weller, and W7-AS Team. Effects of non-vanishing toroidal current densities on stability in the wendelstein7-as stellarator. *Nuclear Fusion*, 40(8):1499, 2000.

[149] J. L. Johnson, C. R. Oberman, R. M. Kulsrud, and E. A. Frieman. Some stable hydromagnetic equilibria. *The Physics of Fluids*, 1(4):281–296, 1958.